

Stochastic geometry models for interacting fibers

Prakash EASWARAN

1. Gutachter: Prof. Dr. Claudia REDENBACH
Technische Universität Kaiserslautern
2. Gutachter: Prof. Dr. Dominique JEULIN
MINES ParisTech

Datum der Disputation: 23.10.2017

Vom Fachbereich Mathematik der Technischen Universität Kaiserslautern
zur Verleihung des akademischen Grades Doktor der Naturwissenschaften
(Doctor rerum naturalium) genehmigte Dissertation

D386

Acknowledgements

I am grateful for funding by the German Federal Ministry of Education and Research through project 05M13 (AniS), Center for Mathematical and Computational Modelling(CM)² and the Deutsche Forschungsgemeinschaft (DFG) through the GrK 1932 “Stochastic Models for Innovations in the Engineering Sciences”, project area P3. I thank Fraunhofer ITWM for providing me a working place and giving me access to all facilities at the institute.

I would like to acknowledge Dr Stefan Rief, Flow and Material Simulation, Fraunhofer ITWM for providing data which is considered in Chapter 4.

I am thankful to Dr. Martin J. Lehmann and Friedemann Hahn, MANN+HUMMEL GMBH, Ludwigsburg, Germany for computing numerical simulation results for the domain size study.

For the sample considered in Chapter 6, Section 6.3., I acknowledge Frank Schuler, Department of civil engineering, University of Kaiserslautern. I acknowledge Markus Kroneberger for detecting fiber clusters from the real data which is considered in Chapter 6, Section 6.3.

Software packages such as MAVI, MAVIlib and Toolip developed at Fraunhofer ITWM, Department of image processing have been used as toolbox for algorithms considered in this thesis and for 3D image visualization.

Preface

First of all, I would like to express my sincere gratitude to Claudia Redenbach and Katja Schladitz for their systematic guidance and fruitful discussions throughout the course of this thesis. Their guidance helped me in all the time of research and writing of this thesis. The door to their office was always open whenever I ran into a trouble spot or had a question about my research or writing. This work would not have been possible without their support and encouragement.

I am deeply grateful to Oliver Wirjadi and Michael Godehardt for their suggestions and technical assistance during my thesis. They were always willing to help and give their best suggestions.

I would also like to thank Sonja Föhst, Martina Sormani, Markus Kronenberger and all other members of Fraunhofer ITWM, department of image processing for their support throughout my studies. Also I thank all of my friends especially Karthick for their help.

Finally, I would like to thank Radha and all other family members for their love, sacrifice and encouragement.

Abstract

Nonwoven materials are used as filter media which are the key component of automotive filters such as air filters, oil filters, and fuel filters. Today, the advanced engine technologies require innovative filter media with higher performances. A virtual microstructure of the nonwoven filter medium, which has similar filter properties as the existing material, can be used to design new filter media from existing media. Nonwoven materials considered in this thesis prominently feature non-overlapping fibers, curved fibers, fibers with circular cross section, fibers of apparently infinite length, and fiber bundles. To this end, as part of this thesis, we extend the Altendorf-Jeulin individual fiber model to incorporate all the above mentioned features. The resulting novel stochastic 3D fiber model can generate geometries with good visual resemblance of real filter media. Furthermore, pressure drop, which is one of the important physical properties of the filter, simulated numerically on the computed tomography (CT) data of the real nonwoven material agrees well (with a relative error of 8%) with the pressure drop simulated in the generated microstructure realizations from our model.

Generally, filter properties for the CT data and generated microstructure realizations are computed using numerical simulations. Since numerical simulations require extensive system memory and computation time, it is important to find the representative domain size of the generated microstructure for a required filter property. As part of this thesis, simulation and a statistical approach are used to estimate the representative domain size of our microstructure model. Precisely, the representative domain size with respect to the packing density, the pore size distribution, and the pressure drop are considered. It turns out that the statistical approach can be used to estimate the representative domain size for the given property more precisely and using less generated microstructures than the purely simulation based approach.

Among the various properties of fibrous filter media, fiber thickness and orientation are important characteristics which should be considered in design and quality assurance of filter media. Automatic analysis of images from scanning electron microscopy (SEM) is a suitable tool in that context. Yet, the accuracy of such image analysis tools cannot be judged based on images of real filter media since their true fiber thickness and orientation can never be known accurately. A solution is to employ synthetically generated models for evaluation. By combining our 3D fiber system model with simulation of the SEM imaging process, quantitative evaluation of the fiber thickness and orientation measurements becomes feasible. We evaluate the state-of-the-art automatic thickness and orientation estimation method that way.

Contents

1	Introduction	1
2	Preliminaries	7
2.1	Stochastic geometry	7
2.2	Orientation distributions	8
2.2.1	The Schladitz distribution	8
2.2.2	The von Mises-Fisher distribution	9
2.2.3	The multivariate von Mises-Fisher distribution	9
2.3	Morphological operations	10
2.4	Random sequential adsorption model	11
2.5	Edge effects	11
2.6	Image data	12
2.6.1	Median filter	13
3	Stochastic modeling of three-dimensional fiber systems incorporating interaction	15
3.1	The Altendorf-Jeulin model for dense fiber systems	18
3.2	Modeling of fiber systems with endless fibers	26
3.3	Modeling of fiber systems incorporating interaction	33
4	Parameter estimation and Model fitting	39
4.1	Parameter estimation	39
4.1.1	Volume fraction	39
4.1.2	Radius estimation	40
4.1.3	Orientation estimation	40
4.2	Model fitting	50
5	Representative domain size for simulated three-dimensional fiber systems	55
5.1	Microstructure generation for domain size study	55
5.2	Simulation study regarding domain size	57

5.3	Statistical study regarding domain size	58
5.4	Results	60
6	Applications	63
6.1	Validation of an automatic fiber analysis tool	63
6.1.1	Validation of fiber thickness estimation	63
6.1.2	Validation of fiber orientation estimation	67
6.2	Modeling of bio-pore structures	71
6.3	Separation and labeling of fibers in steel fiber reinforced concrete	73
6.3.1	Pre-processing	74
6.3.2	Fiber separation	75
6.3.3	Post-processing	76
7	Conclusions and future work	81
7.1	Conclusions	81
7.2	Future work	82
1	Appendix	83
A.1	The method for fiber orientation and radius estimation	83
	Academic curriculum vitae	87
	Bibliography	91
	List of Figures	97
	List of Tables	103

Notations

Φ	Poisson point process
Λ	intensity measure
ν_d	d - dimensional Lebesgue measure
S^2	unit sphere in \mathbb{R}^3
θ	polar angle
ϕ	azimuthal angle
β	anisotropy parameter
f	probability density function of the Schladitz distribution
f_{vMF}	probability density function of the von Mises-Fisher distribution
f_{mvMF}	probability density function of the multivariate von Mises-Fisher distribution
κ_1 and κ_2	concentration parameters for the multivariate von Mises-Fisher distribution
\mathbb{F}_{loc}	local adjacency system
\mathbb{F}	adjacency system
P	fiber system
P_j	j -th fiber of the system
FS	fiber system with fiber bundles
P_{kj}	j -th fiber of the k -th bundle
p_{kji}	i -th sphere in the j -th fiber of the k -th bundle
F_{RP}	repulsion force
f_{δ_s, δ_e}	friction factor
F_{RS}	recover spring force
F_{RA}	recover angle force
I_A	characteristic function of a set A
W	sampling window
W'	extended window
V_F	volume fraction
i.i.d.	independent, identically distributed
Pa	Pascal
ϵ_{abs}	absolute error
ϵ_{rel}	relative error

1

Introduction

Nonwoven fabric is a fibrous material produced using staple fibers (fibers of finite length) or continuous filaments (fibers of apparently infinite length) bonded together by chemical, mechanical or thermal processes. It is a flexible, flat shaped and porous material. It can be disposable (single use) or durable (long-lasting) based on the production process and bonding techniques used. In addition to that, several salient features can be achieved from nonwoven fabrics such as absorbency, sterility, softness, flame retardancy, strength, stretch, washability, or liquid repellency. These properties render non-woven fabrics popular in various applications such as:

- **Hygiene:** Baby diapers, feminine hygiene products, incontinence products, wipes, etc.
- **Medical:** Bandages, masks, surgical gowns, isolation gowns, gloves, etc.
- **Filtration:** Room air cleaners, vacuum bags, automotive filters, water filters, odor filters, tea bags, etc.
- **Agriculture:** Crop covers, root control bags, biodegradable plant pots, etc.

The three main methods used for the production of nonwoven fabrics are drylaid, wetlaid and spunmelt [Hutten 2007]. The spunmelt approach is further classified into spunbond and meltblown. The spunbond and meltblown techniques convert the molten polymers into continuous filament nonwoven fabrics. The production process of these two techniques is described in the following.

- **Spunbond or Spunlaid:** In the first step, polymer chips or flakes are melted and the molten polymer is forced through a small metal plate consisting of several drilled holes which is called spinnerette. When molten polymer exits the spinnerette, it will form fine filament fibers. These filaments are cooled and stretched by air, and deposited on a moving conveyor belt. Finally, thermal, chemical or mechanical bonding is used to bond the fibers. An illustration of this process is given in Figure 1.1.
- **Meltblown:** It is similar to the spunbond approach. The only difference is that high velocity hot air is injected near the spinnerette tips.

In this thesis, we consider nonwoven fabrics produced using the spunmelt approach which are used as filter medium in automotive filters such as fuel filters, oil filters, engine air filters, and cabin air filters. A filter medium is a porous material used in filters to block out the solid particles. In general, filtration is the process of passing liquid or gas through material to filter contaminants from the liquid or gas being treated [Bourke et al. 1995]. The following types of filters are used in automobiles.

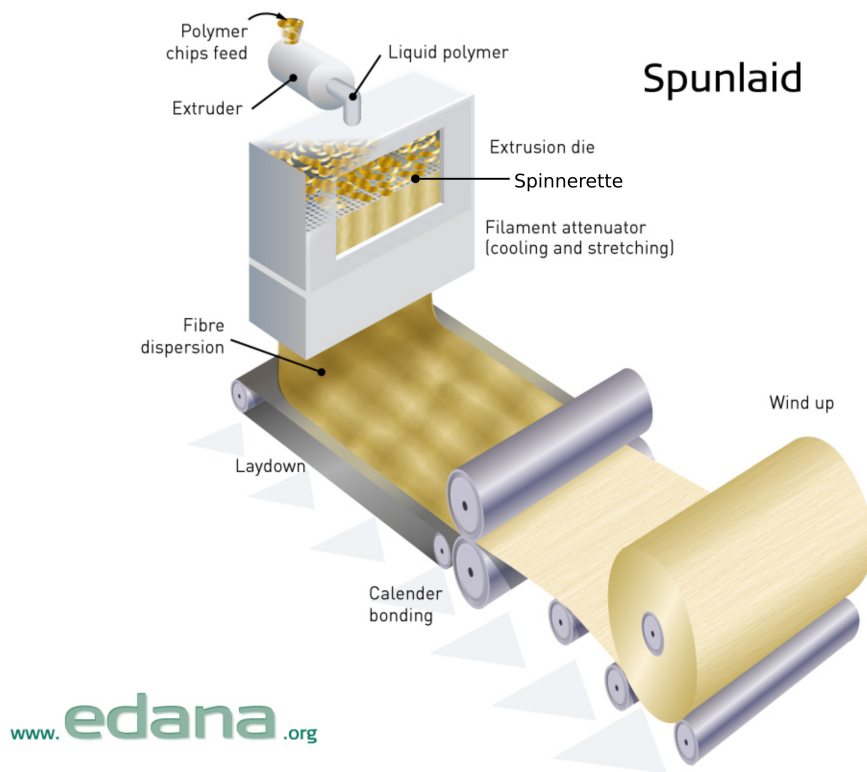


Figure 1.1 – Spunbond process. Image source: <http://www.edana.org>

- **Fuel filter:** Dust, dirt particles, and water may enter into the fuel during its production, storage, or transportation process. These contaminants can damage the fuel injection systems and all parts of the engine that transport fuel. Therefore, fuel filters are used to filter these impurities and any water contained in the fuel before it reaches the engine.
- **Oil filter:** It filters dust, metal particles, and other contaminants from the engine lubricating oil to protect the engine from wear and damage.
- **Engine air filter:** Intake air contains impurities such as dust, sand, moisture, pollen, soot, fine tire particles, etc. Clean air is important for optimal engine performance. The air filter stops the contaminants before they reach the engine.
- **Cabin air filter:** Air entering the vehicle through the air conditioning or ventilation system contains pollen and other impurities. The air filters are used to block these particles to provide clean air to the vehicle interior.

Today, the customer needs and advanced engine technologies require innovative filter media with higher performances. For instance, an efficient air filter could maximize the engine performances with minimum fuel consumption and hence reduce air pollution [Abdullah et al. 2013]. On the contrary, a poor air filter reduces engine performance and raises fuel consumption. This leads to an increased concentration of toxic substances in the exhaust gases. Moreover, filter properties such as

flow rate, pressure drop, dust holding capacity, permeability (capacity to transmit fluids through a porous medium), etc. are highly influenced by the microstructure of the filter media used [Matteson and Orr 1987]. If the pore size is larger than the size of contaminants, particles which are smaller than the pores will enter into the engine. These unblocked impurities cause severe damage to the engine and the engine creates more air pollution. On the other hand, if the size of the pore is too small, there is not enough fuel flow to the engine (high pressure drop). Therefore, the production of filter media with a suitable microstructure is the first step to enhance the performance of a filter.

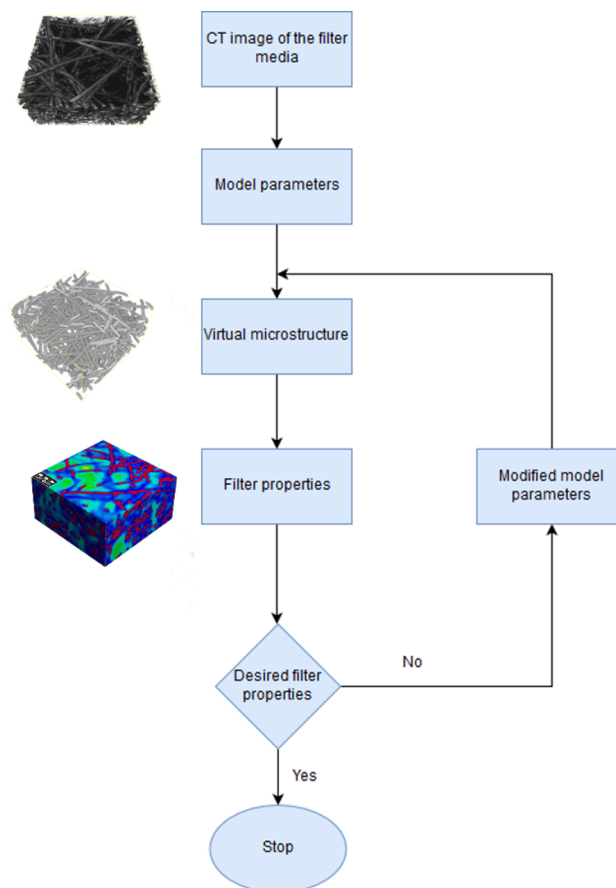


Figure 1.2 – Flow chart for virtual microstructure design. 3D rendering of the first two images are obtained using MAVI (Fraunhofer ITWM, Department of Image processing 2016) and third image using the GeoDict2017 software (Math2Market, Kaiserslautern, Germany).

Numerical filter simulations can be used to investigate the relationships between geometric and filtration properties of existing filter media from three-dimensional (3D) computed tomography (CT) images. In order to design new filter media from existing media, the microstructure of the existing media should be altered and tested numerically. However, it is unrealistic to adjust the microstructure directly in the CT image. Therefore, there is need for a virtual microstructure of the nonwoven filter medium which has similar filter properties as the existing material. The virtual geometry can be evaluated by comparing its macroscopic properties with the real material characteristics based on image data. The virtual microstructure can be changed by modifying its

model parameters. This modification is repeated until the desired filter properties are obtained. The resulting microstructures are treated as the virtual prototypes for new filter media. A flow chart of this procedure is shown in Figure 1.2. Then, these prototypes can be utilized to produce new filter media through an industrial production process. Hence, as part of this thesis, a realistic microstructure model for nonwoven filter media is developed by extending the 3D stochastic model proposed by Altendorf and Jeulin 2011a.

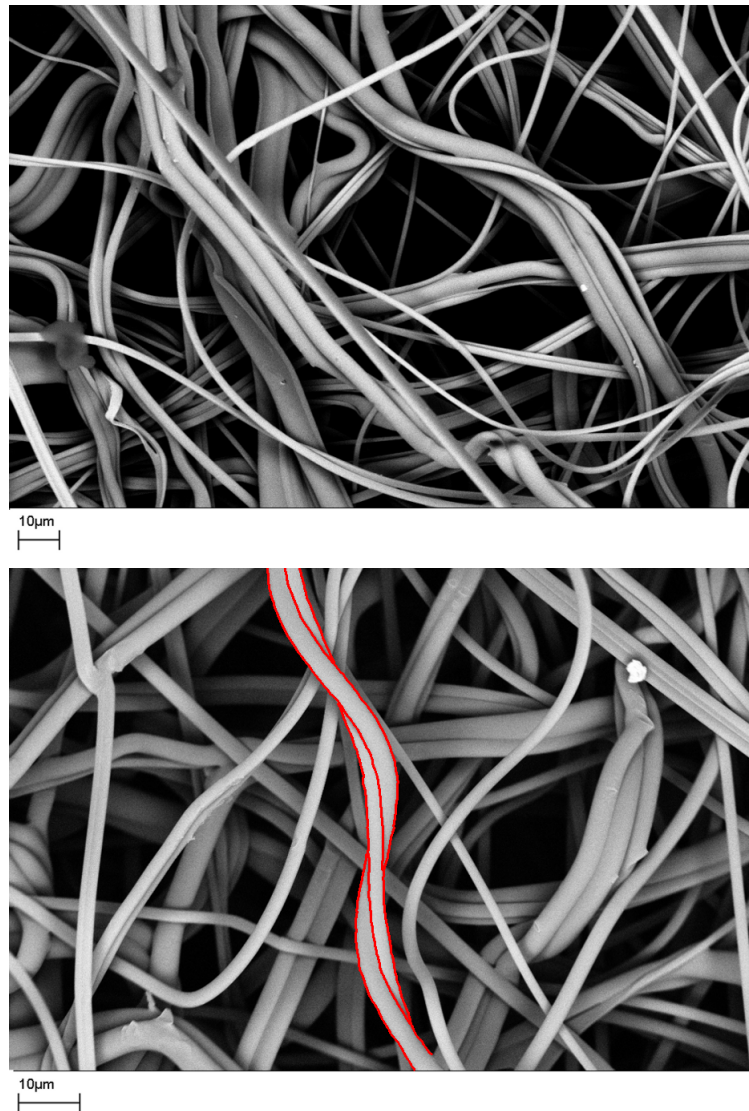


Figure 1.3 – Scanning electron microscopy (SEM) images of nonwoven polymer filter media from MANN+HUMMEL GmbH, Ludwigsburg.

Altendorf and Jeulin developed a stochastic model for the microstructure of glass fiber reinforced polymers. Realizations with high volume density of non-overlapping fibers can be achieved. It generates curved fibers of finite length. Since nonwoven material produced from the spunmelt approach is a continuous filament, its microstructure does not contain any fiber ends. For instance,

we can observe this in two-dimensional (2D) scanning electron microscopy (SEM) images of real nonwoven materials as shown in Figure 1.3. Therefore, as the first modification, we replace fibers of finite length by fibers of seemingly infinite length. Furthermore, nonwoven fabrics include fiber bundles in their geometry. A fiber bundle is a group of touching fibers which are oriented in the same direction. One of the fiber bundles is highlighted in Figure 1.3. Hence, further, we extend this model to incorporate fiber bundles. These extensions are given in Chapter 3. In Chapter 4, the proposed stochastic model is fitted to the CT data of a real non-woven material.

Both the microstructure generation and numerical simulation for domain sizes larger than 2000^3 voxels with 2000 fibers, require extensive system memory and computation time. Instead of doing simulations in the larger domains, we can do it on smaller domains, and finally, the results can be scaled up to the larger domains (homogenization). The smallest domain which represents physical properties of the larger domains is called representative domain size. The representative domain size with respect to packing density, pore size distribution, and pressure drop for our simulated microstructures is studied in Chapter 5. The homogenization step is not considered in this thesis.

Two widely used imaging techniques to capture the microstructure of materials are computed tomography (CT) and scanning electron microscopy (SEM). CT produces 3D images, whereas SEM produces 2D images. Geometric characteristics of the filter medium such as fiber thickness, fiber orientation, pore size distribution, etc. can be estimated from both CT and SEM images. Since SEM images are less expensive than CT, industries prefer SEM over CT images to analyze the fiber thickness and the fiber orientation distribution. These two properties are important characteristics which should be considered in the design and quality assurance of filter media. In particular, the fiber thickness distribution influences the filter efficiency [Payen et al. 2012]. Furthermore, the collection efficiency of filter media is influenced by the fiber orientation distribution [Bharadwaj et al. 2008]. Therefore, design and quality assurance during the production of filter media require means to quantify the fiber thickness, fiber orientation, and pore diameter, among other relevant parameters.

Various measuring techniques for the fiber thickness and orientation distribution from 2D SEM images with minimal or without human intervention have been developed in the last few years [Ziabari et al. 2007, Shin et al. 2008, Altendorf et al. 2010, Lehmann et al. 2013, Öznergiz et al. 2014 and Wirjadi et al. 2016]. Yet, the accuracy of existing analysis tools cannot be judged based on images of real filter media, since their true fiber thickness and fiber orientation distribution can never be known exactly. Previously, manual measurement techniques were used to test the reliability of the aforementioned approaches. However, the quality of the manual measurement process depends on the operator and the accuracy in the fibers' edge detection. Geometric material models allow for a simulation of synthetic fiber systems with known thickness and orientation distributions. In realizations of such models, fiber thicknesses and fiber orientations are known precisely, and when combined with SEM simulation (Prill and Schladitz 2013), the results can be used for systematic evaluations. In the first section of Chapter 6, a 3D stochastic model of a

fiber system introduced in Chapter 3 is used to validate the automatic thickness and orientation measurement technique proposed by Altendorf and Jeulin 2009.

Section 6.2 of Chapter 6, we consider modeling of a bio-pore structure. Bio-pores in the soil are formed by soil fauna and by roots of plants (Stirzaker et al. 1996). In general, bio-pore features can be analyzed from CT images of the soil sample. To this end, bio-pores in CT images have to be segmented in order to analyze their size, shape, orientation and so forth. There are various methods available in the literature to segment bio-pores. Since the ground truth is not known for the real data, the existing techniques cannot be validated quantitatively. However, synthetic data can be used to evaluate the existing methods. Therefore, the basic extension of the Altendorf-Jeulin approach to model bio-pores is considered in Section 6.2.

In order to analyze post-cracking behavior of a steel fiber reinforced concrete sample from its CT image, each fiber in the CT image has to be separated and labeled. We apply the fiber separation algorithm proposed by Altendorf 2011c to separate fibers in a specimen of steel fiber reinforced concrete in Section 6.3 of Chapter 6.

Chapter 7 gives a summary of this thesis.

2

Preliminaries

In this chapter, we provide basic definitions and concepts which are considered in this thesis. Section 2.1 is cited from Stoyan et al. 1995 and Beneš and Rataj 2004. Sections 2.3, 2.4, and 2.6 are cited from Ohser and Schladitz 2009 and Ohser and Mücklich 2000.

2.1 Stochastic geometry

Let \mathbb{S} be a separable metric space. Let $\mathcal{B} = \mathcal{B}(\mathbb{S})$ be the Borel σ -algebra on \mathbb{S} . A measure μ on $(\mathbb{S}, \mathcal{B})$ is called locally finite if it is finite on bounded Borel sets. We denote the set of all locally finite measures on $(\mathbb{S}, \mathcal{B})$ as $\mathcal{M} = \mathcal{M}(\mathbb{S})$. Furthermore, we denote \mathcal{N} as the set of all locally finite integer-valued measures, i.e., $\mathcal{N} = \mathcal{N}(\mathbb{S}) = \{\mu \in \mathcal{M} : \mu(B) \in \mathbb{N} \cup \{0, \infty\} \text{ for all } B \in \mathcal{B}\}$.

The σ -algebra \mathfrak{M} is defined as the smallest σ -algebra on \mathcal{M} with respect to which the function $\mu \rightarrow \mu(B)$ is measurable for all $B \in \mathcal{B}$. The trace of \mathfrak{M} on \mathcal{N} is denoted as \mathfrak{N} , i.e., $\mathfrak{N} = \{M \cap \mathcal{N} : M \in \mathfrak{M}\}$.

Definition 2.1 — Random measure. Let (Ω, \mathcal{A}, P) be a probability space. A random measure ψ on \mathbb{S} is a measurable mapping $\psi : (\Omega, \mathcal{A}, P) \rightarrow (\mathcal{M}, \mathfrak{M})$.

Definition 2.2 — Point process. A point process Φ on \mathbb{S} is a measurable mapping $\Phi : (\Omega, \mathcal{A}, P) \rightarrow (\mathcal{N}, \mathfrak{N})$.

Definition 2.3 — Poisson point process. Let Λ be a locally finite measure on \mathbb{S} and \mathcal{B}_0 be the system of bounded Borel subsets of \mathbb{S} . A point process Φ on \mathbb{S} with intensity measure Λ is called the Poisson point process if

- $\Phi(B)$ has the Poisson distribution with parameter $\Lambda(B)$ for each $B \in \mathcal{B}_0$. $\Lambda(B)$ denotes the expected number of points of Φ in B .
- for each $n \in \mathbb{N}$ and $B_1, B_2, \dots, B_n \in \mathcal{B}_0$ disjoint, $\Phi(B_1), \Phi(B_2), \dots, \Phi(B_n)$ are independent random variables.

Definition 2.4 — Line process. A line process is defined as a random subset of the representation space $C = \{(\cos \alpha, \sin \alpha, p) \in \mathbb{R}^3 : p \in \mathbb{R}, \alpha \in (0, \pi]\}$ where p is the perpendicular distance of a line from the origin and α is the angle between line and the x -axis.

Definition 2.5 — Poisson line process. A Poisson line process Γ is the line process produced by a Poisson process with intensity measure Λ on the representation space C . The intensity measure $\Lambda(A)$ for each Borel subset A of C is the expected number of lines of Γ in A .

Definition 2.6 — Boolean model. Let $\Phi = \{x_1, x_2, \dots\}$ be a Poisson point process in \mathbb{S} with intensity Λ . Let the X_1, X_2, \dots be a sequence of independent identically distributed random compact sets in \mathbb{S} , independent of Φ , and satisfying the condition (refer Stoyan et al. 1995 Equation (3.1.1.))

$$\mathbf{E}(v_d(X_0 \oplus K)) < \infty \quad \text{for all compact } K \quad (2.1)$$

where X_0 denotes the random compact set of the same distribution as X_n and independent of Φ . Then the Boolean model Ξ with germs x_n and the primary grains X_n is defined as

$$\Xi = \bigcup_{n=1}^{\infty} (X_n + x_n) \quad (2.2)$$

2.2 Orientation distributions

In this section, we present the three-dimensional (3D) orientation distributions, which are used in this thesis. The spherical coordinates of a point on the unit sphere S^2 in \mathbb{R}^3 are denoted as $(\theta, \phi) \in [0, \pi) \times [0, 2\pi)$. These spherical coordinates can be converted into the Cartesian coordinates $(x, y, z) \in S^2 \subset \mathbb{R}^3$ as in the following:

$$\begin{aligned} x &= \sin \theta \cos \phi \\ y &= \sin \theta \sin \phi \\ z &= \cos \theta \end{aligned}$$

where θ is the polar angle (similar to co-latitude on the earth) and ϕ is the azimuthal angle (like longitude on the earth). In other words, θ is the angle measured from the positive z -axis and ϕ is the angle measured counterclockwise from the positive x -axis in the xy -plane projection.

2.2.1 The Schladitz distribution

The Schladitz distribution is an orientation distribution introduced by Schladitz et al. 2006, which is a special case of the angular central Gaussian distribution. The probability density function of this distribution w.r.t. spherical coordinates is

$$f(\theta, \phi | \beta) = \frac{\beta \sin \theta}{4\pi(1 + (\beta^2 - 1) \cos^2 \theta)^{\frac{3}{2}}} \quad (2.3)$$

where $\beta > 0$. The parameter β is called the anisotropy parameter. For $\beta \rightarrow 0$ the orientations concentrate on the z -axis, for $\beta = 1$ the orientations are uniformly distributed on the sphere, and for $\beta \rightarrow \infty$ orientations are isotropically distributed in the xy -plane. For later reference, we denote the

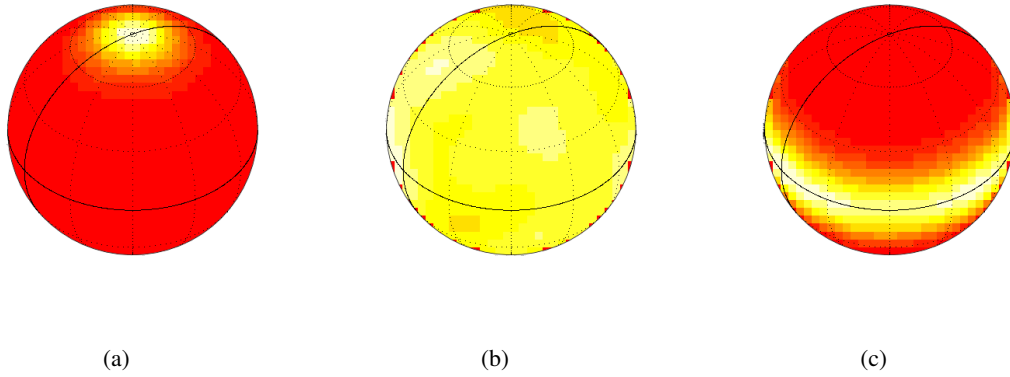


Figure 2.1 – Density plot for the Schladitz distribution. 1000 points are sampled from the Schladitz distribution on the sphere for various parameters β . (a) $\beta = 0.1$ (orientations concentrate on the z -axis) (b) $\beta = 1$ (orientations are uniformly distributed) (c) $\beta = 10$ (orientations are isotropically distributed in the xy -plane). White color represents high values and red color represents low values. Red color on sphere boundaries in (b) is due to discretization effect.

distribution for $\beta < 1$, $\beta = 1$, and $\beta > 1$ as bipolar, isotropic, and girdle, respectively. Examples of realizations for these three different cases are given in Figure 2.1.

2.2.2 The von Mises-Fisher distribution

The probability density function of the von Mises-Fisher distribution [Fisher et al. 1987] with the preferred direction $\mu \in S^2$ and the concentration parameter $\kappa > 0$ is defined as

$$f_{vMF}(v|\mu, \kappa) = \frac{\kappa}{2\pi(e^\kappa - e^{-\kappa})} e^{\kappa \mu^T v} \quad (2.4)$$

where $v \in S^2$. For larger values of κ , the distribution is more strongly concentrated around the preferred direction μ .

2.2.3 The multivariate von Mises-Fisher distribution

Kärkkäinen et al. 2009 introduced the multivariate von Mises-Fisher distribution for the 2D case. The generalization of this distribution for the 3D case is given by Altendorf and Jeulin 2011a. The probability density function of the multivariate von Mises-Fisher distribution for 3D is given as:

$$f_{mvMF}(v|\mu_1, \kappa_1, \mu_2, \kappa_2) = \frac{|\kappa_1 \mu_1 + \kappa_2 \mu_2|}{2\pi(e^{|\kappa_1 \mu_1 + \kappa_2 \mu_2|} - e^{-|\kappa_1 \mu_1 + \kappa_2 \mu_2|})} e^{\kappa_1 \mu_1^T v + \kappa_2 \mu_2^T v} \quad (2.5)$$

where $\mu_1 \in S^2$ and $\mu_2 \in S^2$ are the preferred directions, $\kappa_1 > 0$ is the concentration parameter w.r.t. μ_1 , $\kappa_2 > 0$ is the concentration parameter w.r.t. μ_2 , and $v \in S^2$.

Note that, the multivariate von Mises-Fisher distribution can be represented as the von Mises Fisher

distribution with the parameters

$$\begin{aligned}\kappa &= |\kappa_1\mu_1 + \kappa_2\mu_2| \\ \mu &= \frac{\kappa_1\mu_1 + \kappa_2\mu_2}{\kappa}.\end{aligned}$$

2.3 Morphological operations

The reflection of a set A is defined as

$$\check{A} = \{-x : x \in A\}$$

The Minkowski sum of $A \subset \mathbb{R}^n$ and $B \subset \mathbb{R}^n$ is defined as

$$\begin{aligned}A \oplus B &= \{x + y : x \in A, y \in B\} \\ &= \bigcup_{y \in B} (A + y)\end{aligned}$$

The Minkowski difference of $A \subset \mathbb{R}^n$ and $B \subset \mathbb{R}^n$ is given as

$$\begin{aligned}A \ominus B &= (A^c \oplus B)^c \\ &= \bigcap_{y \in B} (A + y)\end{aligned}$$

Definition 2.7 — Morphological dilation. The morphological dilation of a set A with the structuring element B is defined as

$$A \oplus \check{B} = \{x - y : x \in A, y \in B\}$$

Definition 2.8 — Morphological erosion. The morphological erosion of a set A with the structuring element B is defined as

$$A \ominus \check{B} = \{x \in \mathbb{R}^n : (B + x) \subset A\}$$

Definition 2.9 — Morphological opening. The morphological opening $A \circ B$ of a set A with the structuring element B is an morphological erosion followed by a Minkowski sum,

$$A \circ B = (A \ominus \check{B}) \oplus B$$

Definition 2.10 — Morphological closing. The morphological closing $A \bullet B$ of a set A with the structuring element B is an morphological dilation followed by a Minkowski difference,

$$A \bullet B = (A \oplus \check{B}) \ominus B$$

2.4 Random sequential adsorption model

The random sequential adsorption model (RSA) to generate non-overlapping cylinders in a window W is described in the following:

Step 1: Generate length and radius using any distribution in $\mathbb{R}_{>0}$ and orientation from some orientation distributions in S^2 .

Step 2: Choose a cylinder center from the uniform distribution in a given window W .

Step 3: Insert the new cylinder in the window if it does not overlap with any of the already inserted cylinders. Otherwise, return to Step 2.

Step 4: Repeat Step 1 to 3 until the desired volume fraction is reached or the desired number of cylinders is placed or it is impossible to place any more cylinders into W .

Some realizations simulated using the RSA cylinder model are given in Figure 2.2.

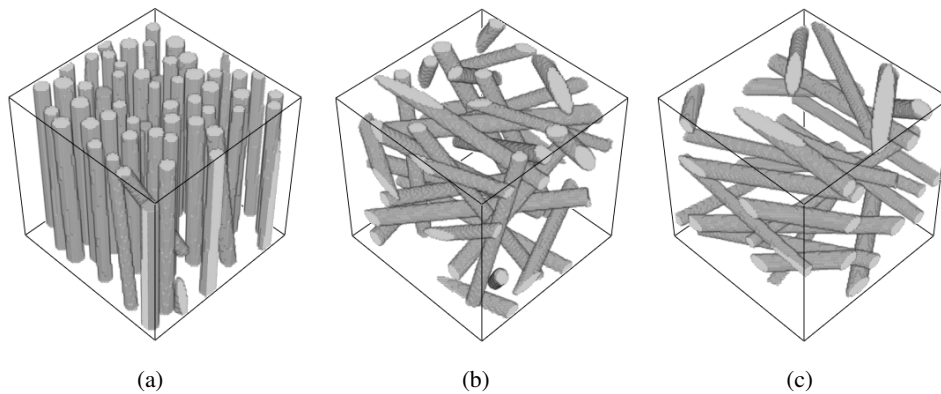


Figure 2.2 – Realizations of systems of cylinders generated using the RSA cylinder model. Common input model parameters: window size = 100^3 voxels, radius and length are uniformly distributed in the intervals $[3, 5]$ and $[150, 200]$, respectively. Orientation follows the Schladitz distribution with $\beta = 0.01$ (a), $\beta = 1$ (b), and $\beta = 5$ (c).

2.5 Edge effects

In the RSA model, first, center coordinates are uniformly generated in a given window W and based on this centers, cylinders are placed. It may happen that a part of the cylinder, which has center outside W , is present inside the window W . This will create edge effects in simulated realizations. This can be corrected using plus sampling, i.e., simulate cylinders in an appropriately enlarged window and consider only cylinders and cylinder parts within W . Another approach is periodic edge treatment, i.e., simulate cylinders in W and allow cylinders to enter into the window from opposite edges of W . Edge correction is illustrated in Figure 2.3.

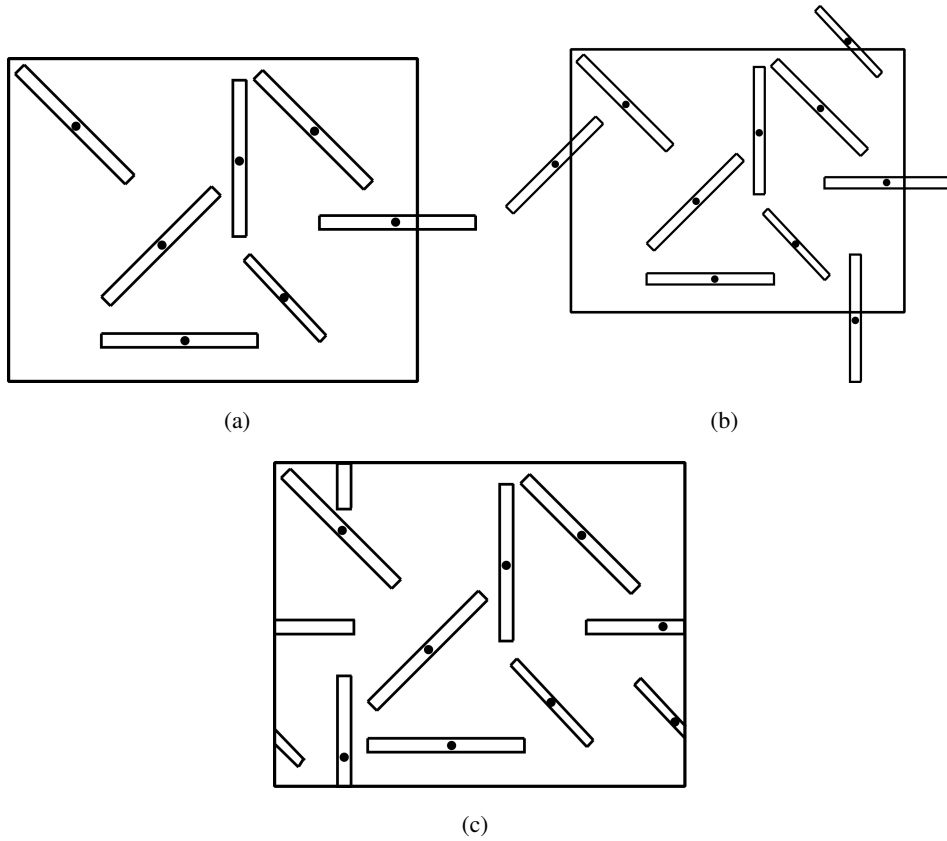


Figure 2.3 – Illustration for edge correction. (a) No edge correction (b) Edge correction: plus sampling (C) Edge correction: periodic edge treatment

2.6 Image data

Let us define an n -dimensional homogeneous lattice $\mathbb{L}^n \subset \mathbb{R}^n$ as

$$\mathbb{L}^n = \left\{ x \in \mathbb{R}^n : x = \sum_{i=1}^n \lambda_i u_i, \lambda_i \in \mathbb{Z} \right\} = U\mathbb{Z}^n$$

where $u_1, u_2, \dots, u_n \in \mathbb{R}^n$ form a basis of \mathbb{R}^n and $U = \{u_1, \dots, u_n\}$ is the matrix of column vectors.

An n -dimensional image I is a function from a subset V of the lattice \mathbb{L}^n to the set of pixel values P and it is defined as

$$I : V \rightarrow P$$

For 3D images, a pixel is also called a voxel. Images are classified according to values of P . Some of the image types are given in Table 2.1.

Furthermore, the connectivity of neighboring pixels is important in image processing. It is defined using the adjacency system \mathbb{F} of the lattice \mathbb{L}^n . In order to define \mathbb{F} , we introduce some of the basic notations in the following.

binary images	$P = \{0, 1\}$
8-bit gray value images	$P = \{0, \dots, 255\}$
16-bit gray value images	$P = \{0, \dots, 65535\}$
float images	$P = \mathbb{R}$

Table 2.1 – Image types

The closed unit cell C of \mathbb{L}^n with respect to the basis u_1, u_2, \dots, u_n is defined by $C = [0, u_1] \oplus \dots \oplus [0, u_n]$ where $[0, u_i]$ is the segment between the origin 0 and the lattice point u_i . Let $\mathbb{F}_{\text{loc}} \subseteq \{F_0, \dots, F_l\}$ be a set of convex polytopes with $F_i \subseteq C$ and $\mathcal{F}^0(F_i) \subseteq \mathcal{F}^0(C) = U \cdot \{0, 1\}^n$, $i = 1, \dots, l$, and $F_0 = \emptyset$, where \mathcal{F}^0 is the set of vertices of a polyhedron. The \mathbb{F}_{loc} is called a local adjacency system of the lattice \mathbb{L}^n (Ohser and Schladitz 2009 Chapter 3) if

- $\emptyset \in \mathbb{F}_{\text{loc}}$ and $C \in \mathbb{F}_{\text{loc}}$
- if $F \in \mathbb{F}_{\text{loc}}$ then $\mathcal{F}^i(F) \subset \mathbb{F}_{\text{loc}}$ for $i = 0, \dots, \dim F$ where $\mathcal{F}^i(F)$ is the set of all i -dimensional faces of F .
- if $F_i, F_j \in \mathbb{F}_{\text{loc}}$ and convex hull of $F_i \cup F_j$ is not in \mathbb{F}_{loc} then $F_i \cap F_j, \overline{F_i \setminus F_j}, \overline{F_j \setminus F_i} \in \mathbb{F}_{\text{loc}}$.
- if $F_1, \dots, F_m \in \mathbb{F}_{\text{loc}}$ and $F = \bigcup_{j=1}^m F_j$ is convex then $F \in \mathbb{F}_{\text{loc}}$, $m = 2, \dots$, cardinality of \mathbb{F}_{loc} .

An adjacency system \mathbb{F} of lattice \mathbb{L}^n is defined as

$$\mathbb{F} = \bigcup_{x \in \mathbb{L}^n} (\mathbb{F}_{\text{loc}} + x) \quad (2.6)$$

and note that $\mathcal{F}^0(\mathbb{F}) = \mathbb{L}^n$ (Ohser and Schladitz 2009 Chapter 3).

The neighbourhood graph Γ of \mathbb{F} is defined as $(\mathcal{F}^0(\mathbb{F}), \mathcal{F}^1(\mathbb{F}))$ where $\mathcal{F}^0(\mathbb{F})$ denotes vertices and $\mathcal{F}^1(\mathbb{F})$ denotes edges. The connectivity of \mathbb{L}^n is the order of the vertices in Γ .

The discretization $X \sqcap \mathbb{F}$ of a compact subset $X \subset \mathbb{R}^n$ with respect to a given adjacency system \mathbb{F} is given by (Ohser and Schladitz 2009 Chapter 3)

$$X \sqcap \mathbb{F} = \bigcup \{F \in \mathbb{F} : \mathcal{F}^0(F) \subseteq X\}. \quad (2.7)$$

2.6.1 Median filter

Let I be a 3D image. The median filter replaces a pixel by the median of all pixels in a window W , i.e.,

$$\tilde{I}(x, y, z) = \text{median}\{I(i, j, k), (i, j, k) \in W\} \quad (2.8)$$

where W represents the window centered at the pixel (x, y, z) .

3

Stochastic modeling of three-dimensional fiber systems incorporating interaction

In this chapter, the virtual microstructure generation for nonwoven filter media is considered. The stochastic fiber model from Altendorf and Jeulin 2011a is extended to generate fiber systems with fiber interaction. Parts of this chapter were published in Easwaran et al. 2015 and Easwaran et al. 2016a.

One of the earliest models for overlapping fiber systems has been introduced by Matheron 1975. It creates straight cylinders of infinite length using the dilated Poisson line process. Tomadakis and Sotirchos 1991 modeled fiber systems with overlapping fibers by distributing cylinders randomly in d ($d = 2$ or 3) directions, that is, with their axes perpendicular to one direction ($d = 2$) or in the three-dimensional (3D) space without preferred orientation ($d = 3$). Later Schladitz et al. 2006 used Poisson lines dilated by spheres to generate the microstructure of a nonwoven fibrous medium from Polyethylene terephthalate (PET). A study on acoustic properties of this microstructure model was carried out. A microstructure model for materials which are used for the gas diffusion layer in proton exchange membrane fuel cells based on dilated Poisson line tessellations was developed by Thiedmann et al. 2008. Peyrega et al. 2009 proposed a Boolean model of random cylinders to simulate the microstructure of Thermisorel (boards made of recycled wooden fibers by a paper making process). Both the Poisson line and the Boolean cylinder approach generate fiber systems of overlapping fibers.

The random sequential adsorption (RSA) model to create systems of non-overlapping objects was introduced by Feder 1980. Precisely, Feder proposed to randomly place disks on a surface. In order to achieve a non-overlapping system of disks, the RSA method places a disk only if it does not overlap with any previously simulated object. This process continues until a desired area fraction has been reached. This technique has been used in many publications to model systems of non-overlapping objects. Recently, Pan 2010, Redenbach and Vecchio 2011, and Naddeo et al. 2014 generated systems of straight fibers for various applications by applying the RSA scheme to cylinders. For instance, Redenbach and Vecchio 2011 fitted RSA models to specimens of glass fiber reinforced polymer and steel fiber reinforced ultra-high performance concrete. In general, only low volume fractions can be achieved by the RSA procedure. For example, we can only attain a volume fraction of about 10% – 15% for fiber systems with isotropic orientation distribution and

a fiber aspect ratio of 10.

All references mentioned above dealt with straight fibers. Modeling of fiber systems with curved fibers has also been considered in the literature. A bending fiber model for wood fibers was proposed by Faessel et al. 2005. This technique is based on dilated curved lines made of curvature points connected by spline interpolation. Wirjadi 2009 introduced another method to generate bending fiber systems of overlapping fibers using random walks with the von Mises-Fisher distribution. Since in this method, long fibers may bend to a circle, the orientation distribution of the simulated fiber system cannot be controlled. Kärkkäinen et al. 2009 and Kärkkäinen et al. 2012 developed a two-dimensional (2D) model based on 2D random walks with the multivariate von Mises-Fisher distribution, which also effectively controls the deviation of local fiber orientation from its main orientation. In the recent work of Gaiselmann et al. 2012, a stochastic model for fiber systems with curved and overlapping fibers using random polygonal tracks was developed. Fibers generated by this procedure are oriented in the xy -plane. The proposed model is fitted to the microstructure of a nonwoven fibrous medium from the gas diffusion layer in polymer electrolyte membrane fuel cells.

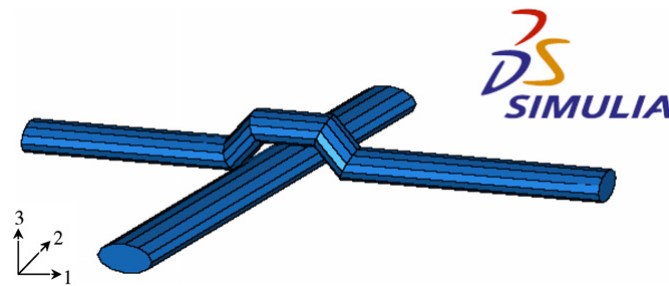


Figure 3.1 – Curved fiber modeled by a chain of polyhedra with elliptical cross-section. 1, 2, and 3 denote x -axis, y -axis, and z -axis, respectively. Reprinted from Composites Science and Technology, 68/13, Y. Pan, L. Iorga, A. A. Pelegri, Numerical generation of a random chopped fiber composite RVE and its elastic properties, 2792–2798, Copyright (2008), with permission from Elsevier.

Pan et al. 2008 proposed a model for non-overlapping fiber systems with curved fibers. A curved fiber is modeled as a chain of irregular polyhedra with elliptical cross-section (see Figure 3.1). Volume fractions of 35% – 40% can be achieved by this method. Nevertheless, fibers generated by the clumped polyhedra do not appear to be very realistic. Recently, a stochastic model for non-overlapping fiber systems with curved fibers was developed by Altendorf and Jeulin 2011a. In this technique, fibers are represented as chains of spheres. The modeling of chains of non-overlapping spheres is already considered by Karayiannis and Laso 2008. However, the method from Karayiannis and Laso 2008 is not appropriate for modeling of fibers, because the restrictions on the chain structure during the simulation steps are too low. Altendorf and Jeulin 2011a model the initial configuration of the system using random walks, where the fiber bending is controlled by two parameters (κ_1 and κ_2) in the multivariate von Mises–Fisher distribution. Fiber systems simulated by random walks may contain overlapping fibers. Subsequently, a variant of the force

biased packing algorithm for spheres introduced by Mościński and Bargieł 1989 is applied to obtain the non-overlapping configuration. The proposed modeling approach can be used to generate fiber systems with high volume fractions that were previously out of reach. Altendorf and Jeulin 2011a have achieved volume fractions of up to 72% for a z-axis preferred orientation distribution and an aspect ratio of 9. Altendorf and Jeulin 2011b and Altendorf et al. 2014 fitted this model to samples of a real glass fiber reinforced polymer.

Gaiselmann et al. 2013 proposed another non-overlapping fiber model for bending fibers. This is an extension of the overlapping fiber model introduced by Gaiselmann et al. 2012. An overlapping fiber system is generated using the method from Gaiselmann et al. 2012. Additionally, they have also included fiber bundles in the initial configuration. Subsequently, the force biased packing algorithm is used to transform the system of overlapping fibers into a non-overlapping fiber system. Recently, a modified version of the algorithm from Altendorf and Jeulin 2011a was presented by Chapelle et al. 2015. In the modified approach, fibers are modeled as chains of spherocylinders rather than sphere chains. This approach has been used to generate the virtual microstructure of mineral wool.

As we already mentioned in the introduction of this thesis, nonwoven filter media which we consider in this thesis, prominently feature (see Figure 1.3)

- (a) non-overlapping fibers
- (b) curved fibers
- (c) fibers with circular cross section
- (d) fibers of apparently infinite length
- (e) fiber bundles

In order to generate virtual microstructure realizations for nonwoven filter media, we require a stochastic model incorporating the above mentioned properties. Even though the fiber bundle model proposed by Gaiselmann et al. 2013 includes properties (a)-(c) and (e), we cannot consider their approach because the fiber orientation distribution of this model is limited to the xy -plane. Moreover, fiber bundles of this approach only consist of parallel fibers, whereas, nonwovens feature fiber bundles with slightly entwined fibers rather than parallel fibers.

Since fiber main orientation and curvature of a fiber can be controlled effectively in the stochastic model proposed by Altendorf and Jeulin 2011a, as part of this thesis, the Altendorf-Jeulin approach will be extended to model microstructures for nonwoven materials. The Altendorf-Jeulin model already incorporates features (a)-(c). We apply several modifications to the Altendorf-Jeulin method to include properties (d) and (e). The alterations are listed in the following:

- The initial fiber configuration is created by extending fibers in two directions rather than just one direction.
- Fiber bundles are introduced in the fiber system.
- Plus sampling is used for edge correction.

In this thesis, we simulate realizations of larger domains (up to $2000 \times 2000 \times 2000$ voxels), whereas Altendorf and Jeulin 2011a considered domain size up to $400 \times 400 \times 400$ voxels.

The rest of the chapter is organized as follows. Section 3.1 describes the fiber model by Altendorf and Jeulin 2011a. In Section 3.2, we extend the Altendorf-Jeulin approach to generate fiber system with endless fibers. We develop the stochastic model for non-overlapping fiber systems incorporating fiber bundles in Section 3.3.

3.1 The Altendorf-Jeulin model for dense fiber systems

In this section, Altendorf-Jeulin stochastic model for dense fiber systems is discussed. In this approach, a fiber is represented as a chain of spheres (see Figure 3.2). The initial configuration of a fiber system is simulated using random walks in 3D space. In the initial system, fibers are allowed to overlap. Model parameters are used to control geometric properties such as fiber thickness, fiber orientation, curvature of a fiber, and so forth. Furthermore, the initial system of overlapping fibers is transformed into a non-overlapping configuration using the force biased fiber packing algorithm. Periodic edge treatment is considered throughout the modeling procedure. A detailed description of the Altendorf-Jeulin approach is given in the following.

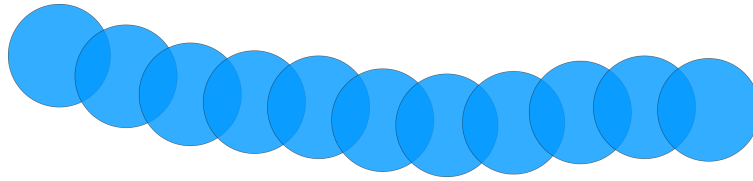


Figure 3.2 – Chain of spheres

Input parameters to create fiber systems using this technique are the sampling window W , the number of fibers N , the distributions of fiber radius, length, orientation, and curvature. Particularly, this approach considers the Schladitz distribution given in Chapter 2 Subsection 2.2.1 with parameter β to generate the main fiber orientation. And, the fiber bending is controlled by the multivariate von Mises-Fisher distribution (see Chapter 2 Subsection 2.2.3) with parameters κ_1 and κ_2 .

Let us denote the fiber system P as

$$P = \bigcup_{j=1}^N P_j \quad (3.1)$$

where P_j is the j -th fiber of the system. It is denoted as a chain of spheres, i.e., $P_j = \{p_{j1}, \dots, p_{jl_j}\}$ with $p_{ji} = (x_{ji}, \mu_{ji}, r_{ji})$ where $x_{ji} \in \mathbb{R}^3$, $\mu_{ji} \in S^2$ (unit sphere), and $r_{ji} \in \mathbb{R}_{>0}$ are center position of the sphere, local orientation of the fiber and radius of the sphere, respectively. There are $l_j \in \mathbb{N}$ spheres in the j -th fiber. The number of spheres l_j of a fiber is determined from the fiber's length. Radii also influence l_j because each sphere's radius will be used to calculate the distance between neighboring spheres in the chain. In general, the length and radius can be varied for each fiber.

In order to generate the j -th fiber, first, the length and radius r_j of the fiber are simulated from the respective distributions on $\mathbb{R}_{>0}$. Then, an initial sphere $p_{j1} = (x_{j1}, \mu_{j1}, r_{j1})$ is generated. The starting coordinate x_{j1} is uniformly distributed in a cubic window W with periodic edge treatment. The main orientation $\mu_{j1} \in S^2$ of the fiber follows the Schladitz distribution and $r_{j1} = r_j$.

To create a new sphere $p_{j(i+1)}$ during the random walk, the new local orientation $\mu_{j(i+1)}$ is generated using the multivariate von Mises-Fisher distribution (see Chapter 2 Subsection 2.2.3) with parameter μ_{j1} , μ_{ji} , κ_1 , and κ_2 where κ_1 is a reliability parameter with respect to the main orientation μ_{j1} and κ_2 is a reliability parameter with respect to the previous orientation μ_{ji} .

Thereby, each new fiber coordinate is computed as $x_{j(i+1)} = x_{ji} + \frac{r_j}{2} \mu_{j(i+1)}$. In addition, periodic boundary conditions are used to treat the spheres which are created outside the sampling window.

The mean orientation of the generated fiber $P_j = \{p_{j1}, \dots, p_{jl_j}\}$ is defined as $\bar{\mu}(P_j) = \frac{p_{jl_j} - p_{j1}}{|p_{jl_j} - p_{j1}|} \in S^2$. It may deviate from the main orientation μ_{j1} depending on the reliability parameters κ_1 and κ_2 . In order to retain the main fiber orientation μ_{j1} without changing fiber length, radius and bending, the fiber P_j is rotated. This rotation is achieved by adapting every sphere $p_{ji} = (x_{ji}, \mu_{ji}, r_{ji})$ to $p'_{ji} = (x'_{ji}, \mu'_{ji}, r_{ji})$, using the initial coordinate x_{j1} and the angle α required to change the fiber's mean orientation $\bar{\mu}(P_j)$ to the desired main orientation μ_{j1} .

$$n = \mu_{j1} \times \bar{\mu}(P_j) \quad (3.2)$$

$$\alpha = \cos^{-1}(\mu_{j1} \cdot \bar{\mu}(P_j)) \quad (3.3)$$

$$Rot(\mu, n, \alpha) = (n \cdot \mu)n + \cos \alpha((n \times \mu) \times n) + \sin \alpha(n \times \mu) \quad (3.4)$$

$$x'_{ji} = x_{j1} + Rot(x_{ji} - x_{j1}, n, \alpha) \quad (3.5)$$

$$\mu'_{ji} = Rot(\mu_{ji}, n, \alpha) \quad (3.6)$$

where “ \cdot ” and “ \times ” denote scalar product and cross product, respectively, α denotes the angle between μ_{j1} and $\bar{\mu}(P_j)$, and n is normal to the plane containing μ_{j1} and $\bar{\mu}(P_j)$. In Equation (3.4), μ is rotated by an angle α about the axis n .

The aforementioned procedure is repeated for N fibers. This approach results in a system of bending fibers which may overlap (see Figure 3.3 (a)). This initial modeling phase is, therefore, followed by a second phase, which will remove any overlap from the system. This second phase is implemented

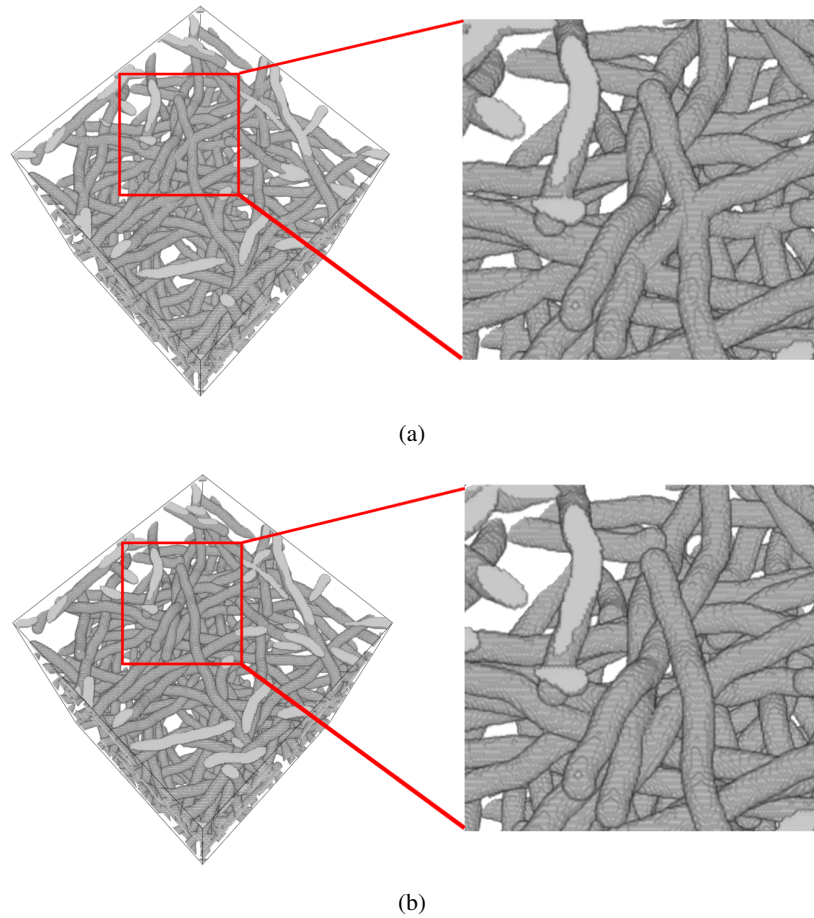


Figure 3.3 – Realizations of the fiber system from the Altendorf-Jeulin approach for input parameters: window size = 250^3 voxels, number of fibers = 80, $\beta = 10$, fiber radius = 5 voxels, $\kappa_1 = 10$, and $\kappa_2 = 100$. (a) Overlapping fiber system. (b) Non-overlapping fiber system.

by a modified version of the force biased packing algorithm for spheres developed by Mościński and Bargieł [1989](#) and statistically analyzed by Bezrukov et al. [2002](#). In the original algorithm, the repulsion force is applied to displace the overlapping spheres to a random position to avoid overlap. In the modified approach for fibers, the recover force is additionally introduced to preserve the fiber structure. Precisely, the repulsion and recover forces are applied to the sphere centers during force biased fiber packing to render the overlapping fiber system non-overlapping, while keeping the fibers intact. These forces do not act like mechanical forces. The repulsion force separates a pair of intersecting spheres which are not neighbors within the same fiber. For this purpose, the spheres are displaced to reduce overlap. The displacements are estimated from the amount of overlap. Meanwhile, the recover force preserves the fiber structure of the sphere chains. It maintains the distance and angle between neighboring spheres during displacement. The recover force is directly proportional to the displacement of the original sphere coordinate as an effect of the repulsion force. The fiber system after applying the force biased fiber packing is given in [Figure 3.3 \(b\)](#). The mathematical formulation of these forces is discussed by Altendorf and Jeulin [2011a](#) and it is summarized in the following.

The simulated overlapping fiber system can be represented by a graph $G = (P, E)$, where

$$P = \{p_{1,1}, p_{1,2}, \dots, p_{1,l_1}, p_{2,1}, \dots, p_{N,l_N}\} \subset \mathbb{R}^3 \times S^2 \times \mathbb{R}_{>0} \quad (3.7)$$

denotes the system of simulated spheres and

$$E = \{(p_{j,i}, p_{j,i+1}) | j \in \{1, \dots, N\}, i \in \{1, \dots, l_j\}\} \quad (3.8)$$

denotes the set of connections between the spheres. N is the number of fibers in a system and l_j is the number of spheres in the j -th fiber. Note that here we represent P and E as vertices and edges of a graph G , respectively. P given in Equation (3.1) and (3.7) are the same, it is just another way of writing. Let $C = \{(a, c, b) \in P^3 | (a, c) \in E \wedge (c, b) \in E\}$ denote the intersections between two edges. In other words, c is the connecting sphere for a and b . A graphical representation of the graph G is given in Figure 3.4.

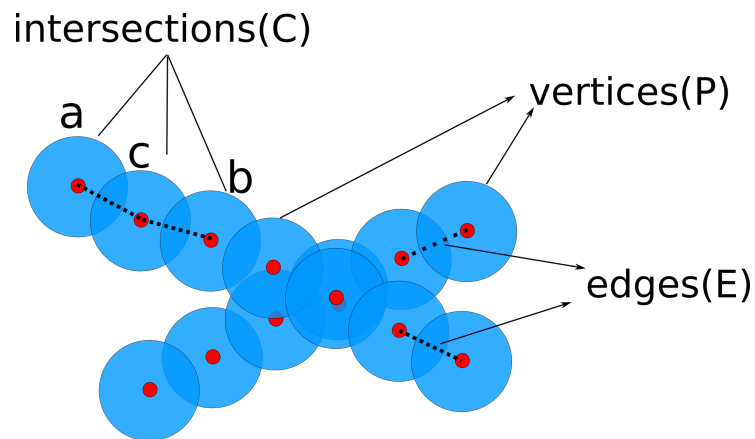


Figure 3.4 – Graph $G = (P, E)$ of a fiber system. Spheres are vertices P and connections between the spheres are edges E . a , c , and b are arbitrary spheres.

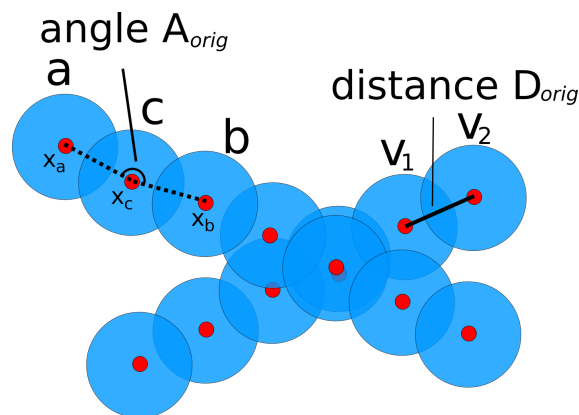


Figure 3.5 – The original distance $D_{orig}(v_1, v_2)$ and the original angle $A_{orig}(a, c, b)$.

Before applying the force biased fiber packing, compute the original distance D_{orig} between two neighboring spheres and the original angle A_{orig} in every joint as in the following (see Figure 3.5).

For $(v_1, v_2) \in E$,

$$D_{orig}(v_1, v_2) = |x_{v_1} - x_{v_2}| \tag{3.9}$$

For $(a, c, b) \in C$,

$$A_{orig}(a, c, b) = \angle(x_a, x_c, x_b) \tag{3.10}$$

Let $p = (x_p, \mu_p, r_p)$ and $q = (x_q, \mu_q, r_q)$ be arbitrary spheres in the fiber system P . The overlap between these two spheres is defined as

$$\text{Overlap}(p, q) = \max[0, r_p + r_q - d(x_p, x_q)]$$

where $d(x_p, x_q)$ is the distance between x_p and x_q . The graphical illustration is given in Figure 3.6.

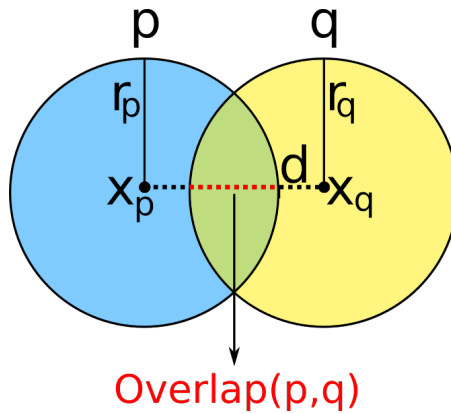


Figure 3.6 – The overlap between two spheres p and q .

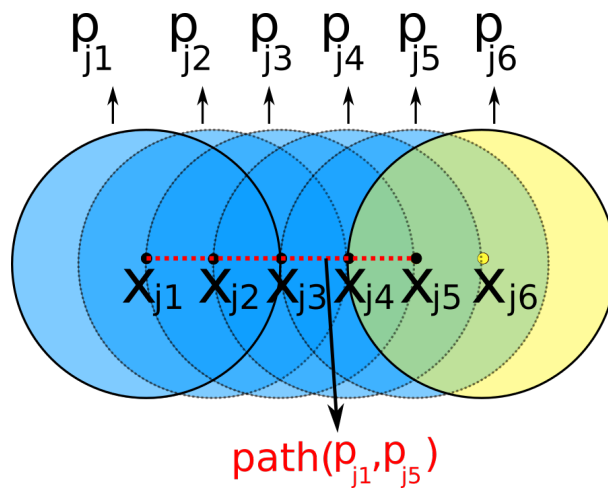


Figure 3.7 – Chain of spheres. The distance between sphere centers x_{j_i} and $x_{j_{i+1}}$ is $\frac{r_j}{2}$. The sphere p_{j1} is overlapping with spheres from p_{j2} to p_{j4} . The length of the path between spheres p_{j1} and p_{j5} is 4.

Repulsion force

The repulsion force is applied on a pair of spheres to make them non-overlapping. An overlap between the pair is permitted if two spheres are close neighbors in the same fiber. In other words, if the two spheres p and q are connected by a path of length less than or equal to 5, p and q are close neighbors. It is denoted as $p \sim q$:

$$p \sim q \Leftrightarrow \text{there exists a path between } p \text{ and } q \text{ with length } \leq 5. \quad (3.11)$$

Here, length of a path denotes the number of edges in the path. We already know from the model description that the distance between two consecutive sphere centers is half of the radius. Therefore, spheres in the same chain linked by a path with length less than 4 do overlap. This is shown in Figure 3.7. In order to accomplish small deviations in the radius or additional curvature, here the minimal path length is assumed to be 5.

The repulsion force is defined as

$$F_{RP}(p, q) = I_{p \sim q} \frac{\text{Overlap}(p, q)}{2} \frac{x_p - x_q}{|x_p - x_q|} \quad (3.12)$$

and is applied, if p is not a close neighbor of q in the same fiber (see Equation (3.11)).

The total repulsion force for the point p is given by

$$F_{RP}(p) = \sum_{q \in P} F_{RP}(p, q) \quad (3.13)$$

Recover force

The recover force is a combination of a spring force, which maintains the distance between the sphere centers in a fiber, and an angle force, which controls the angle between neighboring spheres in a fiber. When the recover force is applied on a sphere in a fiber, it induces a recover force on its neighboring spheres. Each neighboring sphere initiates a recover force on its neighbors, and this process never ends. Therefore, the friction factor is introduced to stabilize this process. The friction factor is given as

$$f_{\delta_s, \delta_e}(\delta) = \begin{cases} 0 & \text{if } \delta < \delta_s \\ \frac{1}{2} - \frac{1}{2} \cos\left(\frac{|\delta| - \delta_s}{\delta_e - \delta_s} \pi\right) & \text{if } \delta_s \leq \delta \leq \delta_e \\ 1 & \text{if } \delta_e < \delta \end{cases}$$

where δ_s and δ_e are changes in distance or angle. δ_s is a minimal change which is needed to induce a force and δ_e is a change when the force attains its full strength.

Recover spring force: The recover spring force F_{RS} is applied to preserve distance between the spheres of the fiber. F_{RS} on a sphere $p \in P$ is defined as

$$F_{RS}(p) = \sum_{q \in P} \left\{ [I_E(p, q) + I_E(q, p)] f_{\delta_s, \delta_e} \left(\frac{|\Delta D(q, p)|}{D_{orig}(q, p)} \right) \times [\Delta D(q, p)] \vartheta(p, q) \right\} \quad (3.14)$$

where

$$\Delta D(q, p) = D_{orig}(q, p) - |x_q - x_p|$$

denotes the change of distance and

$$\vartheta(p, q) = \frac{x_p - x_q}{|x_p - x_q|}$$

denotes the unit vector for the direction of the force. For realizations simulated in this thesis, the friction parameters δ_s and δ_e for spring forces are fixed as 0.05 and 0.10, respectively (same as in Altendorf and Jeulin 2011a).

Recover angle force: The recover angle force is applied to maintain the angle between sphere joints and it is defined on each sphere having two direct neighbors. Let $(a, p, b) \in C$, i.e., a and b are the adjacent spheres of the sphere p . These sphere centers are shown in Figure 3.8 (a). The formula to compute the angle at x_p is derived as in the following:

- Let the point m be an intersection point of the plane passing through the point x_p and perpendicular to the vector $(x_a - x_b)$ and the line between x_a and x_b (refer Figure 3.8 (b)).
- Compute the distance between m and x_a , i.e., $h_1 = |m - x_a|$, distance between m and x_b , i.e., $h_2 = |m - x_b|$, and distance between m and x_p , i.e., $z = |m - x_p|$ (refer Figure 3.8 (c)).
- Compute

$$\alpha_1 = \tan^{-1} \left(\frac{h_1}{z} \right) \quad (3.15)$$

$$\alpha_2 = \tan^{-1} \left(\frac{h_2}{z} \right) \quad (3.16)$$

From Equation (3.15) and (3.16), the angle α at x_p can be written as (refer Figure 3.8 (d))

$$\begin{aligned} \tan(\alpha) &= \tan(\alpha_1 + \alpha_2) \\ &= \frac{z(h_1 + h_2)}{z^2 - h_1 h_2} \\ \alpha &= \tan^{-1} \left(\frac{z(h_1 + h_2)}{z^2 - h_1 h_2} \right) \end{aligned} \quad (3.17)$$

Note that we already have the original angle α_0 at x_p which is computed before applying any forces (see Equation (3.10)). Furthermore, we define distance z_0 from the point m to a point $x_{\bar{p}}$ in such a way that $\angle(x_a, x_{\bar{p}}, x_b) = \alpha_0$ using Equation (3.17) (refer Figure 3.8 (e))

$$z_0 = \frac{h_1 + h_2 + \sqrt{(h_1 + h_2)^2 + 4h_1 h_2 \tan^2 \alpha_0}}{2 \tan \alpha_0}$$

In the computation of the recover angle force, z_0 will be used to compute the necessary length to displace the sphere p in order to retain the original angle α_0 . The recover angle force F_{RA} on a sphere p is given as

$$F_{RA}(p) = I_{\exists a, b \in P, (a, p, b) \in C} f_{\delta_s, \delta_e}(\alpha_0 - \alpha)(z - z_0) \vartheta(m, p) \quad (3.18)$$

where a and b are the direct neighbors of p , and $\vartheta(m, p)$ is the unit vector for the direction of the force, and \cdot . For realizations generated in this thesis, the friction parameters δ_s and δ_e for angle forces are chosen as 0.1° and 0.2° (same as in Altendorf and Jeuin 2011a).

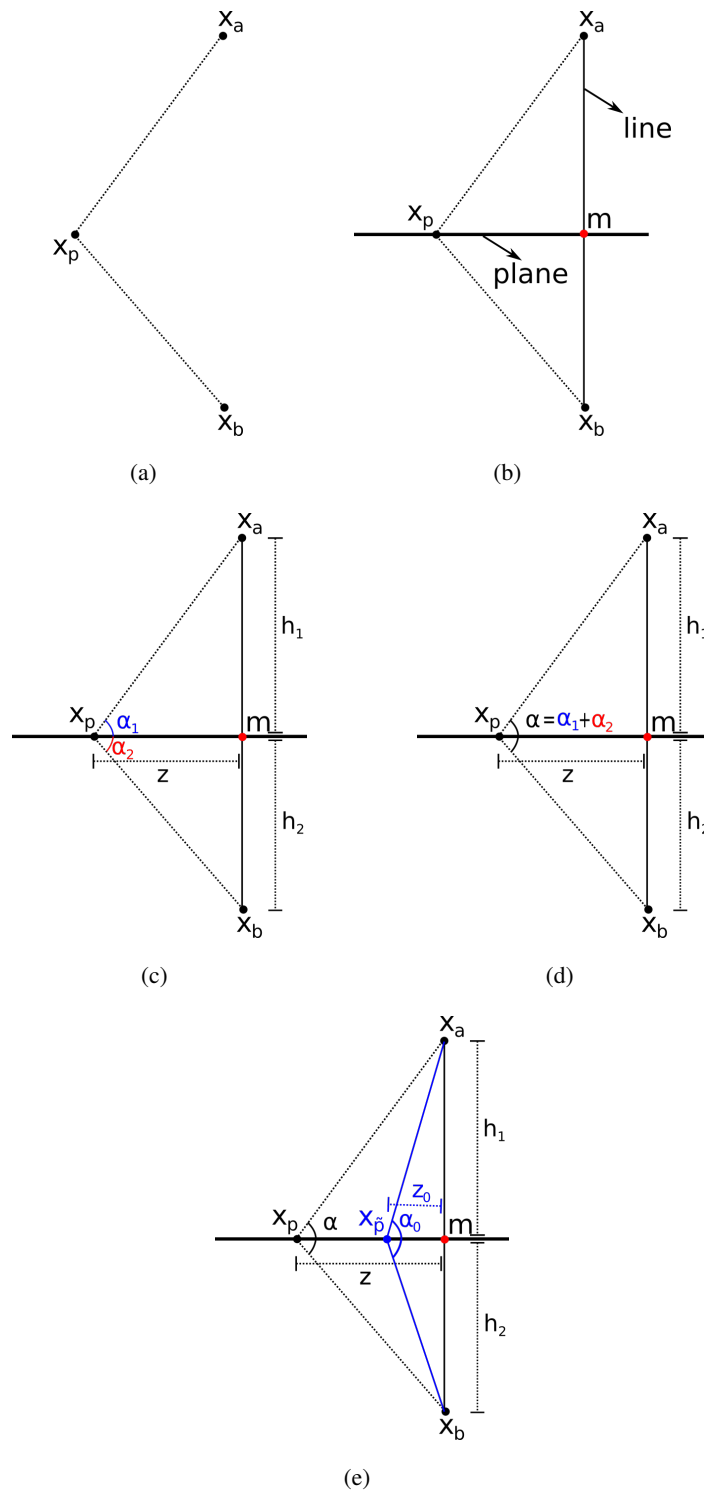


Figure 3.8 – Angle force geometry.

The total force on an arbitrary sphere $p = (x_p, \mu_p, r_p) \in P$ is defined as

$$F_{total}(p) = F_{RP}(p) + \rho F_{RS}(p) + \rho F_{RA}(p) \quad (3.19)$$

where $\rho \in [0, 1]$ is a factor to smooth the development of recover forces and favor the repulsion forces in the initial steps. $\rho = 0.5$ is used for realizations created in this thesis. The upper bound F_{max} for the final force strength F_{final} to limit the possible displacement of a sphere is defined.

$$F_{final}(p) = \frac{F_{total}(p)}{|F_{total}(p)|} \min(|F_{total}(p)|, F_{max}) \quad (3.20)$$

In every step, the sphere center x_p is displaced by the final force:

$$x'_p = x_p + F_{final}(p) \quad (3.21)$$

Systems of non-overlapping fibers with high volume fractions can be achieved by this modeling approach (see Figure 3.9). Furthermore, fiber orientation distributions and fiber bending can be controlled effectively.

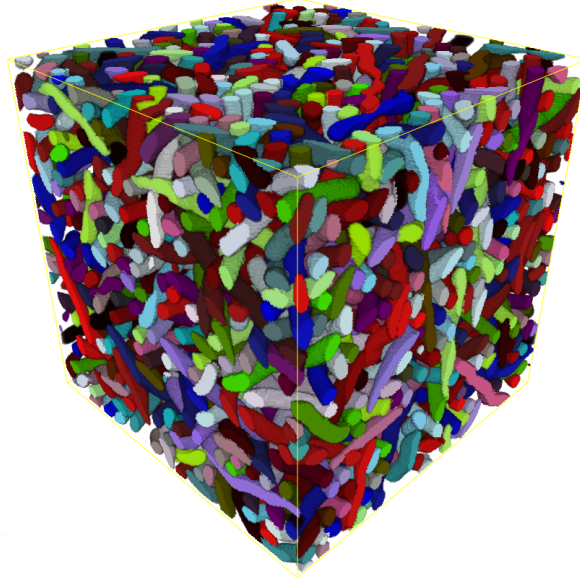


Figure 3.9 – Realization of a packed fiber system. Model parameters: Window size = 250^3 voxels, number of fibers = 300, isotropic orientation ($\beta = 1$), constant fiber length = 300 voxels, fiber radius = 5 voxels, and bending parameters $\kappa_1 = 10$ and $\kappa_2 = 100$. Volume fraction = 46%. Higher volume fractions can be achieved for anisotropic orientation distributions or shorter fibers.

3.2 Modeling of fiber systems with endless fibers

In this section, we extend the algorithm of Altendorf and Jeulin 2011a to generate fiber systems with endless fibers. In the aforementioned procedure, each fiber is simulated by following the main fiber direction from its starting coordinate x_{j1} . Since x_{j1} is uniformly distributed in the sampling window,

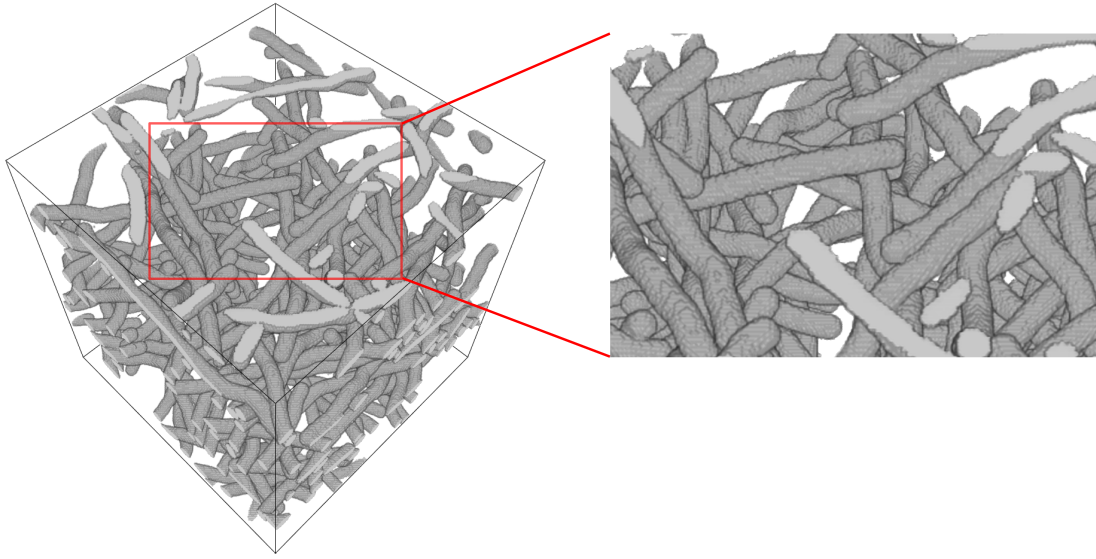


Figure 3.10 – 3D realization of a fiber system simulated using the Altendorf-Jeulin model. Fiber end points are visible in the observation window.

naturally one end of the fiber is in the observation window. If the other end of the fiber grows beyond the boundaries of the sampling window, periodic edge treatment is used to bring it back into the window. Hence, both ends of all fibers are visible in the observation window (see Figure 3.10). In order to obtain fiber systems with endless fibers, each fiber in an initial configuration is simulated using random walks in two directions starting at their centers until it hits the sampling window boundaries. Finally, the overlapping fiber system is transformed into a non-overlapping system using force biased fiber packing as described in Section 3.1.

The input to our modeling procedure consists of the sampling window W , the number of fibers N , the distribution of fiber radius, the parameter β for the Schladitz distribution to generate the main fiber orientation and the parameters κ_1 and κ_2 for the multivariate von Mises-Fisher distribution to control fiber bending. Note that here we do not require fiber length as an input parameter whereas the Altendorf-Jeulin model takes this as an input parameter. Here, plus sampling is used to avoid edge effects, i.e., simulating fibers in an appropriately enlarged window W' and considering fibers in the given sampling window W as the result. We obtain W' by enlarging all sides of the window W . We have tested edge effects with respect to the volume fraction for several sampling windows of side lengths from 250 voxels to 2000 voxels. The test results for input fiber radius 5 voxels show that the preferable length for enlargement is 100 voxels.

As in the previous section, here also we denote the fiber system as

$$P = \bigcup_{j=1}^N P_j$$

and the j -th fiber is represented as $P_j = \{p_{j1}, \dots, p_{jl_j}\}$ where $p_{ji} = (x_{ji}, \mu_{ji}, r_{ji}) \in \mathbb{R}^3 \times S^2 \times \mathbb{R}_{>0}$.

There are $l_j \in \mathbb{N}$ spheres in the j -th fiber. The radius r_j of the j -th fiber follows some distribution on $\mathbb{R}_{>0}$.

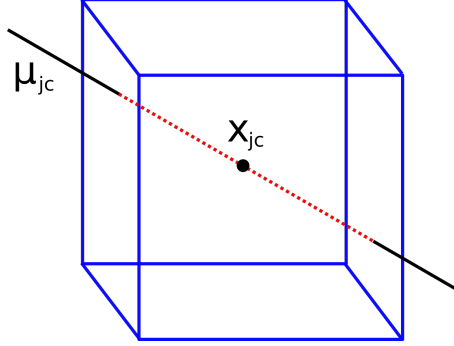


Figure 3.11 – Generation of center coordinate x_{jc} .

Simulation of the j -th fiber is described in the following:

- The center sphere of the j -th fiber is denoted as $q_{jc} = (x_{jc}, \mu_{jc}, r_{jc}) \in \mathbb{R}^3 \times S^2 \times \mathbb{R}_{>0}$ where x_{jc} is the sphere coordinate, μ_{jc} is the local orientation, and r_{jc} denotes the radius. The μ_{jc} is considered to be the main orientation of the j -th fiber.
- Generate the center sphere q_{jc} as in the following:
 - Generate μ_{jc} using the Schladitz distribution defined in Chapter 2 Subsection 2.2.1. This distribution generates the orientation based on the parameter β .
 - A random uniform line of infinite length with orientation μ_{jc} is generated in a window W' .
 - The midpoint of the segment of this line within W' is considered as center coordinate x_{jc} of the j -th fiber (refer Figure 3.11).
 - Let $r_{jc} = r_j$.

- The generated center sphere q_{jc} is illustrated in Figure 3.12 (a).

- The next sphere $q_{j f_1} = (x_{j f_1}, \mu_{j f_1}, r_{j f_1})$ is defined as

$$x_{j f_1} = x_{jc} + \frac{r_j}{2} \mu_{j f_1} \quad (3.22)$$

where the multivariate von Mises-Fisher distribution with parameters μ_{jc} , μ_{jc} , κ_1 , and κ_2 is used to find the next local orientation $\mu_{j f_1}$, and $r_{j f_1} = r_j$ (see Figure 3.12 (b)).

- The $(s + 1)$ -th sphere $q_{j f_{s+1}} = (x_{j f_{s+1}}, \mu_{j f_{s+1}}, r_{j f_{s+1}})$ along the line of the fiber main direction is given as

$$x_{j f_{s+1}} = x_{j f_s} + \frac{r_j}{2} \mu_{j f_{s+1}} \quad (3.23)$$

where the multivariate von Mises-Fisher distribution with parameters μ_{jc} , $\mu_{j f_s}$, κ_1 and κ_2 is used to obtain the next local orientation $\mu_{j f_{s+1}}$, and $r_{j f_{s+1}} = r_j$ (see Figure 3.12 (c)).

- Further spheres are generated until it reaches the boundaries of the window W' (see Figure 3.12 (d)).
- Once the fiber end reaches the boundary, the next sphere is simulated from the center coordinate x_{jc} along the line of the inverted main fiber direction. That is, the new sphere $q_{jb_1} = (x_{jb_1}, \mu_{jb_1}, r_{jb_1})$ is defined as

$$x_{jb_1} = x_{jc} + \frac{r_j}{2} \mu_{jb_1} \quad (3.24)$$

where the multivariate von Mises-Fisher distribution with parameters $-\mu_{jc}$, $-\mu_{jc}$, κ_1 , and κ_2 is utilized to compute the next local orientation μ_{jb_1} , and $r_{jb_1} = r_j$ (see Figure 3.12 (e)).

- The $(t + 1)$ -th sphere $q_{jb_{t+1}} = (x_{jb_{t+1}}, \mu_{jb_{t+1}}, r_{jb_{t+1}})$ along the line of the inverted main fiber direction is defined as

$$x_{jb_{t+1}} = x_{jb_t} + \frac{r_j}{2} \mu_{jb_{t+1}} \quad (3.25)$$

where the multivariate von Mises-Fisher distribution with parameters $-\mu_{jc}$, μ_{jb_t} , κ_1 , and κ_2 is used to compute the next local orientation $\mu_{jb_{t+1}}$, and $r_{jb_{t+1}} = r_j$ (see Figure 3.12 (f)).

- The sphere generation process stops once the chain reaches the window boundaries (see Figure 3.12 (g)).
- The simulated fiber is represented as $P_j = \{p_{j1}, \dots, p_{jl_j}\} = \{q_{jb_m}, \dots, q_{jb_1}, q_{jc}, q_{jf_1}, \dots, q_{jf_n}\}$ where n and m are the number of spheres along the line of the fiber main direction and its inverted direction, respectively.
- The simulated fiber P_j is rotated as described in Section 3.1 such that its mean orientation $\frac{p_{jl_j} - p_{j1}}{|p_{jl_j} - p_{j1}|} \in S^2$ equals the main fiber orientation μ_{jc} .

The modified fiber generation process, starting from the center instead of one end, allows for growing fibers up to the boundaries of the sampling window in a natural way. This procedure generates an overlapping fiber system in an extended window W' (see Figure 3.13(a)). The force biased fiber packing is applied to transform the resulting system into a non-overlapping fiber system (see Figure 3.13(b)) as described in Section 3.1. Finally, only fibers within the sampling window W are considered as the generated fiber system for the given input parameters.

Fiber systems with different orientations are shown in Figure 3.14. We have also simulated fiber systems of larger domain size up to 1000^3 voxels. A realization of a fiber system of domain size 1000^3 voxels is given in Figure 3.15.

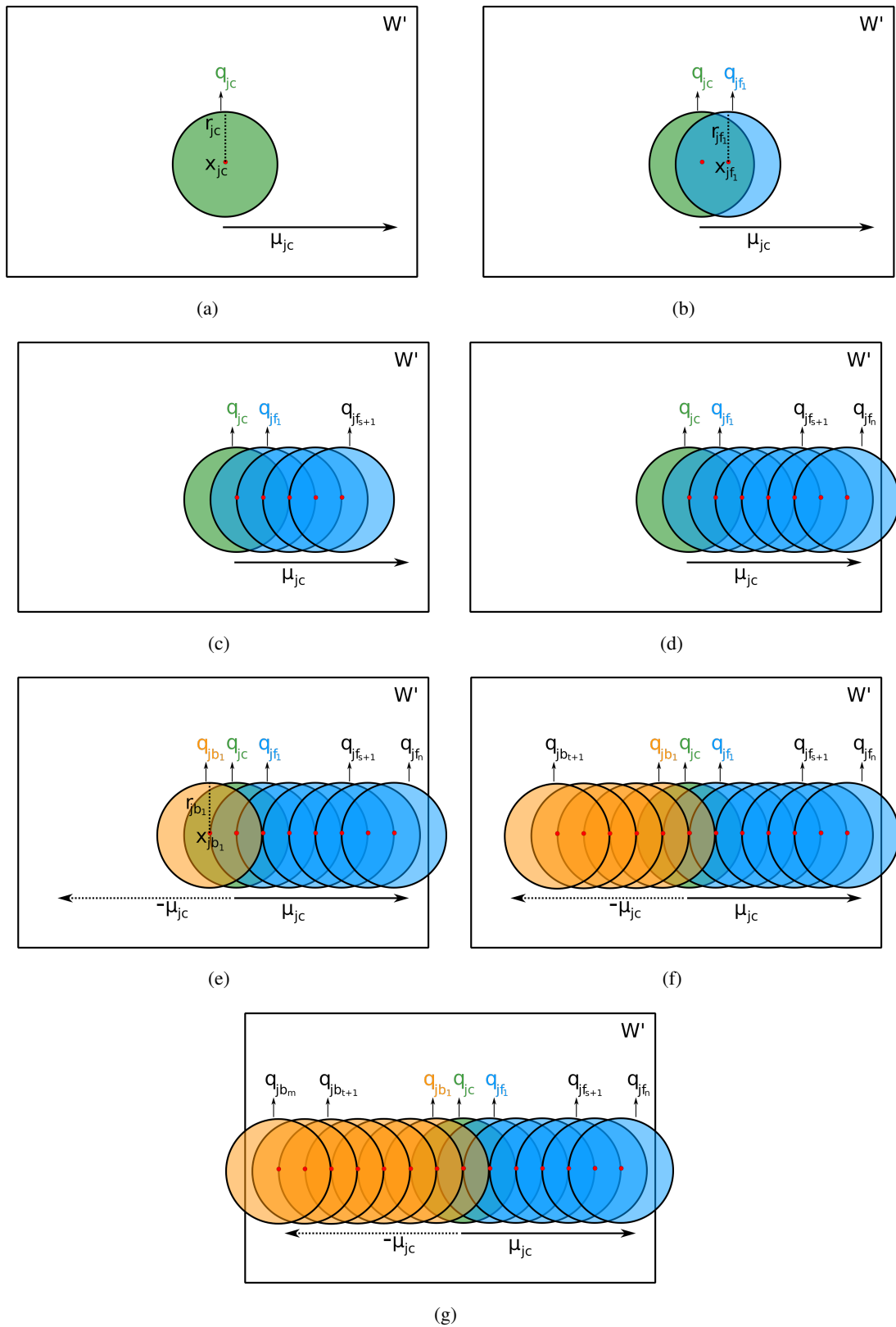


Figure 3.12 – Simulation of a fiber as a chain of spheres. (a) Center sphere. (b) New sphere along the line of the fiber main direction. (c) The $(s + 1)$ -th sphere along the line of the main direction. (d) Further spheres are generated until it reaches the boundaries. (e) New sphere along the line of the inverted fiber main direction. (f) The $(t + 1)$ -th sphere along the line of the inverted main direction. (g) Further spheres are generated until it reaches the boundaries.

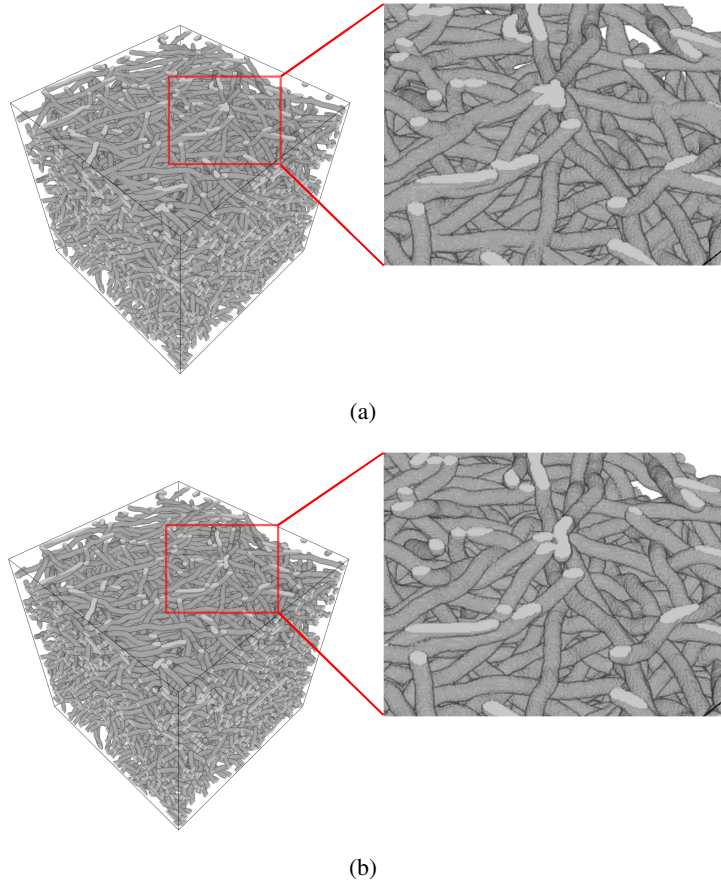


Figure 3.13 – Realizations of the fiber system with endless fibers for input parameters: window size = 250^3 voxels, number of fibers = 255, $\beta = 5$, fiber radius = 5 voxels, $\kappa_1 = 10$, and $\kappa_2 = 100$. (a) Overlapping fiber system in an extended window $W' = 450^3$. (b) Non-overlapping fiber system in an extended window $W' = 450^3$. Volume fraction = 20%

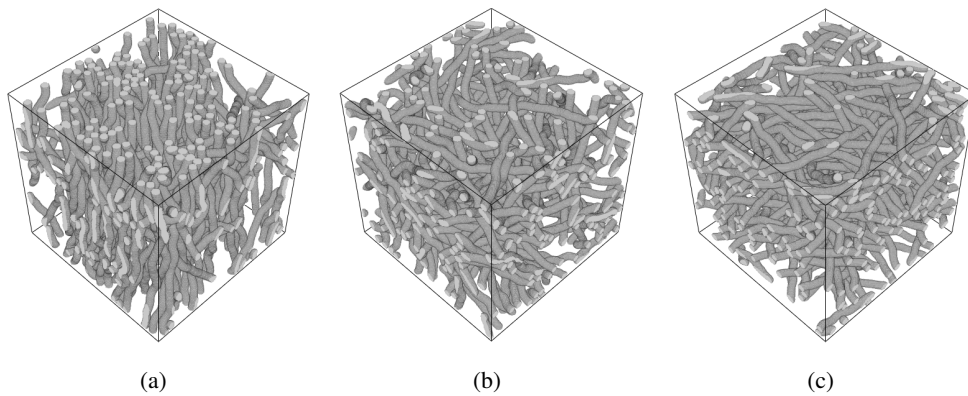


Figure 3.14 – Realizations of the fiber system with endless fibers for various β . (a) Orientation concentrated on the z -axis ($\beta = 0.1$) and volume fraction = 20%. (b) Isotropic orientation ($\beta = 1$) and volume fraction = 17%. (c) Isotropy within the xy -plane ($\beta = 5$) and volume fraction = 21%. Common parameters are window size = 250^3 voxels, fiber radius = 5 voxels, $\kappa_1 = 10$, and $\kappa_2 = 100$.

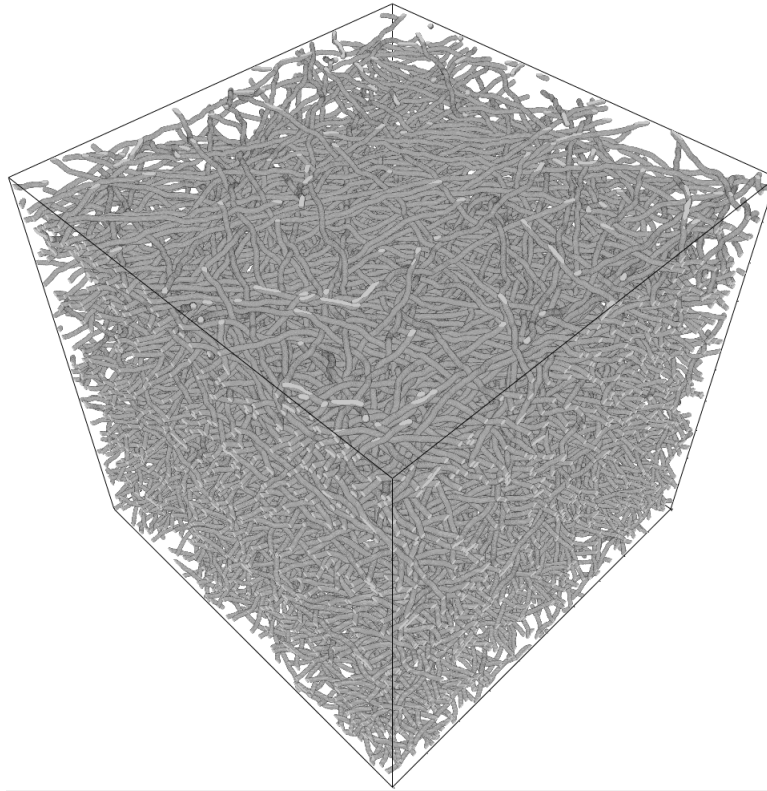


Figure 3.15 – Realization of the fiber system with endless fibers for input parameters: window size = 1000^3 voxels, volume fraction = 8%, $\beta = 5$, fiber radius = 5 voxels, $\kappa_1 = 10$, and $\kappa_2 = 100$.

The above described modeling technique step by step:

Input parameters: Sampling window size W , number of fibers N , radius distribution, parameter β for the Schladitz distribution to generate main fiber orientation, and parameters κ_1 and κ_2 for the multivariate von Mises-Fisher distribution.

Step 1: Compute the enlarged window W' by extending all six sides of the window W . Recommended length for enlargement is 100 voxels.

Step 2: Generate main fiber orientation μ_{jc} using the Schladitz distribution defined in Chapter 2 Subsection 2.2.1.

Step 3: Draw a uniform line of infinite length with orientation μ_{jc} in W' .

Step 4: Choose the midpoint x_{jc} of the segment of this line within W' .

Step 5: Generate the radius of a fiber using the given radius distribution.

Step 6: Grow the fiber starting from x_{jc} in two directions using κ_1 and κ_2 until it hits the boundaries of W' .

Step 7: Repeat Step 2 - 6 for all remaining fibers.

Step 8: Apply the force biased fiber packing.

Step 9: Output fibers within the sampling window W .

Stop criterion and end step

As discussed in Section 3.1, the repulsion and recover forces during the force biased fiber packing depend on the amount of overlap of the spheres. As mentioned earlier, after the random walk simulation, a fiber system contains a large number of overlapping spheres. Therefore, large displacements of spheres are occurring at the beginning of the force biased fiber packing. As soon as the size of an overlapping region is reduced, the spheres are less far displaced. The packing process should be stopped when displacement becomes negligible. For realizations generated in this work, the algorithm has been stopped when the total force strength $\sum_{p \in P} F_{total}(p)$ was less than $0.002 \times N \times s$ where N denotes the total number of fibers in the fiber system and s denotes the side length of the window (same as in Altendorf and Jeulin 2011a). In addition to that, to ensure that the final fiber system is non-overlapping, the maximum overlap of spheres is also checked. For all realizations considered in this thesis, maximum overlap should be less than $0.1r_{min}$, where r_{min} denotes the minimal radius in the system (same as in Altendorf and Jeulin 2011a). If displacement is not negligible before reaching 20000 iterations of the algorithm, it will be stopped unsuccessfully.

Consequently, the resulting successful fiber configurations may contain overlapping fibers. Hence, the radius of all overlapping spheres is reduced as follows.

The radius r of an arbitrary sphere $a = (x, \mu, r) \in P$ is reduced to

$$r' = r - \frac{1}{2} \left(\max_{p, q \in P, p \neq q} [\text{Overlap}(p, q)] \right)$$

If the precision of the radius distribution is important, repulsion forces can be used to make fibers non-overlapping. In this case, especially for dense fiber systems, it has to be checked manually that the sphere chains are not drawn apart.

Remark:

The just described endless fiber model is an improved version of our stochastic model proposed in Easwaran et al. 2016a.

3.3 Modeling of fiber systems incorporating interaction

In this section, the model for endless fibers from Section 3.2 is extended to include fiber bundles as observed in nonwoven filter media (see Figure 1.3). We propose two approaches to generate the initial configuration of the fiber system with fiber bundles. In both approaches, the initial fiber of a bundle is simulated as defined in the previous section. In the first approach, the following fibers of

a bundle are simulated using random walks which start from the initial coordinate of the first fiber along the line of its main direction. In the second approach, further fibers in a bundle are generated by duplicating sphere centers of the initial fiber. Finally, force biased fiber packing is applied to transform the initial configuration into a non-overlapping fiber system.

Input parameters for fiber bundle modeling are the sampling window W , the number of fibers N , the distribution of fiber radius, the parameter β to generate main fiber orientation, the parameters κ_1 and κ_2 for fiber bending, the frequency of fiber bundles, and the number of fibers in each bundle. As in the previous section, here also, the fiber system is simulated in the extended window W' .

Let us denote the fiber system with fiber bundles as

$$FS = \bigcup_{k=1}^{N_B} \bigcup_{j=1}^{N_k} P_{kj} \quad (3.26)$$

where k numbers bundles, j numbers fibers in the bundles, N_B denotes the total number of fiber bundles, and N_k denotes the number of fibers in the k -th bundle. N_B and N_k follow an arbitrary distribution in \mathbb{N} . Note that $N = \sum_{k=1}^{N_B} N_k$. The j -th fiber in the k -th bundle is represented as $P_{kj} = \{p_{kj1}, \dots, p_{kj}l_{kj}\}$ where $p_{kji} = (x_{kji}, \mu_{kji}, r_{kji}) \in \mathbb{R}^3 \times S^2 \times \mathbb{R}_{>0}$. l_{kji} denotes the number of spheres in the j -th fiber of the k -th bundle. The radius r_{kj} of the fiber P_{kj} follows an arbitrary distribution on $\mathbb{R}_{>0}$.

An initial fiber P_{k1} of the k -th bundle is generated by a random walk on both sides of its center sphere $q_{k1c} = (x_{k1c}, \mu_{k1c}, r_{k1c}) \in \mathbb{R}^3 \times S^2 \times \mathbb{R}_{>0}$ as described in Section 3.2. This initial fiber is represented as $P_{k1} = \{p_{k11}, \dots, p_{k1}l_{k1}\} = \{q_{k1b_m}, \dots, q_{k1b_1}, q_{k1c}, q_{k1f_1}, \dots, q_{k1f_n}\}$ where n and m is the number of spheres generated along the line of the fiber main direction and its inverted direction, respectively. We introduce the following two approaches to simulate the j -th fiber in the k -bundle.

Modeling of fiber bundles: Method I

- The initial sphere of the j -th fiber is denoted as $p_{kj1} = (x_{kj1}, \mu_{kj1}, r_{kj1}) \in \mathbb{R}^3 \times S^2 \times \mathbb{R}_{>0}$
- Choose first coordinate x_{k11} of the initial fiber of the k -th bundle as a starting coordinate x_{kj1} for the j -th fiber.
- Assign the main orientation of the initial fiber μ_{k11} as the main orientation μ_{kj1} of the j -th fiber.
- The $(i+1)$ -th sphere $p_{kj(i+1)} = (x_{kj(i+1)}, \mu_{kj(i+1)}, r_{kj(i+1)})$ of the j -th fiber is simulated as in the following

$$x_{kj(i+1)} = x_{kj1} + \frac{r_{kj}}{2} \mu_{kj(i+1)} \quad (3.27)$$

where $\mu_{kj(i+1)}$ is generated using the multivariate von Mises-Fisher distribution with parameter μ_{k11} , μ_{kji} , κ_1 , and κ_2 .

- Furthermore, if the newly created sphere $p_{kj(i+1)}$ does not touch the initial fiber P_{k1} during random walk simulation, in other words, if there is no $p_{k1i}, i = 1, \dots, l_{k1}$ such that $(r_{kj(i+1)} + r_{k1i} - |x_{kj(i+1)} - x_{k1i}|) \leq 0$, then displace the center $x_{kj(i+1)}$ of the sphere $p_{kj(i+1)}$ as in the following

$$x'_{kj(i+1)} = x_{kj(i+1)} + d(x_{kj(i+1)}, x_p) - (r_p + r_{kj(i+1)}) \frac{x_{kj(i+1)} - x_p}{|x_{kj(i+1)} - x_p|} \quad (3.28)$$

where

$$x_p = \operatorname{argmin}_{s=1, \dots, l_{k(j-1)}} d(x_{kji}, x_{k(j-1)s}) \quad (3.29)$$

r_p denotes radius of the sphere corresponding to x_p , $l_{k(j-1)}$ denotes the number of spheres in the previous fiber $P_{k(j-1)}$, $d(x, y)$ is the distance between x and y .

- If the newly created sphere $p_{kj(i+1)}$ is displaced, the recover force is applied as defined in (Equation (3.14) and (3.18)) to all previously simulated spheres $p_{kjt}, t = 1, \dots, i$ in the j -th fiber to maintain the chain structure.

Modeling of fiber bundles: Method II

- Sphere centers of the fiber P_{kj} is generated by duplicating sphere centers of an initial fiber P_{k1} and placing them parallel to the center line of an initial fiber with certain distance, i.e.,

$$x_{kji} = x_{k1i} + \mu_R r_{k1} \varepsilon \quad (3.30)$$

where μ_R is a random orientation which is perpendicular to the main orientation μ_{k1c} of an initial fiber and $\varepsilon \in [0, 1]$.

- The local orientation $\mu_{kji} = \mu_{k1i}$ and $r_{kji} = r_{kj}$.
- If the radius r_{k1} of the initial fiber is greater than r_{kj} , the distance between x_{kji} and $x_{kj(i+1)}$ for $i = 1, \dots, l_{kj}$ is greater than $r_{kj}/2$. This may result in a disconnected sphere chain. Therefore, new spheres are inserted between x_{kji} and $x_{kj(i+1)}$ until the distance between newly inserted spheres and $x_{kj(i+1)}$ are less than $r_{kj}/2$.

Force biased fiber packing

The two procedures mentioned above generate an overlapping fiber system with fiber bundles. The goal of these procedures is to deliberately simulate overlapping fibers since these will result in close fiber bundles after the force biased packing procedure.

Then, the force biased fiber packing is applied to transform the resulting system into a non-overlapping fiber system as described in Section 3.1. Lastly, fibers within the observation window W are treated as the simulated fiber system for the given input parameters. Some generated fiber systems with fiber bundles using Method I are shown in Figure 3.16. Similarly, fiber systems from

Method II are given in Figure 3.17.

Both methods can be used to model fiber systems with fiber bundles of entwined fibers. Furthermore, Method II can also be used to simulate fiber systems with parallel fibers. This can be controlled by the parameter ε . When $\varepsilon \rightarrow 0$, sphere centers of the fibers in the bundles are close to the sphere centers of the other fibers. Displacement of spheres during the force biased fiber packing result these fibers into an entwined fibers (refer Figure 3.17 (a)). When $\varepsilon \rightarrow 1$, sphere centers of the fibers in the bundles are placed away from the sphere centers of the other fibers. These fibers are displaced as parallel fibers during the force biased fiber packing (refer Figure 3.17 (b)).

A similar type of approach as Method II to model fiber bundles has been used by Gaiselmann et al. 2013. In the initial configuration of the fiber system, they do not allow fibers to overlap within the fiber bundles. In our approach, fibers are allowed to overlap within the fiber bundles. It results in fiber bundles of entwined fibers in the final system.

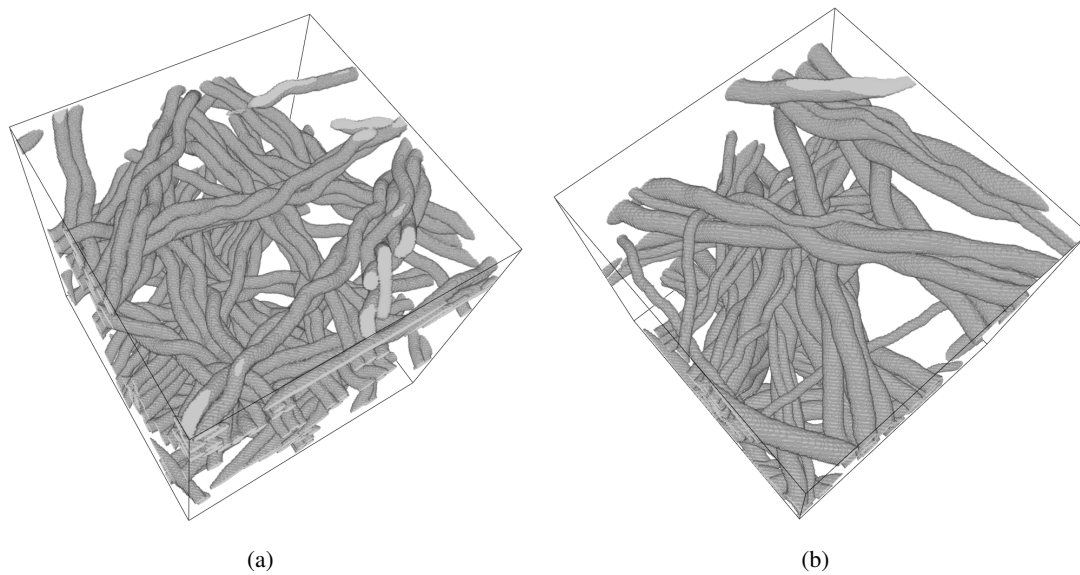


Figure 3.16 – Realizations of fiber systems with fiber bundles from Method I. (a) Fiber radius = 5 voxels and volume fraction = 12%. (b) Fiber radii = 4, and 8 voxels and volume fraction = 13%. Common parameters are window size = 250^3 voxels, $\beta = 10$, $\kappa_1 = 10$, and $\kappa_2 = 100$.

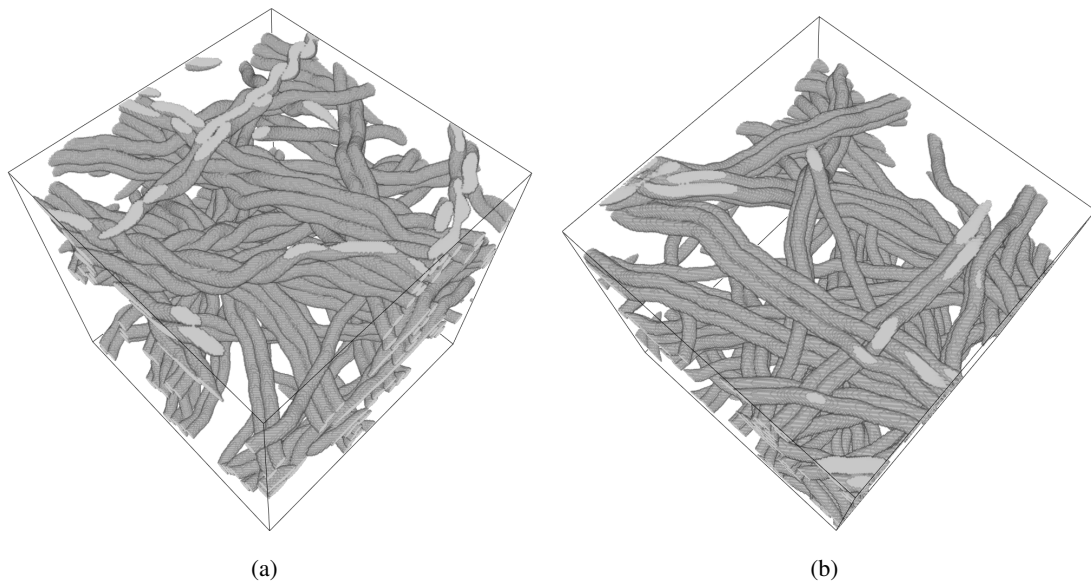


Figure 3.17 – Realizations of fiber systems with fiber bundles from Method II. (a) Entwined fibers ($\varepsilon = 0$) and volume fraction = 13%. (b) Parallel fibers ($\varepsilon = 1$) and volume fraction = 12%. Common parameters are window size = 250^3 voxels, fiber radius = 5 voxels, $\beta = 10$, $\kappa_1 = 10$, and $\kappa_2 = 100$.

4

Parameter estimation and Model fitting

In this chapter, we fit the stochastic fiber bundle model developed in Chapter 3 Section 3.3 to a specimen of nonwoven material. Recently, in Altendorf and Jeulin 2011b, the stochastic model introduced by Altendorf and Jeulin 2011a is fitted to a specimen of glass fiber reinforced polymer. They proposed methods to calculate fiber radius, anisotropy parameter β for orientation distribution, and parameters κ_1 and κ_2 for fiber bending from the three-dimensional (3D) computed tomography (CT) image. Nevertheless, fibers need to be separated beforehand in order to estimate parameters such as β , κ_1 , and κ_2 . Fiber separation for a specimen studied by Altendorf and Jeulin 2011b is achievable because the glass fiber reinforced polymers contain low levels of fiber bending and no fiber bundles. Since nonwoven materials incorporate fiber bundles and fibers with high bending, individual fiber separation is very difficult. So we cannot apply the method proposed by Altendorf and Jeulin 2011b to compute model parameters such as β , κ_1 , and κ_2 . Hence, we propose alternative approaches to compute β directly from the input image without fiber separation. In addition to that the volume fraction, media thickness, and fiber radius are also estimated from the CT image for model fitting.

In Section 4.1, we present procedures to estimate model parameters. Section 4.2 deals with the model fitting of the real nonwoven material.

4.1 Parameter estimation

4.1.1 Volume fraction

Let V be the total volume of a sample. Consider the volume of the pore phase to be V_p and the volume of the solid phase to be V_s , with $V = V_p + V_s$. The volume fraction of the solid phase is defined as $V_F = \frac{V_s}{V}$. Then, the pore volume fraction is $(1 - V_F)$ and it is commonly known as the porosity. In this thesis, we call the solid volume fraction V_F simply as the volume fraction.

The volume fraction of fiber systems is estimated using MAVI (Fraunhofer ITWM, Department of Image processing 2016) from its binarized image. It computes the volume fraction by dividing the total number of foreground voxels by the total number of voxels. Realizations of simulated fiber systems with various volume fractions are given in Figure 4.1.

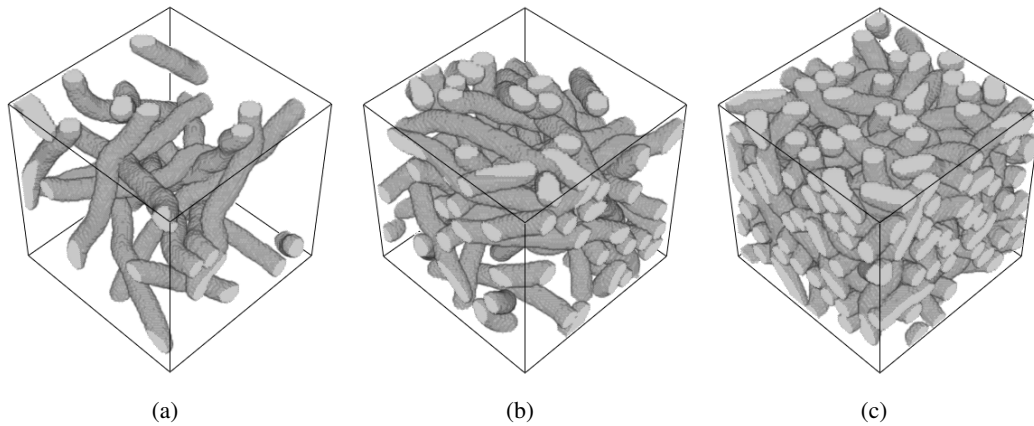


Figure 4.1 – Realizations of the fiber system with different volume fractions. Input model parameters: window size = 100^3 voxels, $\beta = 5$, fiber radius = 5 voxels, $\kappa_1 = 10$, and $\kappa_2 = 100$. (a) Volume fraction = 13%. (b) Volume fraction = 29%. (c) Volume fraction = 51%.

4.1.2 Radius estimation

The algorithm based on directional distance transform and inertia moments developed by Altendorf and Jeulin 2009 is applied to compute the fiber radius distribution. A short description of this method is given in Appendix.

4.1.3 Orientation estimation

The main fiber orientation in the modeling of fiber systems proposed in Chapter 3 follows the distribution introduced by Schladitz et al. 2006. The short description of this distribution is given in Chapter 2 Subsection 2.2.1. Since this distribution depends on an anisotropy parameter β , it has to be estimated from the input data.

Recently, a maximum-likelihood (ML) estimator for parameter β has been developed by Franke et al. 2016. We use this estimator to compute β from the given CT data. The proposed ML estimator takes independent, identically distributed (i.i.d.) data as an input. In case of fiber systems with less fiber interaction, the mean orientation of each fiber can be considered as a required i.i.d. data for the ML estimator. Estimation of the mean fiber orientation without single fiber separation is not possible. On the other hand, instead of the mean fiber orientation, local fiber orientations, which are computed on each fiber voxel can be considered. Already, Franke et al. 2016 applied the ML estimator using local fiber orientations to estimate β for specimens of glass fiber composites.

Since local fiber orientations are not a i.i.d. data, the effect of the ML estimator for non i.i.d. data has been studied. Therefore, in this section, we evaluate the ML estimator for non i.i.d. data, i.e., local fiber orientations, utilizing simulated 3D fiber systems. Computation of the ground truth for the synthetic data is explained later in this section. For the estimation of local fiber orientations, the Hessian-based approach (Wirjadi et al. 2016) and a technique based on directional distance

transform and inertia moments introduced by Altendorf and Jeulin 2009 are considered. Then, the ML estimator is applied to compute β using local orientations from these two approaches, separately. Finally, the estimated results are compared with the ground truth.

For our analysis, we generate 3D realization of fiber systems using the random sequential adsorption (RSA) cylinder model (Chapter 2 Section 2.4) and the stochastic model for endless fibers introduced in Chapter 3 Section 3.2. The following configurations are considered for our study. Set of all input values of β is denoted as $B = \{0.1, 0.4, 0.8, 1, 3, 5, 7, 9\}$.

Model I: The RSA cylinder model with fixed fiber thickness

- Model parameters: window size = 250^3 voxels, number of fibers = 100, $\beta \in B$, fiber thickness = 10 voxels, and fiber length = 300 voxels

Model II: The RSA cylinder model with variable fiber thickness I

- Model parameters: window size = 250^3 voxels, number of fibers = 100, $\beta \in B$, fiber thicknesses are uniformly distributed in the interval [3,6], and fiber length = 300 voxels

Model III: The RSA cylinder model with variable fiber thickness II

- Model parameters: window size = 250^3 voxels, number of fibers = 100, $\beta \in B$, fiber thicknesses are uniformly distributed in the interval [3,16], and fiber length = 300 voxels

Model IV: The stochastic model for endless fibers with almost straight fibers

- Model parameters: window size = 250^3 voxels, volume fraction = 10%, $\beta \in B$, fiber thickness = 10 voxels, $\kappa_1 = 200$, and $\kappa_2 = 5$

Model V: The stochastic model for endless fibers with curved fibers

- Model parameters: window size = 250^3 voxels, volume fraction = 10%, $\beta \in B$, fiber thickness = 10 voxels, $\kappa_1 = 10$, and $\kappa_2 = 100$

Fiber systems are simulated utilizing the aforementioned models for all values of $\beta \in B$. Some of the realizations produced from these models are displayed in Figures 4.2 - 4.6. Local fiber orientations of the simulated fiber systems are input for the ML estimator. They are computed using the Hessian and the inertia-based approaches. In addition to that two more inputs "orientation type" and "initial β " are required for numerical evaluation based on Newton's method. Parameter "orientation type" should be either girdle or bipolar. Parameter "initial β " is the initial value β_0 for Newton's method. Input values for "orientation type" and "initial β " which are used for our computations are given in Table 4.1. Even though we realize that β around 1 is neither "bipolar" nor "girdle" type, we choose type "bipolar" for $\beta \leq 1$ and "girdle" for $\beta > 1$. Because the method has only these two choices.

input β	orientation type	initial β
0.1	bipolar	0.05
0.4	bipolar	0.05
0.8	bipolar	0.05
1	bipolar	0.05
3	girdle	0.05
5	girdle	0.05
7	girdle	0.05
9	girdle	0.05

Table 4.1 – Input parameters for the ML estimator considered in our experiments

Ground truth

We compute the ground truth for parameter β as in the following:

The RSA fiber system: Fibers are modeled as straight cylinders. The mean orientation of each cylinder is extracted during fiber generation. Then, the ML estimator is applied for these i.i.d. data to estimate the ground truth.

The stochastic model for endless fibers: Here, we denote the simulated fiber system as $P = \{p_{1,1}, p_{1,2}, \dots, p_{1,l_1}, p_{2,1}, \dots, p_{N,l_N}\}$ where $p_{j,i} = (x_{j,i}, \mu_{j,i}, r_{j,i}) \in \mathbb{R} \times S^2 \times \mathbb{R}_{>0}$, N be number of fibers, l_j is the total number of spheres in the j -th fiber. The mean orientation of the j -th fiber is defined as $\bar{\mu}(P_j) = \frac{p_{j,l_j} - p_{j,1}}{|p_{j,l_j} - p_{j,1}|} \in S^2$. Since these calculated orientations are i.i.d. data, we consider $\hat{\beta}$ estimated using the ML estimator from these data as the ground truth.

Results

The mean of the estimated β from 100 realizations for Model I - V are computed. The deviation of the mean value from the input β for Model I - V are plotted in Figures 4.7 - 4.11, respectively. Since all fibers in the realizations of the RSA model are completely straight, the deviation of ground truth is 0.27 (see Figures 4.7 - 4.9). However, already for slightly bend fibers, the deviation is 0.87 (Figure 4.10). The deviation is 2.69 for strongly curved fibers (Figure 4.11).

Since the local fiber orientation estimation around the fiber surfaces contains noise, β is also computed for data without surface voxels. The ML estimator for data after removing surface voxels gives better values for β in all five models (see Figures 4.7 - 4.11). Moreover, the difference between β estimated with and without surface voxels in Figures 4.7, 4.10, and 4.11 shows that the Hessian-based technique has more surface noise than the one based on inertia.

For Model I, the ML estimator based on inertia approach without surface voxels estimates β for input $\beta \leq 7$ with maximum deviation of 0.5. The same experiment is repeated to check the estimate

for fiber systems with different thicknesses (Model II and Model III). Since our generated realizations contain various fiber thicknesses, an appropriate scale σ has to be chosen for the Hessian method. We choose σ for Model II and Model III as 1.5, 2.25, and 3, and 1.5, 3, and 8, respectively. Here also, once input for β gets larger, the ML estimator starts to underestimate β . Figures 4.8 and 4.9 show that the choice of scale influences the computation of β . The Hessian-based technique without surface voxels for Model II does not indicate considerable variation for different scales because fiber thicknesses for this model are in a small interval [3,6]. However, for a large interval [3,16] in Model III, we observe significant changes in the estimated value of β for various scales. The appropriate selection of scale may give better results for the Hessian method.

Realizations created from Model IV contain slightly curved fibers. The effect of these small curves is reflected in the β estimation (see Figure 4.10), i.e. the deviation for input $\beta > 3$ is larger than 0.5. Since realizations of Model V include strong fiber bending, we observe more deviation in both estimates (see Figure 4.11). Especially, calculated values of β get worse for larger β , i.e., $\beta > 3$.

Despite the fact that the Hessian-based approach and the technique depending on inertia yield almost the same result after removing surface voxels, we use the inertia-based method for model fitting in the next section. The reason for this choice is that the approach based on inertia is independent of scale.

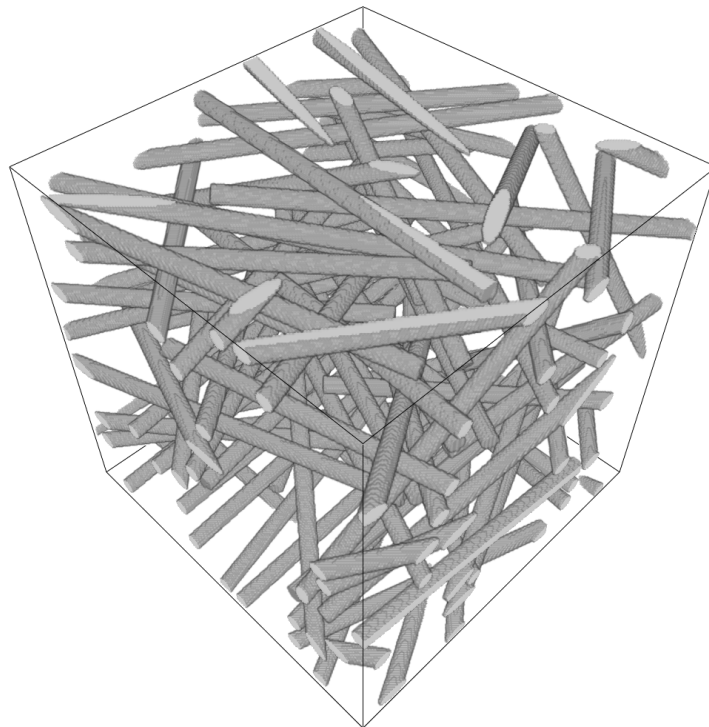


Figure 4.2 – A realization of Model I. Model parameters: window size = 250^3 voxels, number of fibers = 100, $\beta = 5$, fiber thickness = 10 voxels, and fiber length = 300 voxels.

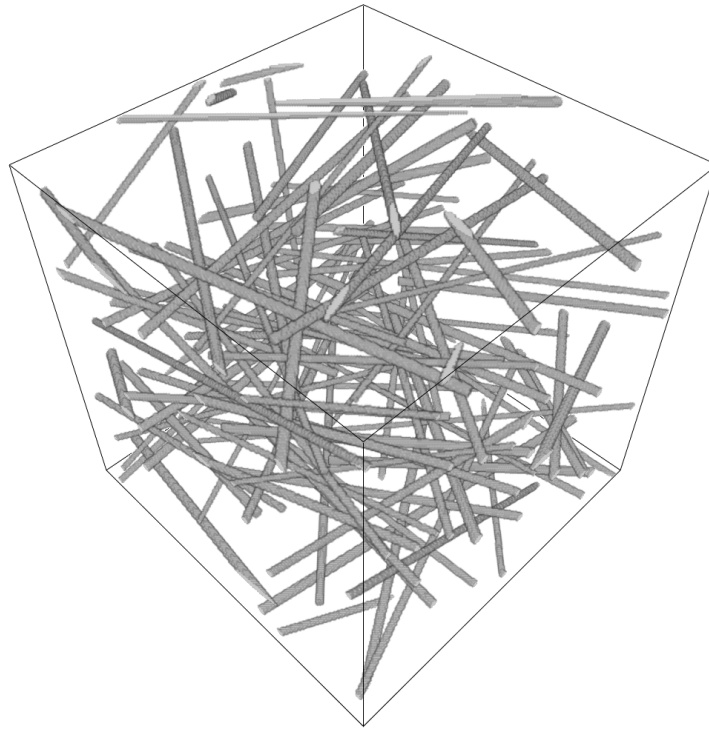


Figure 4.3 – A realization of Model II. window size = 250^3 voxels, number of fibers = 100, $\beta = 5$, fiber thicknesses are uniformly distributed in the interval $[3,6]$, and fiber length = 300 voxels.

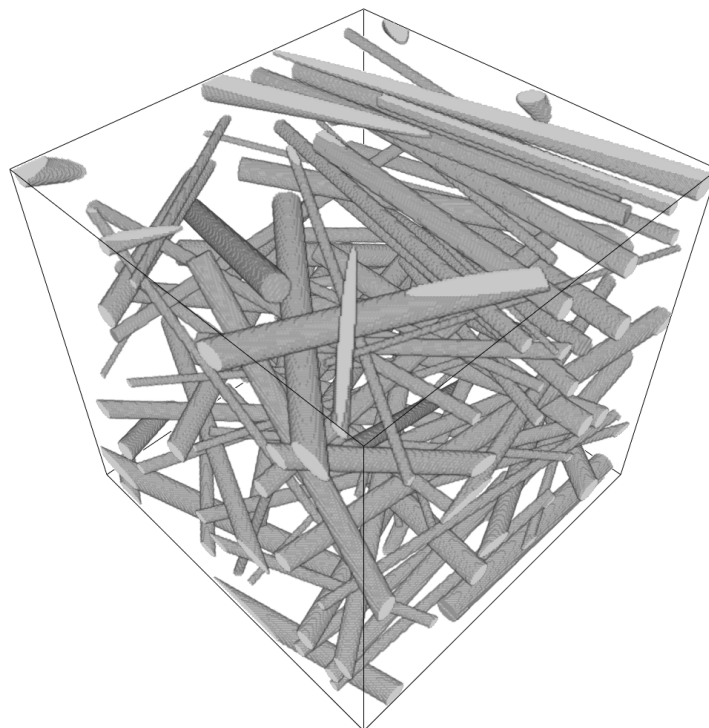


Figure 4.4 – A realization of Model III. Model parameters: window size = 250^3 voxels, number of fibers = 100, $\beta = 5$, fiber thicknesses are uniformly distributed in the interval $[3,16]$, and fiber length = 300 voxels.

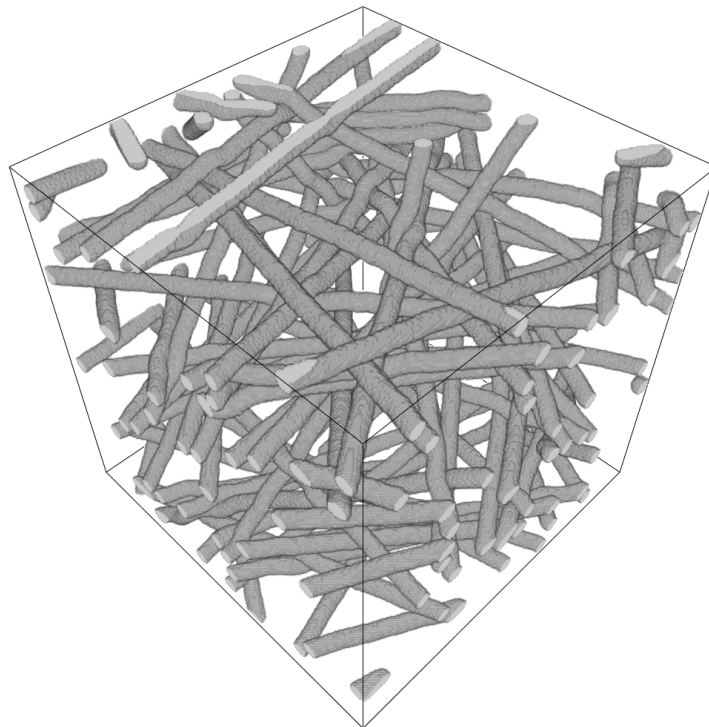


Figure 4.5 – A realization of Model IV. Model parameters: window size = 250^3 voxels, volume fraction = 10%, $\beta = 5$, fiber thickness = 10 voxels, $\kappa_1 = 200$, and $\kappa_2 = 5$.

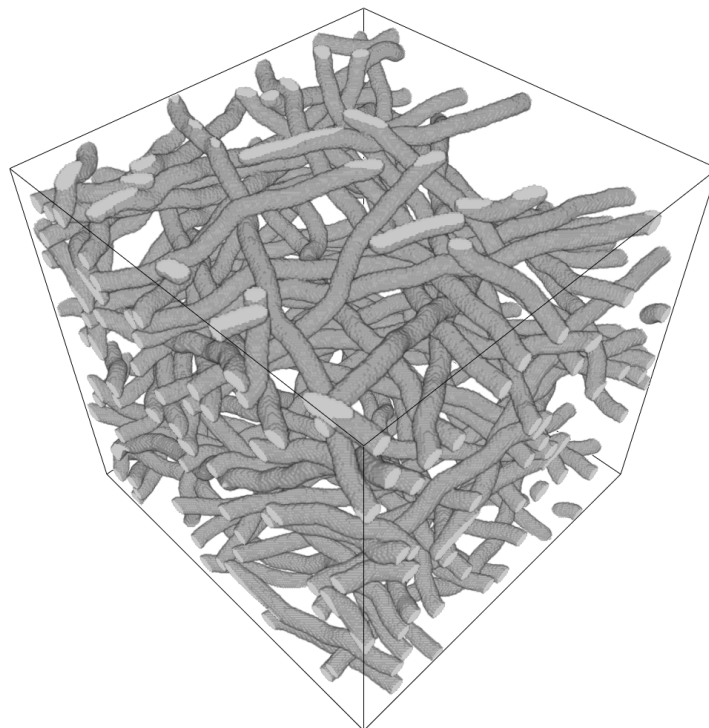


Figure 4.6 – A realization of Model V. window size = 250^3 voxels, volume fraction = 10%, $\beta = 5$, fiber thickness = 10 voxels, $\kappa_1 = 10$, and $\kappa_2 = 100$.

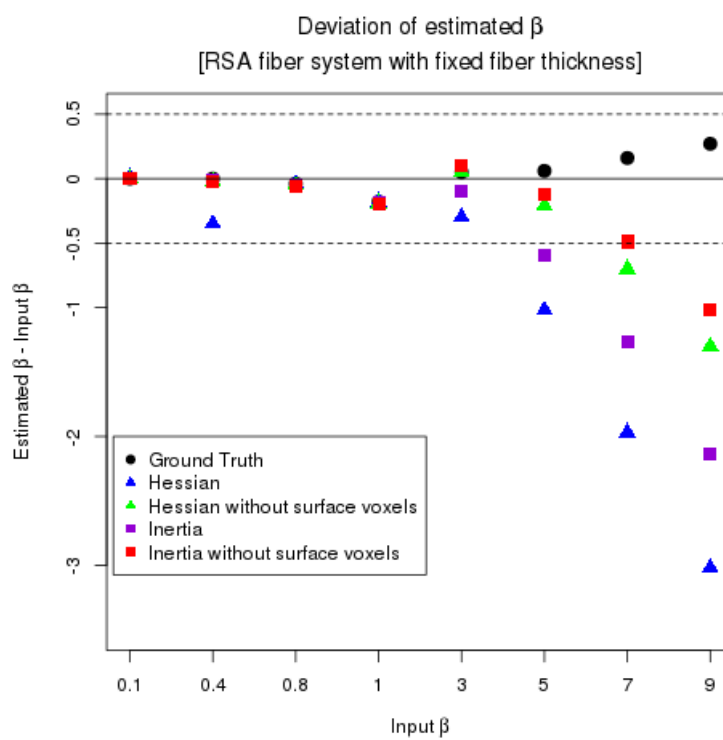


Figure 4.7 – Deviation of the mean of the estimated β for Model I.

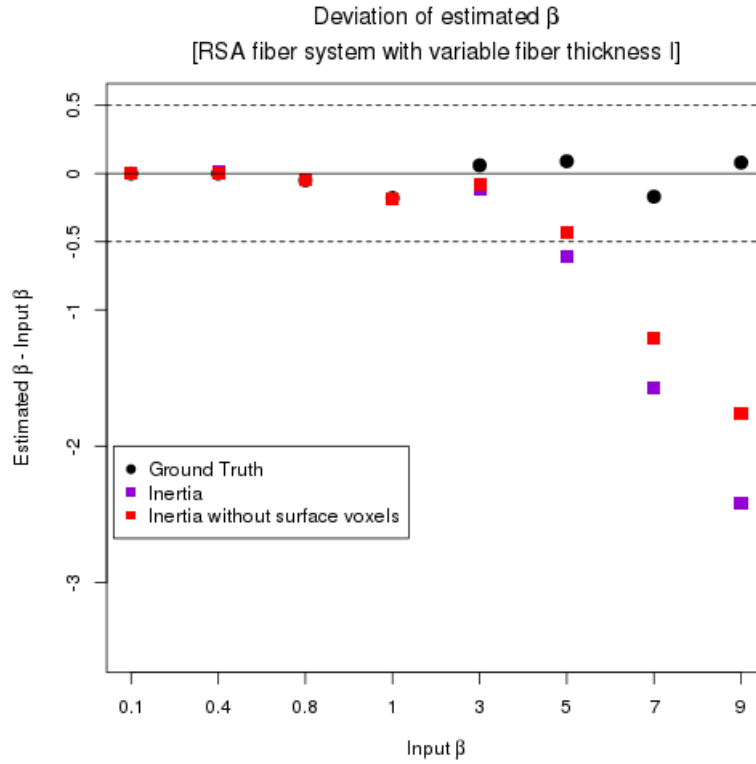
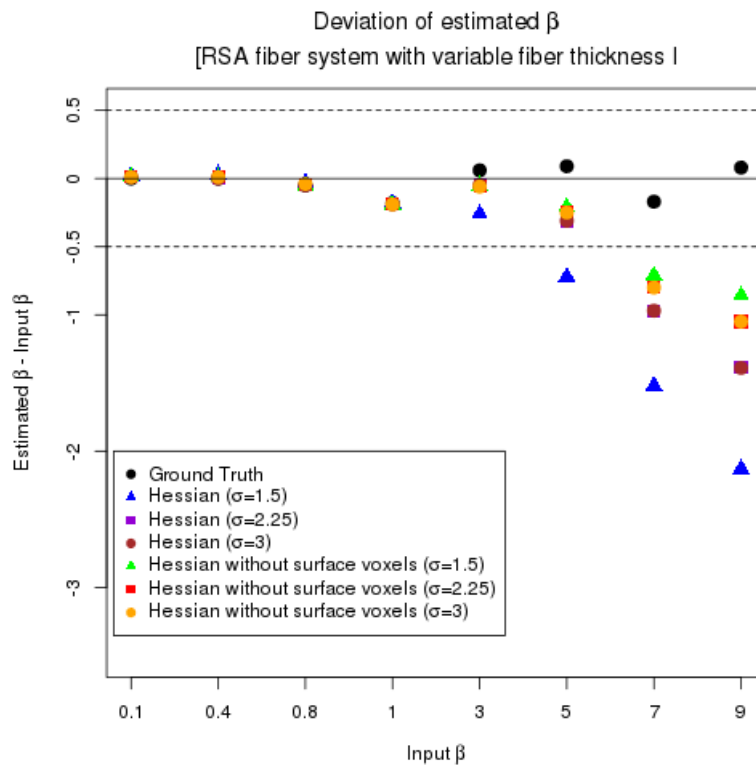


Figure 4.8 – Deviation of the mean of the estimated β for Model II. (a) Hessian. (b) Inertia method.

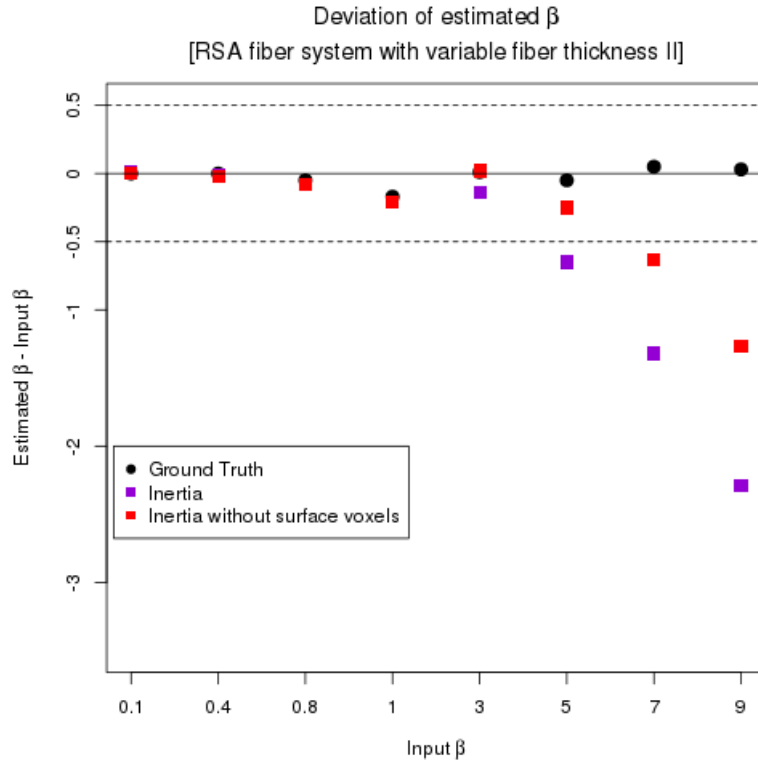
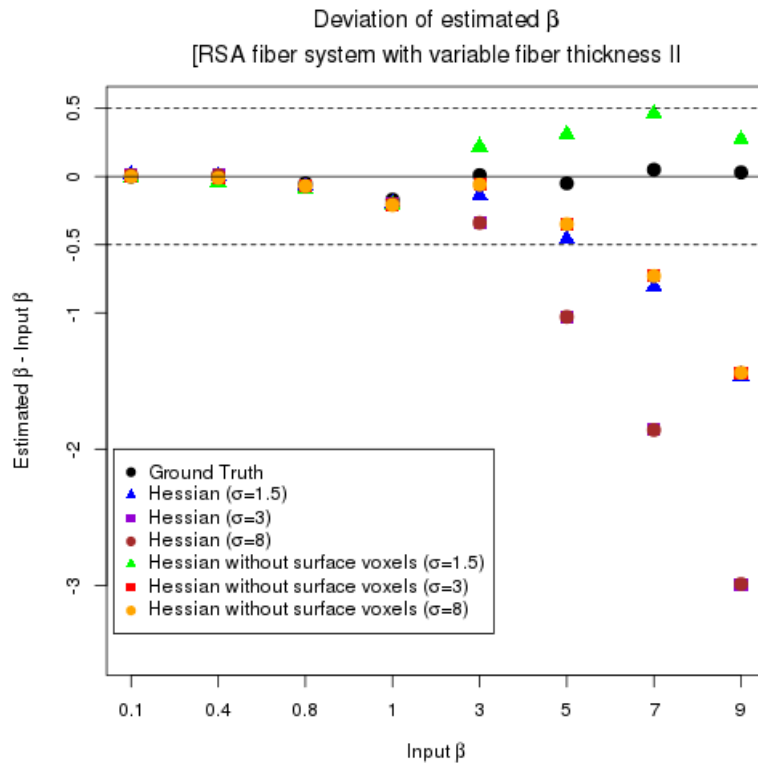


Figure 4.9 – Deviation of the mean of the estimated β for Model III. (a) Plot for the Hessian approach. (b) Plot for the inertia method.

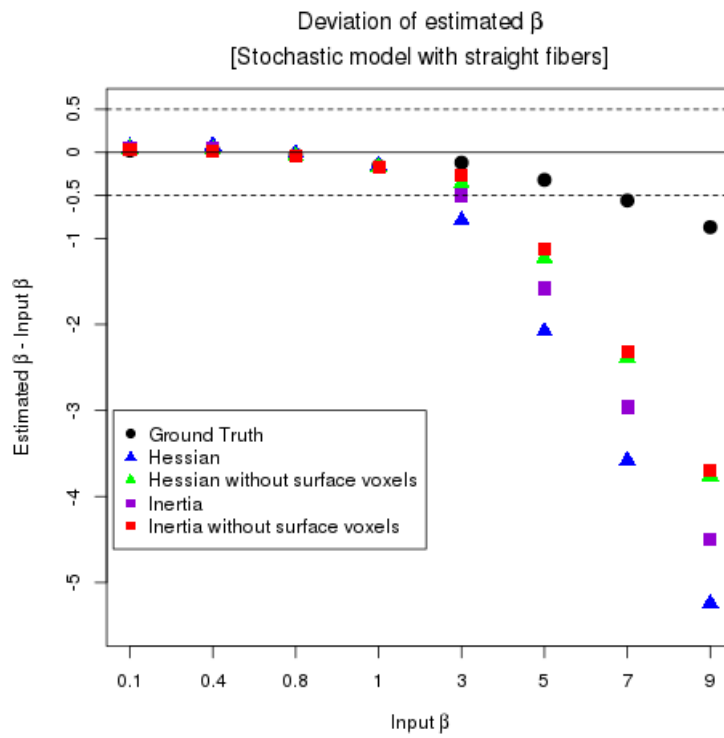


Figure 4.10 – Deviation of the mean of the estimated β for Model IV.

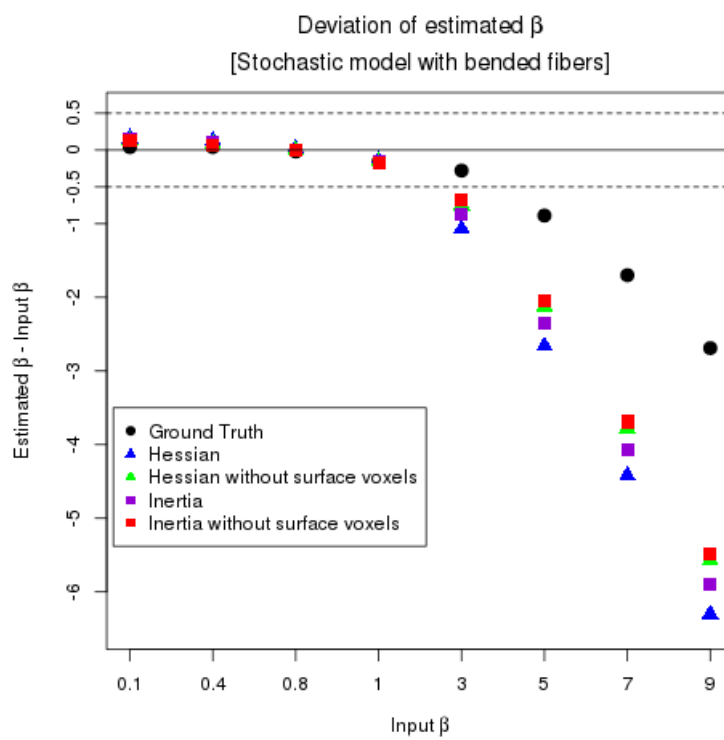


Figure 4.11 – Deviation of the mean of the estimated β for Model V.

4.2 Model fitting

The CT image of the non-woven material considered for model fitting is shown in Figure 4.12 (a). Size of the image is $580 \times 580 \times 300$ voxels with a voxel edge length of $1.87 \mu\text{m}$. The median filter (Equation (2.6.1)) with a window size 5 is used to remove background noise from the data. Then, the filtered image is segmented using the global thresholding approach (Otsu 1979). This segmentation step assigns gray value "0" for background and "1" for foreground. The segmented image is given in Figure 4.12 (b).

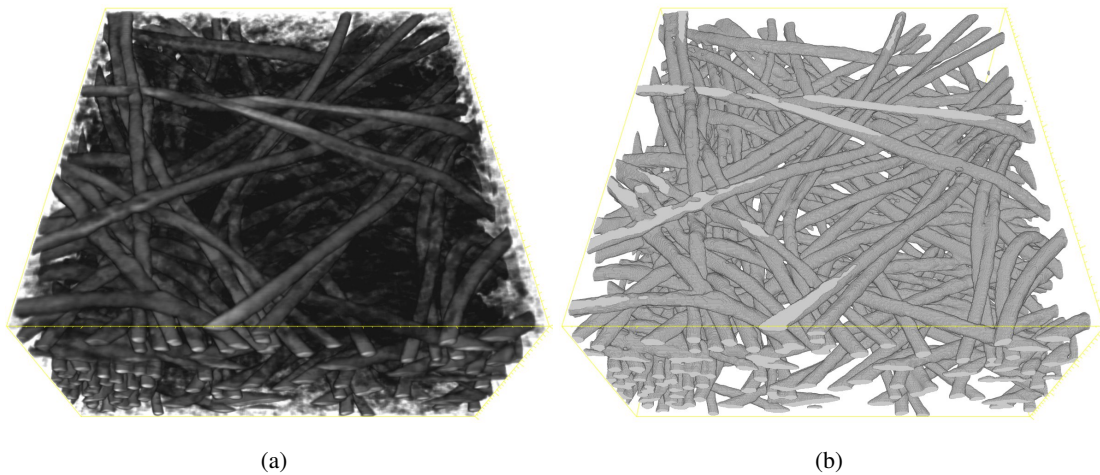


Figure 4.12 – (a) A 3D visualization of the CT image of the non-woven material. Size: $580 \times 580 \times 300$ voxels and voxel edge length: $1.87 \mu\text{m}$. (b) The segmented image of (a)

We observe that fibers in the specimen have circular cross section and it contains single fibers and fiber bundles. Therefore, the stochastic model for fiber systems introduced in Chapter 3 Section 3.3 is fitted to the given CT data. Since fiber bundles contain parallel fibers not entwined fibers, we consider Method II for fiber bundles with $\varepsilon = 1$. The virtual microstructure realizations will be evaluated by comparing the pressure drop, which is a macroscopic property of the filter media, of the real material and the simulated microstructure realizations. The pressure drop is computed using the FlowDict module of the GeoDict2017 software (Math2Market, Kaiserslautern, Germany). Details of the pressure drop simulation implemented in this software is given in Wiegmann et al. 2010. The estimated pressure drop for the given real non-woven material is 8.05527 Pa .

Following parameters are estimated from the segmented image using the methods described in the previous section. The volume density is 15.77% and the fiber radius is 7.96 voxels. The β value for the Schladitz distribution is estimated using the approach described in Subsection 4.1.3. Precisely, we use the ML estimator based on inertia approach without surface voxels. The estimated β value is 4.37 . Since the real data contains slightly curved fibers, based on our results from Subsection 4.1.3, the β value may be underestimated. Since we do not have exact method to correct this bias, estimated β is used for model fitting.

There is also no method available in the literature to estimate κ_1 and κ_2 from the data without separating the fibers. We observe from the data that fibers are neither straight nor locally curved. Based on the properties of κ_1 and κ_2 , and the observations from the virtual microstructure realizations, if $(\kappa_1, \kappa_2) = (5, 10)$, fibers are more locally curved and if $(\kappa_1, \kappa_2) = (50, 200)$, fibers are straight. By taking this into account, we choose six different combinations of κ_1 and κ_2 for our realizations such as $(5, 100)$, $(5, 200)$, $(10, 100)$, $(20, 200)$, $(30, 200)$, and $(50, 200)$. Also there is no proper method to estimate number of fiber bundles from our data. Bundles put fibers close together, intuitively, it creates empty space in the microstructure. This will influence the pressure drop of the microstructure realization. We visually observe from the data that the maximum number of fibers in a bundle is two. Here we consider three different set of realizations, one without fiber bundles (say Model A), second with 20% of its fibers are bundles (say Model B), and third with 60% of its fibers are bundles (say Model C).

Five realizations for each combination of (κ_1, κ_2) are generated for each model. The pressure drop computed for each realizations is plotted for Model A in Figure 4.13 (a), for Model B in Figure 4.14 (a), and for Model C in Figure 4.15 (a). The mean and standard deviations of the pressure drop are plotted in Figure 4.13 (b), Figure 4.14 (b), and Figure 4.15 (b).

As we expected, Figures 4.13-4.15 shows that if the number of fiber bundles in the system increases, the pressure drop decreases. Also, it turns out that, the pressure drop of the realizations generated from Model B is same as the real material with relative error less than 8% for three combinations of κ_1 and κ_2 such as $(5, 100)$, $(20, 200)$, and $(30, 200)$. Realizations simulated from Model B are illustrated in Figure 4.16. From the description of our fiber model we know that, for smaller κ_1 values, fibers have more bending and for larger κ_1 values, fibers are straight. Since fibers in the given CT data are neither locally curved nor completely straight (visual observation), we select realizations with $\kappa_1 = 20$ and $\kappa_2 = 200$ as the fitted model for the CT data.

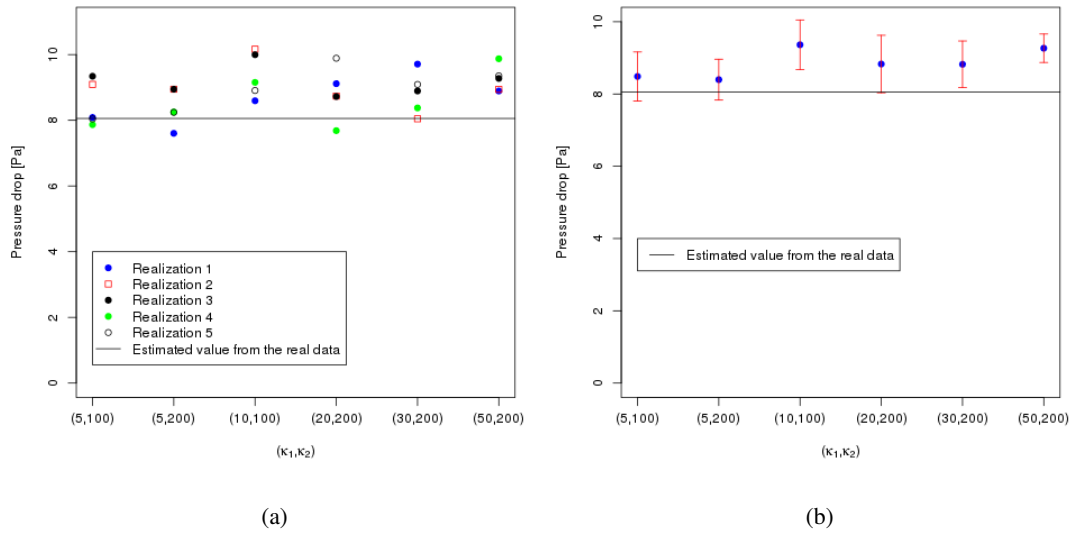


Figure 4.13 – The mean and standard deviation of pressure drop computed over 5 realizations for each combination of κ_1 and κ_2 . These realizations are without fiber bundles (Model A).

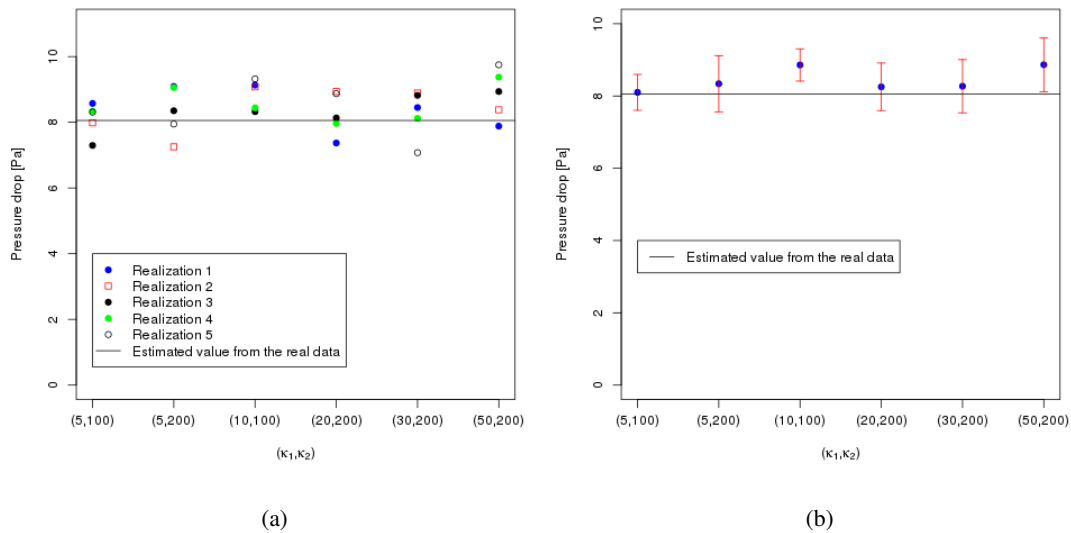


Figure 4.14 – The mean and standard deviation of pressure drop computed over 5 realizations for each combination of κ_1 and κ_2 . 20% of the fibers in these realizations form bundles of two fibers (Model B).

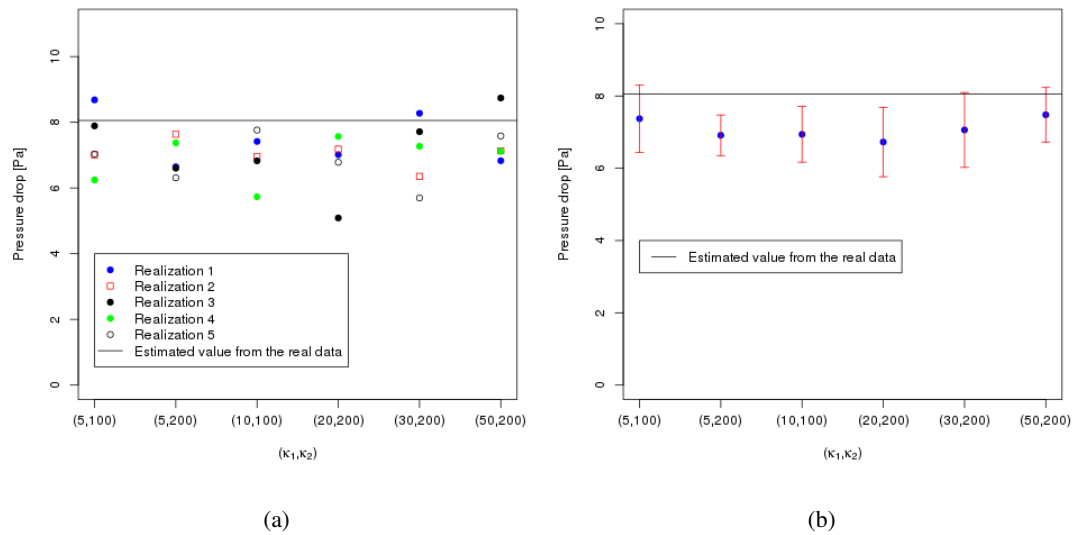


Figure 4.15 – The mean and standard deviation of pressure drop computed over 5 realizations for each combination of κ_1 and κ_2 . 60% of the fibers in these realizations form bundles of two fibers (Model C).

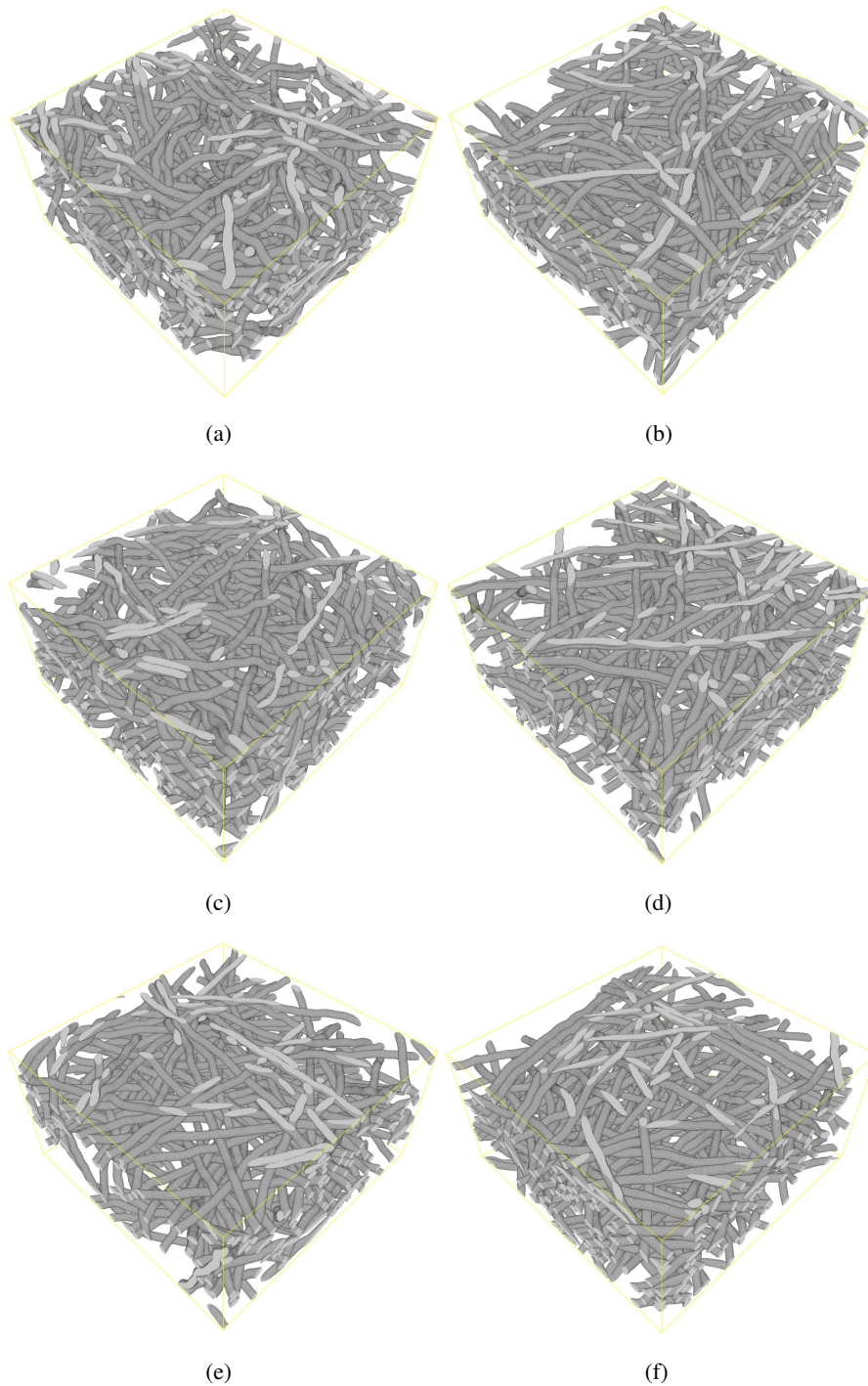


Figure 4.16 – A 3D visualization of generated fiber system. Common parameters: Window size = $580 \times 580 \times 300$ voxels, fiber radius = 7.96 voxels, $\beta = 4.37$. (a) $\kappa_1 = 5$ and $\kappa_2 = 100$. (b) $\kappa_1 = 5$ and $\kappa_2 = 200$. (c) $\kappa_1 = 10$ and $\kappa_2 = 100$. (d) $\kappa_1 = 20$ and $\kappa_2 = 200$. (e) $\kappa_1 = 30$ and $\kappa_2 = 200$. (f) $\kappa_1 = 50$ and $\kappa_2 = 200$.

5

Representative domain size for simulated three-dimensional fiber systems

In this chapter, we estimate the representative domain size or size of the representative volume element (RVE) for virtual microstructures generated from the fiber bundle model developed in Chapter 3. Parts of this chapter were published in Easwaran et al. 2016b. Previously, a purely simulation based domain size study for the non-overlapping fiber systems simulated by the GeoDict2014 software (Math2Market, Kaiserslautern, Germany) was carried out by Lehmann et al. 2016. A statistical approach to compute the size of the RVE for a given property is proposed by Kanit et al. 2003. In the literature, this approach has been used to calculate the size of the RVE for various microstructure models and materials properties such as elasticity or thermal conductivity (see Kanit et al. 2006; Altendorf 2011c; Dirrenberger et al. 2014).

Here, we use both a simulation and the statistical approach to compute the size of the RVE. In particular, the representative domain size is estimated for the packing density, the pore size distribution which are geometric characteristics of the microstructure and the pressure drop which is a macroscopic property of the resulting filter media. The statistical approach from Kanit et al. 2003 is used to compute the representative domain size for the packing density and the pressure drop. Finally, the simulation results are compared with the statistical results. It turns out that the statistical approach can be used to estimate the representative domain size for the given property more precisely and using less generated microstructures than the purely simulation based approach.

Section 5.1 deals with the generation of realizations for the domain size study. The estimation of the representative domain size based on the simulation approach and the statistical approach is given in Section 5.2 and 5.3, respectively. The results are discussed in Section 5.4.

5.1 Microstructure generation for domain size study

We generate the microstructure realizations for this study using our fiber bundle model (Method I) introduced in Chapter 3 Section 3.3. Due to the stochasticity of our model, each model simulation run with fixed input parameters generates a different realization of the geometric structure. For our domain size study, we consider 10 independent realizations of the model for five different domain sizes $2000^2 \times 512$ voxels, $1000^2 \times 512$ voxels, $750^2 \times 512$ voxels, $500^2 \times 512$ voxels,

and $250^2 \times 512$ voxels as in Figure 5.1. Totally, we have 50 realizations. The input parameters are fixed for all realizations as in the following. Fiber radius = 5 voxels, $\beta = 10$, $\kappa_1 = 10$ and $\kappa_2 = 100$. In these realizations, 40% of the given fibers form bundles of four fibers, 30% of fibers form bundles of three fibers, 20% of fibers are paired and the remaining fibers are modeled as individual fibers. During the microstructure generation, all sides of the given window are enlarged by 100 voxels.

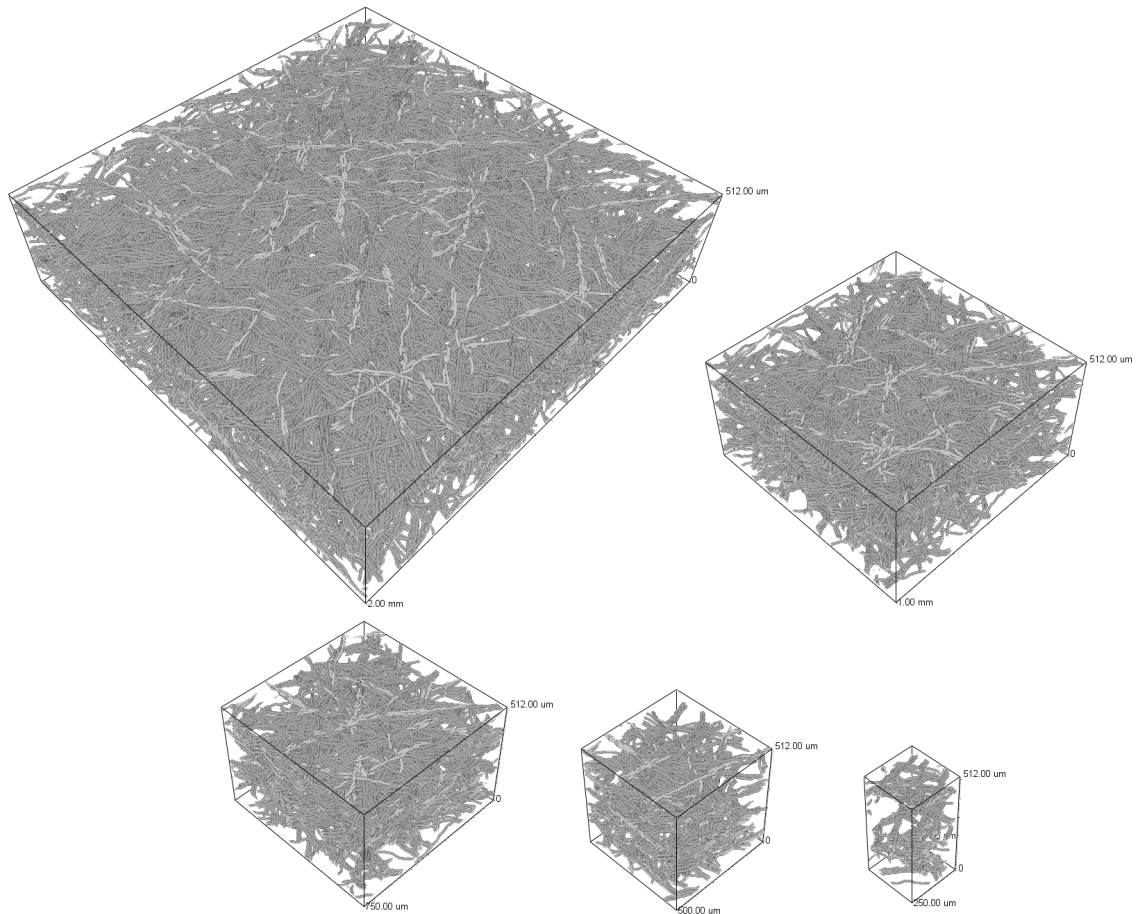


Figure 5.1 – Realizations of our stochastic geometry model in different domain sizes $2000^2 \times 512$ voxels, $1000^2 \times 512$ voxels, $750^2 \times 512$ voxels, $500^2 \times 512$ voxels, and $250^2 \times 512$ voxels. Volume fraction $\approx 10\%$, fiber radius = 10 voxels and fibers are oriented in the xy -plane.

5.2 Simulation study regarding domain size

In this section, we compute the representative domain size for the packing density, the pressure drop, and the pore size distribution. To this end, the three characteristics are calculated for the 10 realizations of each domain size using the GeoDict2017 software (Math2Market, Kaiserslautern, Germany). The pore size distribution is calculated using the PoroDict module of the software. A pore diameter is computed by fitting spheres into the pore volume i.e., granulometry on the pore space. The pressure drops are computed using the FlowDict module of the software. The mean and standard deviation are computed for all domains. Results are plotted in Figures 5.2.

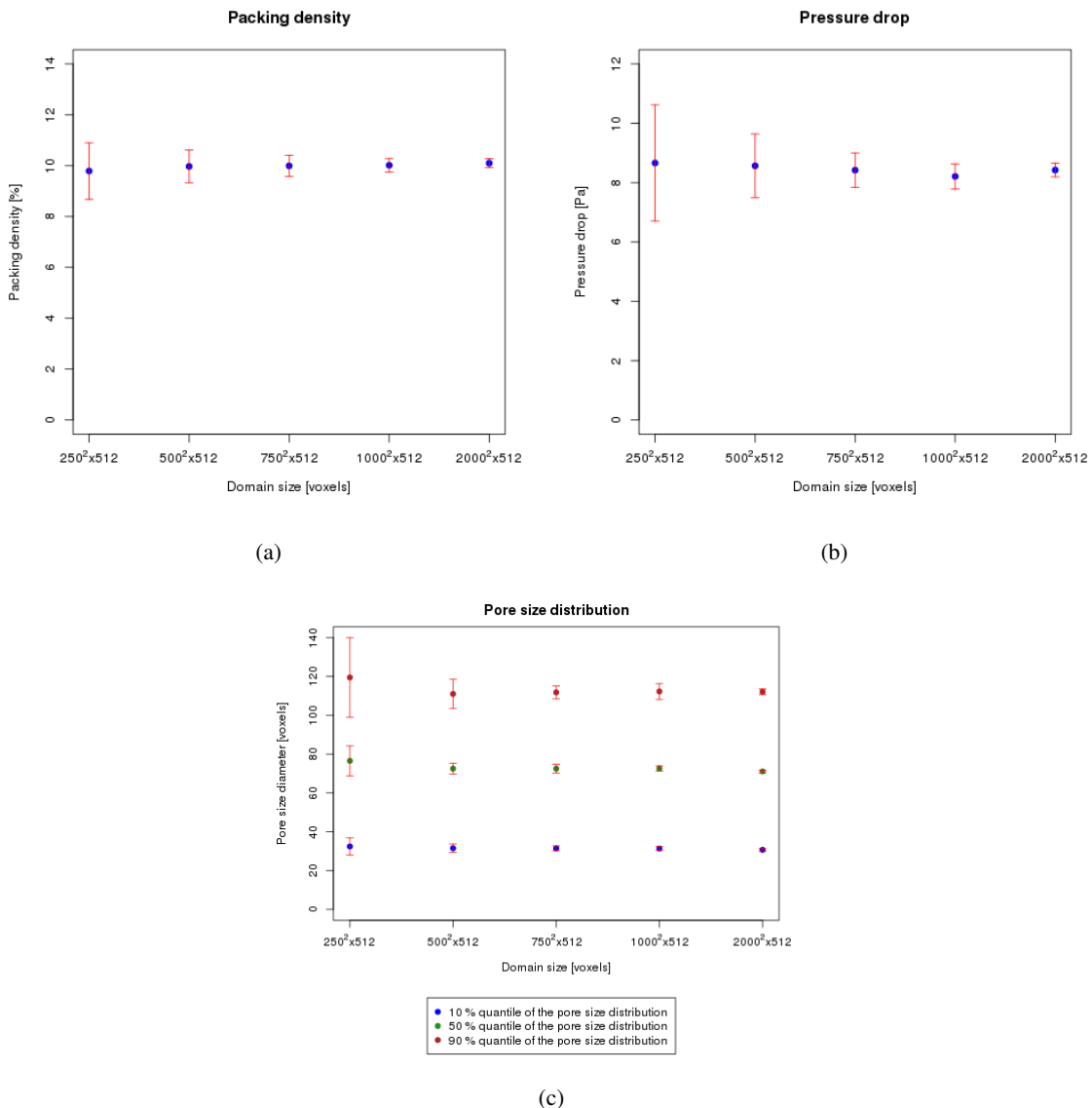


Figure 5.2 – The mean and standard deviation (error bar) of the packing density (a), the pressure drop (b), and the pore size distribution (c) computed for 10 realizations of each domain size.

5.3 Statistical study regarding domain size

The statistical approach to estimate the size of the RVE for a given property Z , for a given relative precision in the estimation of Z , and given number of realizations that one is ready to simulate is defined by Kanit et al. 2003.

We summarize this approach in the following. Let \bar{Z} be the mean of the given property Z estimated on m independent realizations of domain V_v of volume v . The sub-domains $V_{s,1}, V_{s,2}, \dots, V_{s,m}$ of equal volume $s < v$ are cropped from m independent realizations. The mean squared error of the given property Z in m sub-domains of equal volume s to the target property \bar{Z} is defined as

$$D_Z^2(V) = \frac{1}{m} \sum_{i=1}^m (Z_i - \bar{Z})^2 \quad (5.1)$$

where Z_i is the calculated value of the given property Z on sub-domain $V_{s,i}$.

For an ergodic stationary random function $Z(x)$, the mean squared error $D_Z^2(V)$ of its mean value \bar{Z} over the volume V is defined as (Kanit et al. 2003)

$$D_Z^2(V) = D_Z^2 \frac{A_3}{V} \quad (5.2)$$

where D_Z^2 is the point variance of $Z(x)$ and A_3 is so-called the integral range. The integral range provides information on the domain size of the structure for which the parameters measured in this volume have a proper statistical representativity.

Since the integral range of the typical microstructures with long range of correlations like dilated Poisson lines in 3D is not finite (Jeulin 1991a and Jeulin 1991b), the computation of $D_Z^2(V)$ in Equation (5.2) cannot be used (Jeulin 2011). The scaling law with exponent $\alpha < 1$ was proposed by Lantuéjoul 1991. The variance in Equation (5.2) can be rewritten as (Jeulin 2011)

$$D_Z^2(V) = D_Z^2 \frac{\tilde{A}_3^\alpha}{V^\alpha}$$

where \tilde{A} is not anymore an integral range, however, still it is homogeneous to a microstructure volume (Jeulin 2011).

For the microstructure with infinite integral range, there is no information about the theoretical value of the point variance D_Z^2 except geometric characteristics (Dirrenberger et al. 2014). The above equation was reformulated by Dirrenberger et al. 2014 as

$$D_Z^2(V) = \frac{K}{V^\alpha} \quad (5.3)$$

where $K = D_Z^2 \tilde{A}_3^\alpha$.

The variables K and α can be numerically approximated by fitting a straight line to the logarithmic version of Equation (5.3):

$$\log D_Z^2(V) = \log K - \alpha \log V \quad (5.4)$$

The absolute error ϵ_{abs} on the mean value of the given property obtained with n independent realizations of volume V is deduced from the interval of confidence (95 %) by

$$\epsilon_{abs} = \frac{2D_Z(V)}{\sqrt{n}}$$

The relative error ϵ_{rel} is given as

$$\epsilon_{rel} = \frac{\epsilon_{abs}}{\bar{Z}} \quad (5.5)$$

$$\epsilon_{rel}^2 = \frac{4D_Z^2(V)}{n\bar{Z}^2} \quad (5.6)$$

Substitute Equation (5.3) in Equation (5.6),

$$\epsilon_{rel}^2 = \frac{4K}{n\bar{Z}^2 V^\alpha} \quad (5.7)$$

The size of the RVE for effective property Z with a given relative error ϵ_{rel} and n realizations is defined as

$$V_{RVE} = \left(\frac{4K}{\epsilon_{rel}^2 n \bar{Z}^2} \right)^{\frac{1}{\alpha}} \quad (5.8)$$

We apply the above mentioned statistical approach to estimate the size of the RVE of our generated microstructure for the packing density and the pressure drop. Samples of 10 different sub-domains with cross sections 1800^2 voxels, 1600^2 voxels, 1400^2 voxels, 1200^2 voxels, 1000^2 voxels, 800^2 voxels, 600^2 voxels, 400^2 voxels, 300^2 voxels and 200^2 voxels are cropped from 10 independent realizations of domain size $2000^2 \times 512$ voxels. The thickness of all realizations is 512 voxels.

The target packing density and pressure drop are assumed as the mean of the corresponding properties measured on 10 independent realizations of largest domain size $2000^2 \times 512$ voxels. Here, the target packing density is 10.1 % and the target pressure drop is 8.42 Pa. In order to compute the size of the RVE from Equation (5.8), the constants α and K need to be calculated. These values can be estimated by fitting a straight line to the logarithmic version of the mean squared error curve (see Equation (5.4)). The squared deviation from the target packing density is computed for all domains as in Equation (5.1). The logarithmic plot of the mean squared error and a fitted straight line are given in Figure 5.3. The values of α and K are also displayed in this figure. Similarly, the mean squared error for the pressure drop is measured and corresponding straight line fitting is given in Figure 5.4.

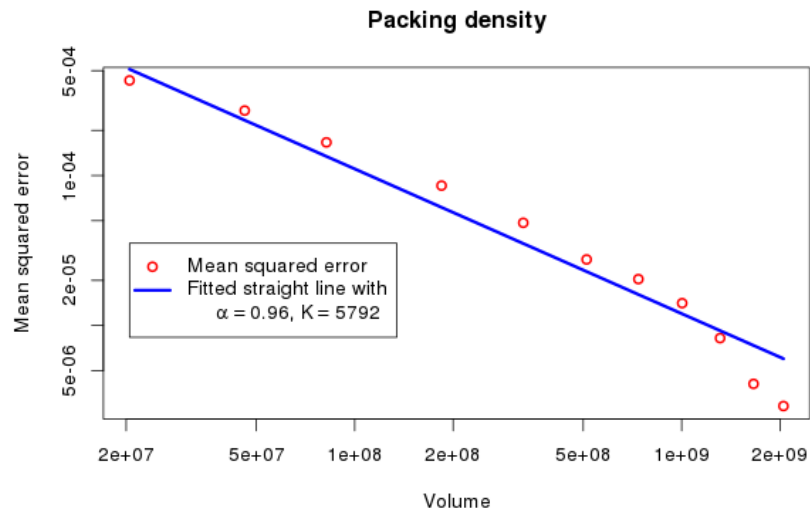


Figure 5.3 – Fitted straight line for the mean squared error of the packing density.

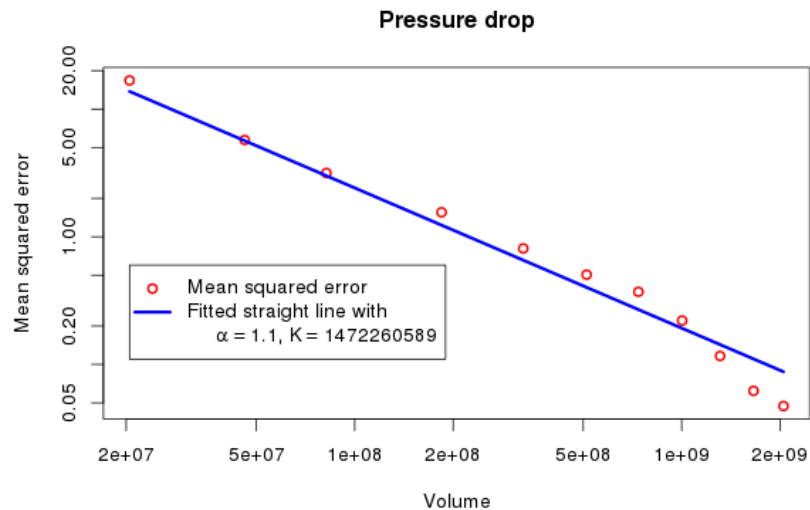


Figure 5.4 – Fitted straight line for the mean squared error of the pressure drop.

5.4 Results

From Equation (5.8), the size of the RVE for the target packing density 10.1% with relative error 5% and 10 realizations is $588^2 \times 512$ voxels. In other words, a packing density of 10.1% from our microstructure model can be achieved with a relative error of 5% by taking the mean over 10 realizations of medium domain size $588^2 \times 512$ voxels. Whereas, if we reduce the number of realizations to 1, we need a larger domain size of $1939^2 \times 512$ voxels to attain the targeted packing density 10.1% with relative error 5%.

Similarly, the representative domain size for the target pressure drop $8.42 Pa$ with relative error 5% and 10 realizations is $955^2 \times 512$ voxels. Whereas, for a single realization, the representative domain size for the target pressure drop $8.42 Pa$ with relative error 5% is $2725^2 \times 512$ voxels.

For the same target packing density 10.1% and the pressure drop $8.42 Pa$, the relative error computed using Equation (5.5) based on simulation results from Section 5.2 are plotted in Figure 5.5. It shows that if we consider 10 realizations, the representative domain size for the target packing density with relative error less than 5% is $500^2 \times 512$ voxels, and for the target pressure drop with relative error less than 5% is $750^2 \times 512$ voxels.

Both the simulation and the statistical domain size study yielded similar results. Since the statistical domain size study is carried out in cropped sub-samples of larger domains, this approach requires less computational resources than the simulation approach. In this thesis, we generated 50 realizations for the simulation study, whereas only 10 generated microstructures are needed for the statistical study. Moreover, the statistical study estimated the precise representative domain size.

Furthermore, we estimate the representative domain size for the pore size distribution using simulation results from Section 5.2. Here, we consider the mean of the pore size distribution from 10 realizations of domain size $2000^2 \times 512$ voxels as the target value. The target characteristics are 10% of all pores should have diameter smaller than 30.69 voxels, 50% of all pores should have diameter smaller than 71.09 voxels, and 90% of all pores should have diameter smaller than 112.13 voxels, respectively. The relative errors computed for the pore size distribution is plotted in Figure 5.6. It shows that if we consider 10 realizations, the pore size distribution with relative error 5% are $500^2 \times 512$ voxels.

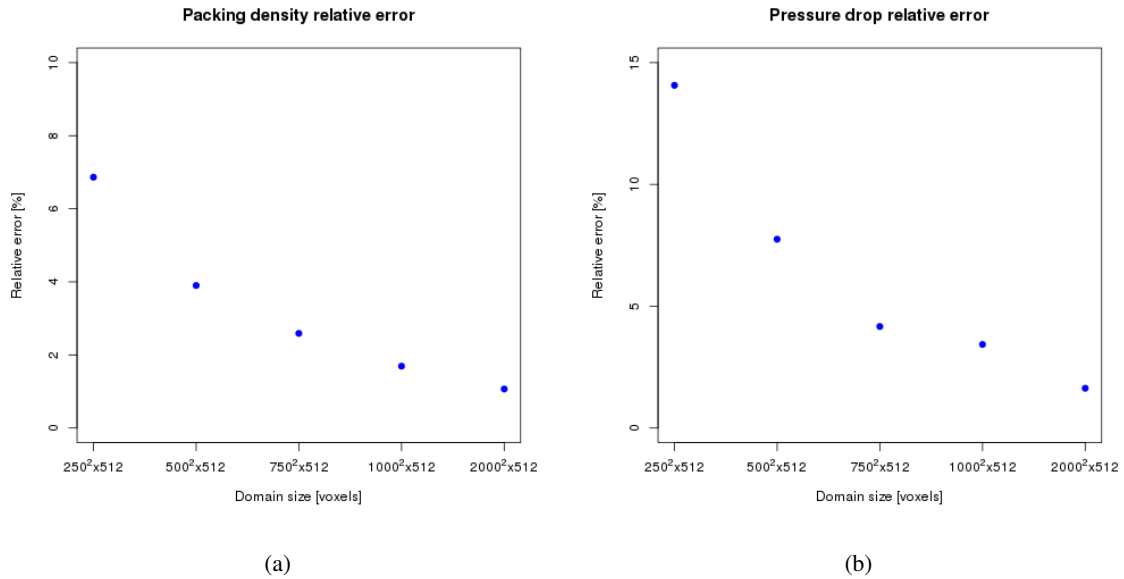


Figure 5.5 – Relative error of the packing density (a) and the pressure drop (b)

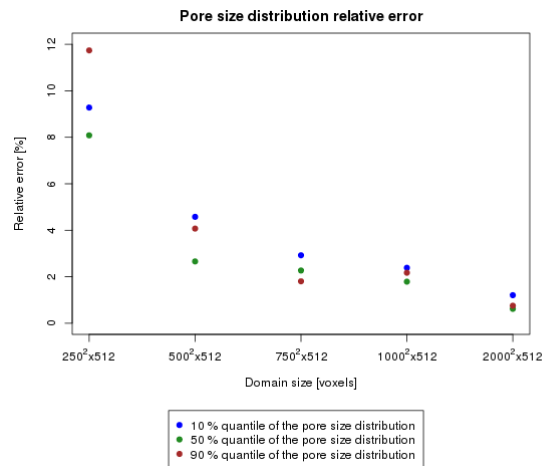


Figure 5.6 – Relative error of three different quantiles of the pore size distribution.

6

Applications

6.1 Validation of an automatic fiber analysis tool

In this section, we validate the automatic fiber thickness and orientation measurement technique for two-dimensional (2D) scanning electron microscopy (SEM) images proposed by Altendorf et al. 2010. For validation, realizations generated from the stochastic model proposed in Chapter 3 Section 3.3 are used. A short summary of the automatic fiber thickness and orientation computation is given in Appendix. Parts of this section were published in Easwaran et al. 2015 and Easwaran et al. 2016a.

6.1.1 Validation of fiber thickness estimation

First, we generate 3D fiber systems using the stochastic model developed in Chapter 3 Section 3.3. SEM images of realizations of our model are simulated using the method described by Prill and Schladitz 2013. Then, the automatic thickness estimation method is used to estimate the fiber thickness distribution from the SEM images. The advantage of this model-based approach is that the true fiber thickness distribution in the models is known. Hence, error prone manual determination of ground-truth data can be avoided.

However, SEM images do not contain the full spatial information. Thus, even perfect image processing could not regain the true 3D thickness distribution. Therefore, it was decided to compare to the "perfect" SEM image instead. More precisely, the image used to estimate the true solution is a projection similar to an SEM image, but additionally contains all exact fiber boundaries. That is, to obtain the true solution, the simulated labeled 3D image is orthogonally projected onto the xy -plane yielding a 2D labeled projection. Binarization of this 2D image gives a binary image with exact fiber boundaries. The automatic thickness estimation algorithm is applied to this binary image to obtain the true solution.

The fiber thickness distribution obtained by the automatic approach and the true solution of various fiber systems are compared to validate the automatic thickness measurement. In particular, fiber systems with thin fibers from 6 voxels and thick fibers up to 16 voxels are considered. And the combination of both thin and thick fibers are also studied. Some of these comparison results with the corresponding 3D realization and SEM image are presented in Figures 6.1, 6.2, and 6.3. In these realizations, 40% of the given fibers form bundles of four fibers, 30% of the fibers form bundles of three fibers, 20% of the fibers are paired, and the remaining fibers are modeled as individual fibers. The common parameters are window side length = 512 voxels, $\beta = 10$, $\kappa_1 = 10$ and $\kappa_2 = 100$. The

volume fractions and fiber thicknesses are given in the figure captions. In the following experiments, all fibers in realizations have constant radius along the fiber.

Plots in Figures 6.1 and 6.2 show that the fiber thickness distribution estimated by the automatic approach is able to capture all peaks of the true fiber diameter distribution with an accuracy of 1 pixel for thin fibers, i.e., fibers with a thickness less than 10 pixels. This observation may not be true for thick fibers from 10 pixels thickness on. In particular, the automatic approach features two peaks, whereas the true solution has only one peak in Figure 6.3. This extra peak occurs due to overlaying and shadowing effects of fibers in the SEM images (see Figure 6.4) which cannot be avoided. Note that in all the three plots, the true solution estimated from the 2D projection image has peaks exactly at the input fiber thickness of the 3D realization.

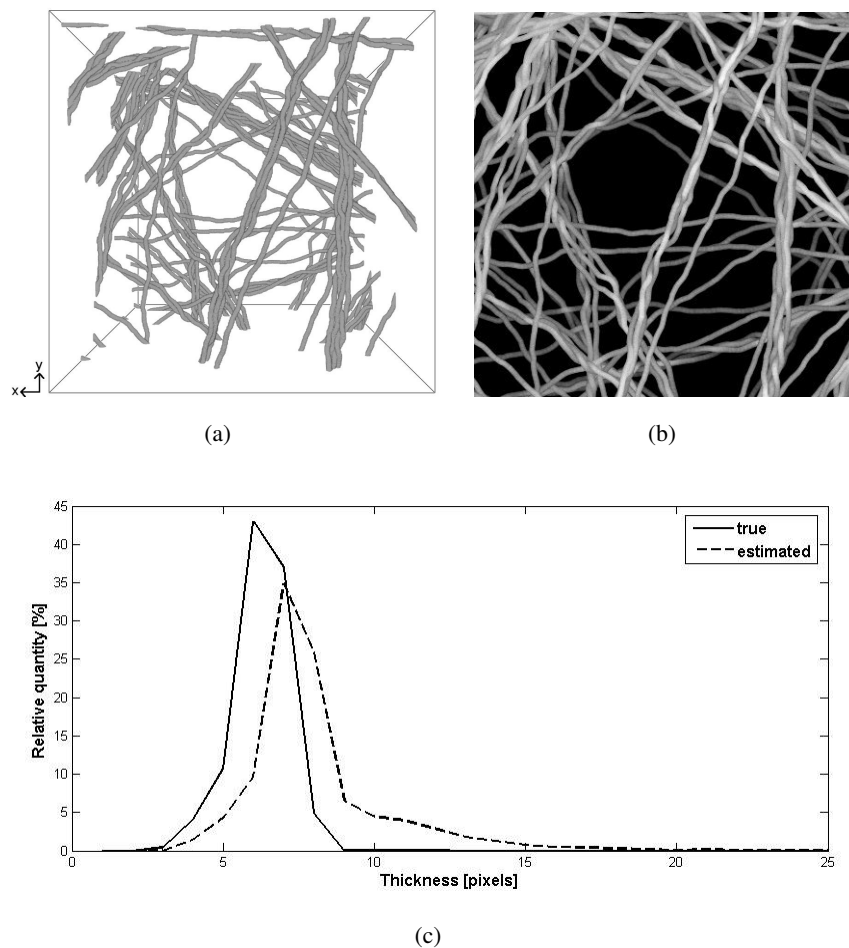


Figure 6.1 – Realization of a fiber system with fiber bundles and its thickness estimation. Input fiber thickness for the 3D model is 6 voxels and volume fraction = 1%. (a) Realization of the 3D fiber model. (b) Synthetic SEM image of the 3D model. (c) Area weighted thickness histogram of (b). The automatic approach captures the peak obtained by the true solution. The overestimation occurs due to the image contrast. Some parts of the fiber bundles are treated as single fiber.

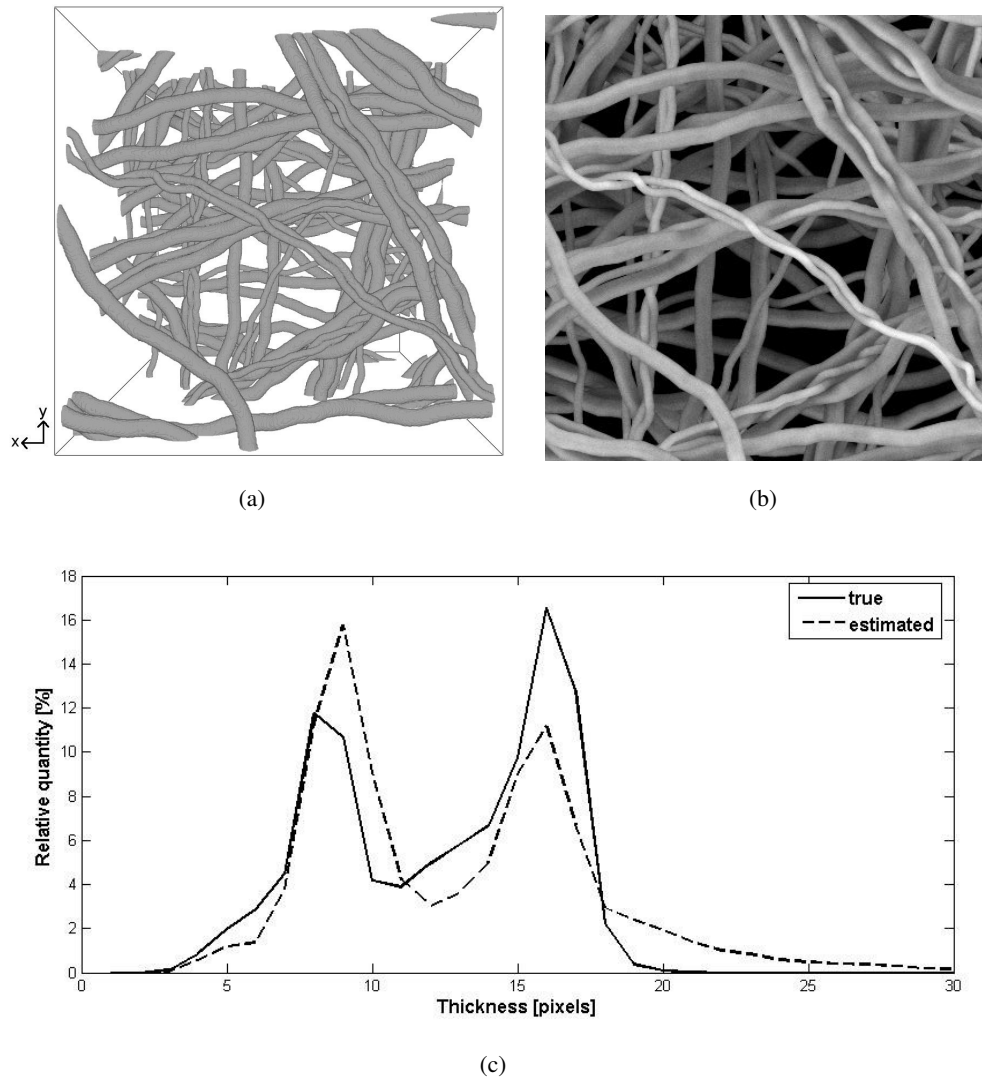


Figure 6.2 – Realization of a fiber system with fiber bundles and its thickness estimation. Input fiber thicknesses for the 3D model are chosen as 8 and 16 voxels each with probability 0.5 and volume fraction = 5%. (a) Realization of the 3D fiber model. (b) Synthetic SEM image of the 3D model. (c) Area weighted thickness histogram of (b). The automatic approach captures the two peaks obtained by the true solution. Frequencies of the peaks are different.

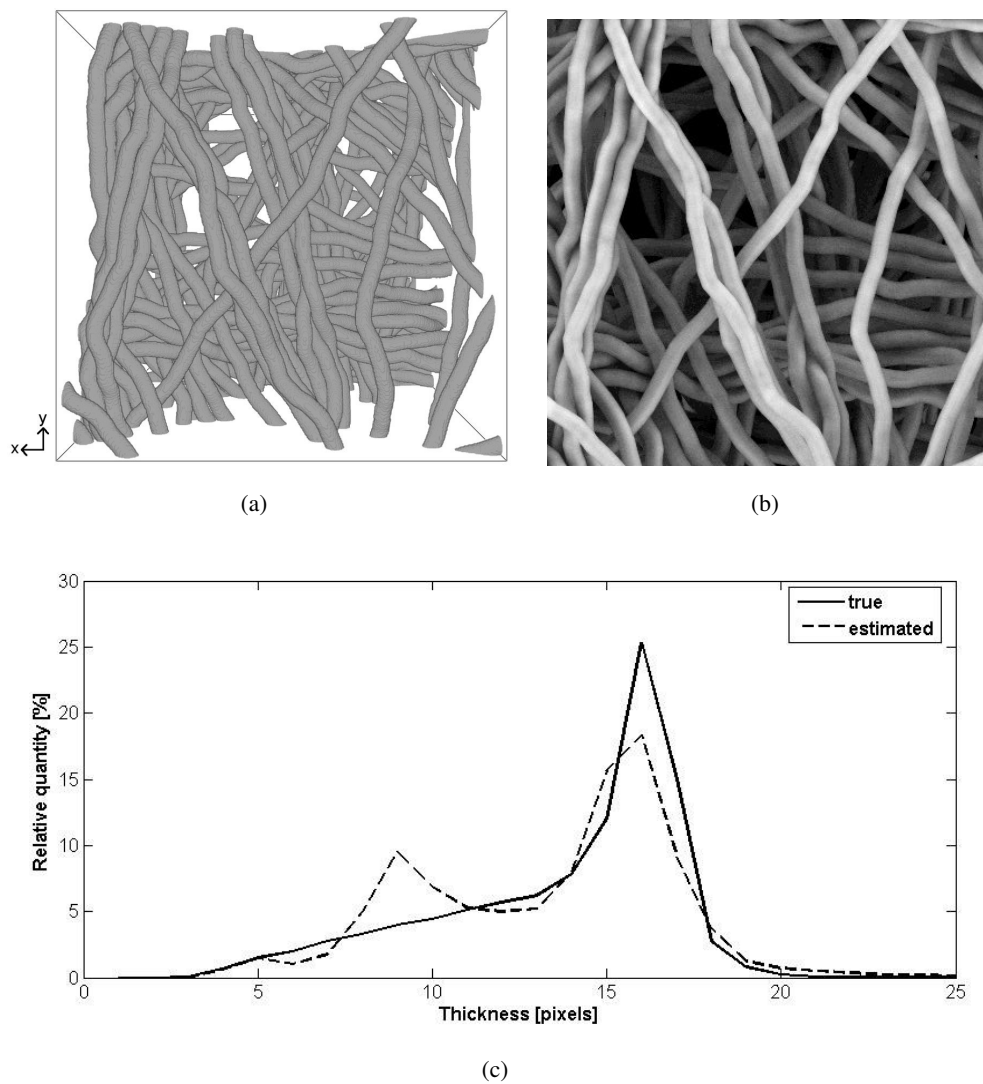


Figure 6.3 – Realization of a fiber system with fiber bundles and its thickness estimation. Input fiber thickness for the 3D model is 16 voxels and volume fraction = 12%. (a) Realization of the 3D fiber model. (b) Synthetic SEM image of the 3D model. (c) Area weighted thickness histogram of (b). The automatic approach features an additional peak.

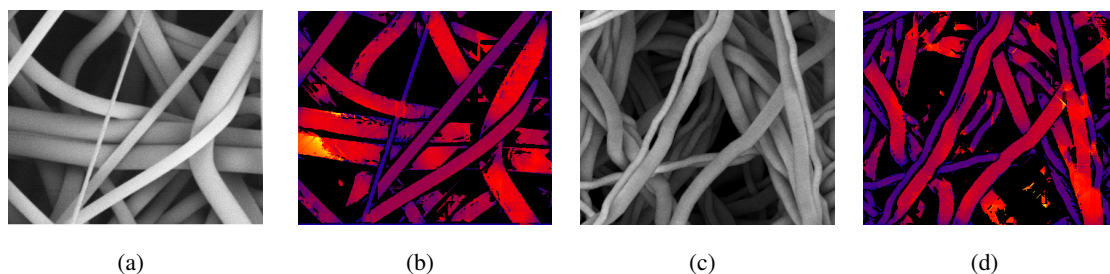


Figure 6.4 – SEM of the real material (a) and its thickness map (b). Simulated SEM image (c) and its thickness map (d). Both in the SEM image of a real material and simulated SEM images, some of the fibers overlay others and shadows of upper fibers fall on lower fibers. The estimation method underestimates the fiber thickness of the lower fibers due to these overlaying and shadowing effects.

6.1.2 Validation of fiber orientation estimation

As mentioned in the previous subsection, here also, SEM images are simulated from the generated 3D fiber systems. Then, the local fiber orientation distribution from the SEM image is estimated using the automatic fiber orientation estimation. In order to validate the estimated measurements, the ground truth is computed as in the following. As we already know, a fiber in our 3D model is represented as a chain of spheres $\{p_{kj1}, \dots, p_{kjl_{kj}}\}$ with $p_{kji} = (x_{kji}, \mu_{kji}, r_{kji}) \in \mathbb{R}^3 \times S^2 \times \mathbb{R}_{>0}$ where x_{kji} , μ_{kji} , and r_{kji} are center coordinate of the sphere, local orientation of the fiber and radius of the sphere, respectively (refer Chapter 3 Section 3.3). The local orientation μ_{kji} of the fiber is $\frac{x_{kj(i+1)} - x_{kji}}{|x_{kj(i+1)} - x_{kji}|}$. The spherical coordinates of μ_{kji} can be written as $(\theta_{kji}, \phi_{kji}) \in [0, \pi) \times [0, 2\pi)$ (refer Chapter 2 Section 2.2). Furthermore, the azimuthal angle ϕ_{kji} at the center coordinate of the kji -th sphere is assigned to all other voxels of the kji -th sphere. The ground truth is obtained by orthogonally projecting the azimuthal angle ϕ image onto the xy -plane.

The ground truth and the local orientation distribution estimated from the SEM image by the automatic approach are compared in Figure 6.5. Parameters used to simulate the realization in Figure 6.5 are window side length = 512 voxels, $\beta = 10$, $\kappa_1 = 10$ and $\kappa_2 = 100$. The volume density of the fiber system is 10%, 40% of the fibers form bundles of four fibers, 30% of the fibers form bundles of three fibers, 20% of the fibers are paired, and the remaining fibers are modeled as individual fibers. Fiber thickness is 10 voxels.

A visual comparison of the ground truth (Figure 6.5(d)) and the estimated orientation (Figure 6.5 (e)) shows that they are close to each other. Furthermore, we observe that boundary pixels of the estimated orientation contain some noise. In order to get rid of this noise, the morphological erosion is applied on the mask image to remove boundary pixels (Figure 6.5 (f)). For further reference, we denote the result image after erosion as "mask erosion". The ground truth and the estimate image is masked with "mask erosion" (Figures 6.5 (g) and 6.5 (h)). The histograms of the ground truth image (Figure 6.5 (d)), the estimated image (Figure 6.5 (e)), the ground truth masked with "mask erosion" image (Figure 6.5 (g)) and the estimated masked with "mask erosion" image (Figure 6.5 (h)) are plotted in Figure 6.5 (i). Each histogram is smoothed using the R function *density()* with bandwidth 3 (R Core Team 2013). It shows that the ground truth and the ground truth masked with "mask erosion" do not differ. Whereas the estimated masked with "mask erosion" slightly enhances the peak of the estimated orientation. Visually, the images and the plots of the ground truth and the estimated orientation are equal.

This experiment is repeated for two more realizations as shown in Figures 6.6 and 6.7. In these two realizations, except the fiber thickness all the other parameters are the same as in Figure 6.5. The fiber thickness for the realization in Figure 6.6 is 20 voxels and fiber thicknesses for the realization in Figure 6.7 are randomly chosen as 8 and 16 voxels with equal probability. We obtain similar results as for the realization in Figure 6.5.

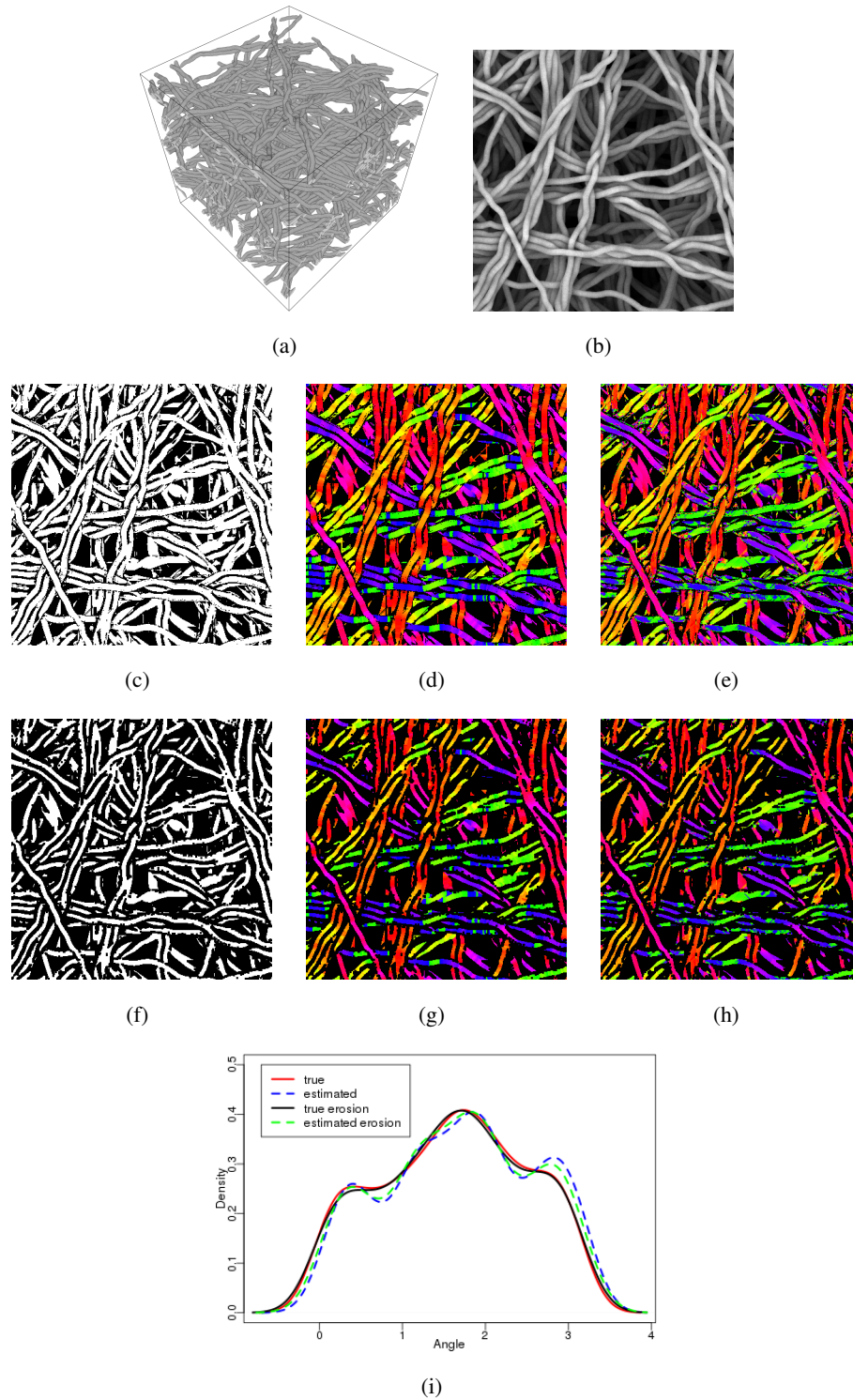


Figure 6.5 – (a) Realization of the 3D fiber model. (b) Synthetic SEM image of the 3D model. (c) Mask image. (d) Ground truth. (e) Estimated local fiber orientation of (b). (f) Mask image after erosion. (g) Ground truth masked with (e). (h) Estimated masked with (e). (i) Ground truth and estimated fiber orientation plot.

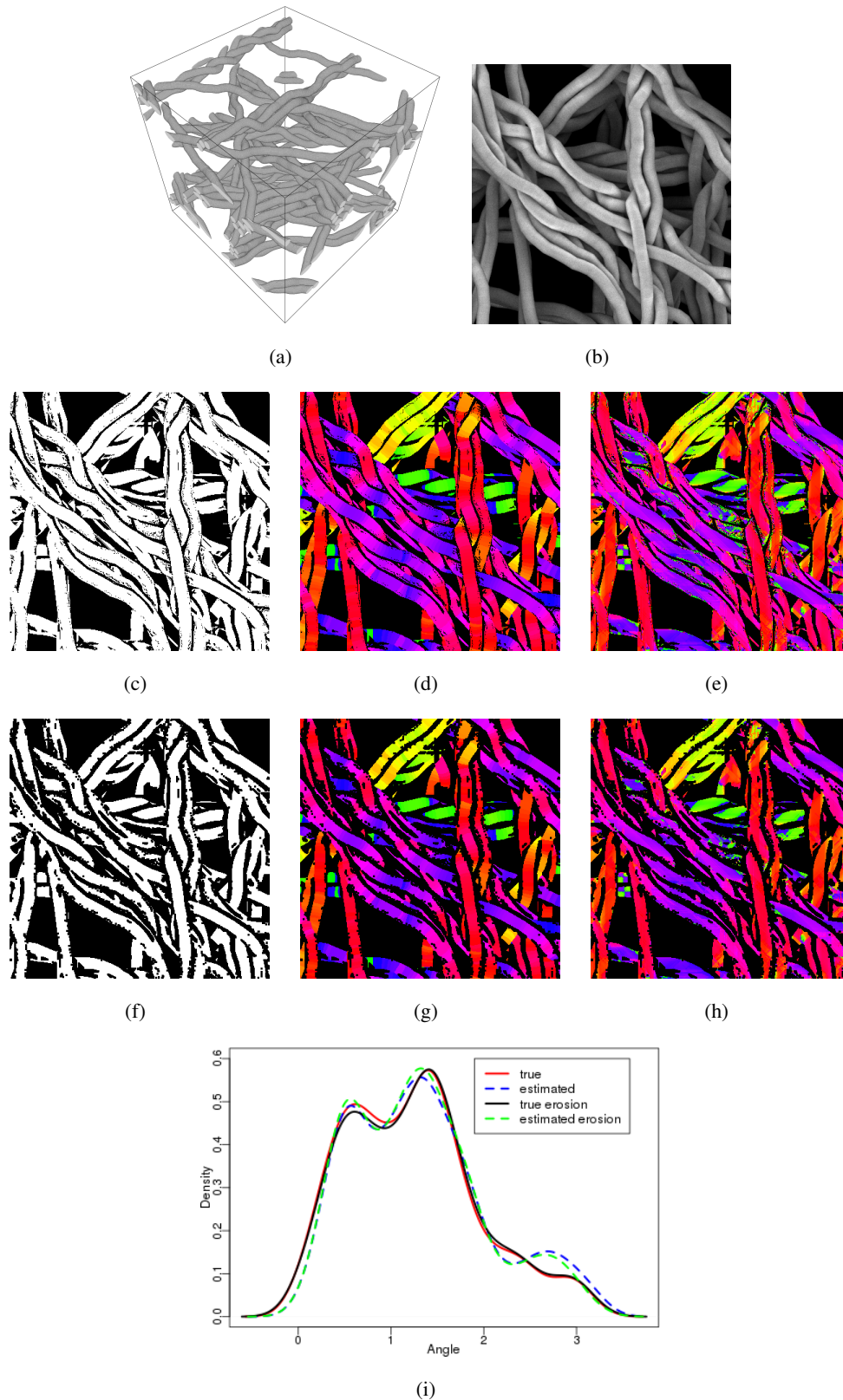


Figure 6.6 – (a) Realization of the 3D fiber model. (b) Synthetic SEM image of the 3D model. (c) Mask image. (d) Ground truth. (e) Estimated local fiber orientation of (b). (f) Mask image after erosion. (g) Ground truth masked with (e). (h) Estimated masked with (e). (i) Ground truth and estimated fiber orientation plot.

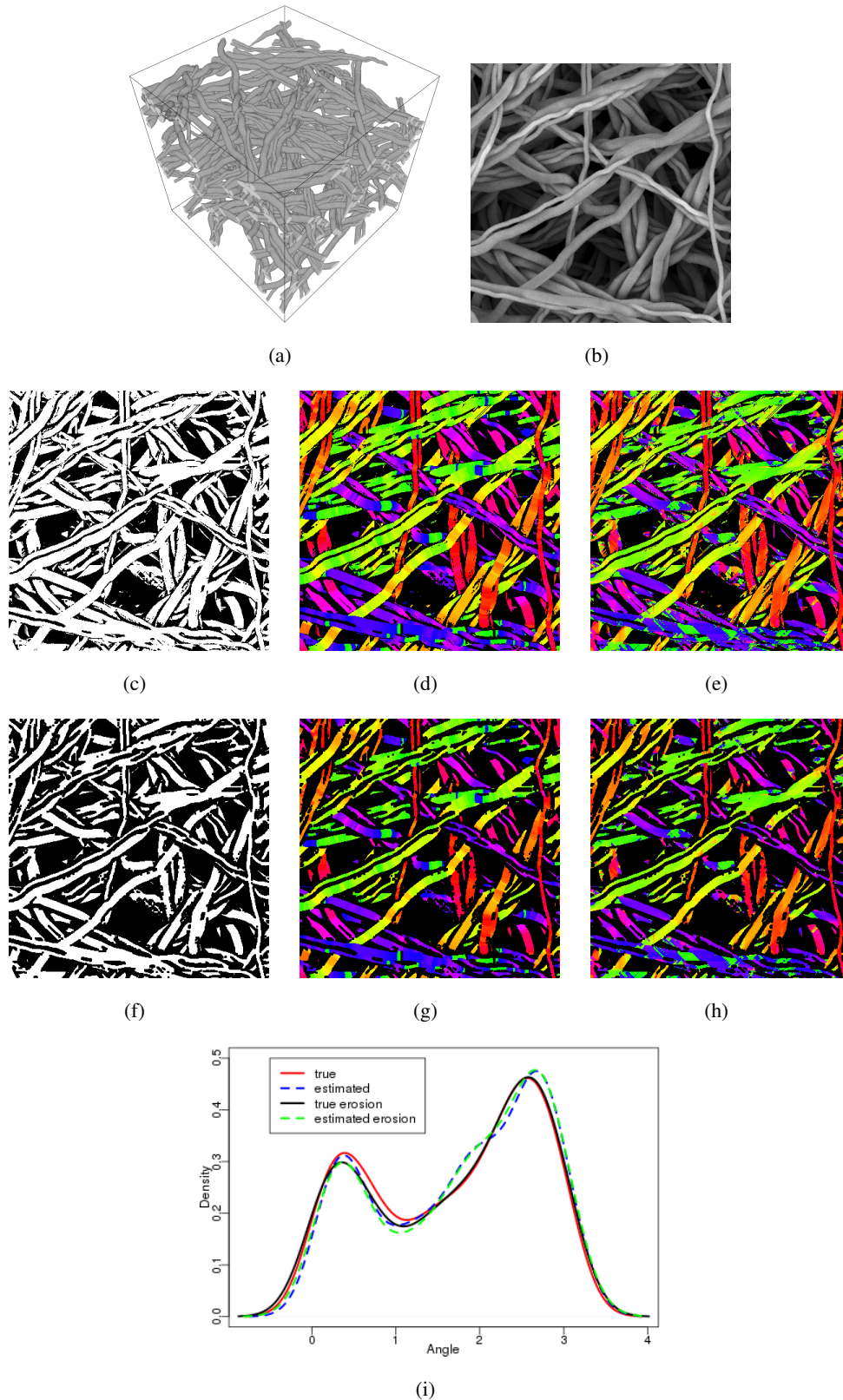


Figure 6.7 – (a) Realization of the 3D fiber model. (b) Synthetic SEM image of the 3D model. (c) Mask image. (d) Ground truth. (e) Estimated local fiber orientation of (b). (f) Mask image after erosion. (g) Ground truth masked with (e). (h) Estimated masked with (e). (i) Ground truth and estimated fiber orientation plot.

6.2 Modeling of bio-pore structures

As we described in the introduction of this thesis, bio-pores in the computed tomography (CT) images have to be segmented in order to analyze their size, shape, orientation, etc. Recently, Bauer et al. 2017 compared various image segmentation algorithms for bio-pore segmentation from the CT images of the soil. Precisely, they compared the variational segmentation model (Bauer et al. 2017), the indicator kriging method (Oh and Lindquist 1999), global gray value thresholding (Otsu 1979), and the morphological extract holes transform (Soille 1999). Since the ground truth is not known for the real data, synthetic data is required to validate these segmentation techniques quantitatively.

We have observed from the CT image of a soil sample Ch2y-II from Pagenkemper et al. 2013 (see Figure 6.8 (a)) that bio-pores can be modeled as fibers. Ch2y-II was imaged with a voxel size of $463 \mu m$ at the Technical University Dortmund, Germany, Department of Mechanical Engineering. Size of the data is $185 mm \times 185 mm \times 455 mm$. Therefore, in this section, we propose a basic extension of the method from Altendorf and Jeulin 2011a to model bio-pores. Since bio-pores contain branch-like structure, we simulate fiber branches in our extended model.

As in Chapter 3 Section 3.1, here also we denote the system of fibers as

$$P = \bigcup_{j=1}^N P_j \quad (6.1)$$

where P_j is the j -th fiber of the system. It is denoted as a chain of spheres, i.e., $P_j = \{p_{j1}, \dots, p_{jl_j}\}$ with $p_{ji} = (x_{ji}, \mu_{ji}, r_{ji})$ where $x_{ji} \in \mathbb{R}^3$, $\mu_{ji} \in \mathcal{S}^2$ (unit sphere), and $r_{ji} \in \mathbb{R}_{>0}$ are center position of the sphere, local orientation of the fiber and radius of the sphere, respectively.

The first $n (< N)$ fibers are simulated using the random walk approach as described in Chapter 3 Section 3.1. The remaining $N - n$ fibers are simulated as branches of already existing fibers. In order to create branches, a fiber is randomly chosen from previously simulated fibers, say P_t . A sphere coordinate is randomly chosen from the fiber P_t , say x_{ti} . Simulate a new fiber starting from the coordinate x_{ti} using a random walk. A fiber branch simulated from this approach is shown in Figure 6.9 (a).

The following parameters were used to simulate realizations considered by Bauer et al. 2017. Window size $400^2 \times 984$ voxels, thicknesses of core fibers are randomly chosen as 10 and 16 voxels with equal probability, thicknesses of fiber branches are randomly chosen as 2 and 6 voxels with equal probability. β value for core fibers is 0.01 and for branches 0.5. The κ_1 and κ_2 values for both core and branch fibers are 10 and 100, respectively. The length of the main fibers is fixed as 1500 voxels and the lengths of branches are uniformly distributed on the interval $(0, 150]$. One of the fiber systems considered by Bauer et al. 2017 is shown in Figure 6.9 (b).

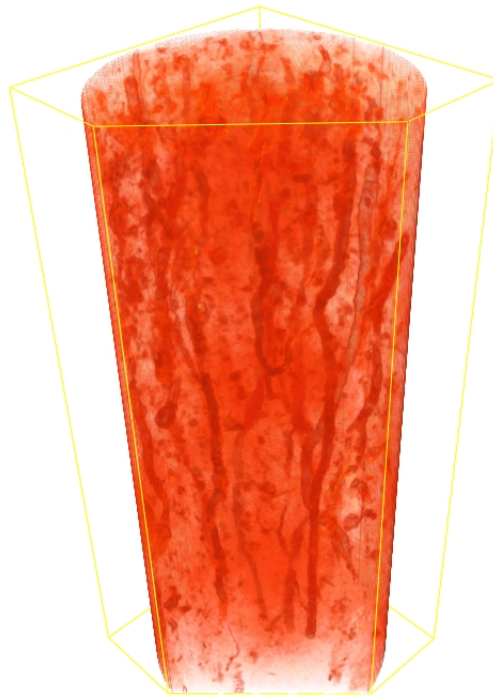


Figure 6.8 – Volume rendering of the CT image of the soil sample. Size: $399 \times 399 \times 983$ voxels with a voxel edge length of $463 \mu\text{m}$. Reprinted from *Computers & Geosciences*, 98, B. Bauer, X. Cai, S. Peth, K. Schladitz, G. Steidl, Variational-based segmentation of bio-pores in tomographic images, 1-8, Copyright (2017), with permission from Elsevier.

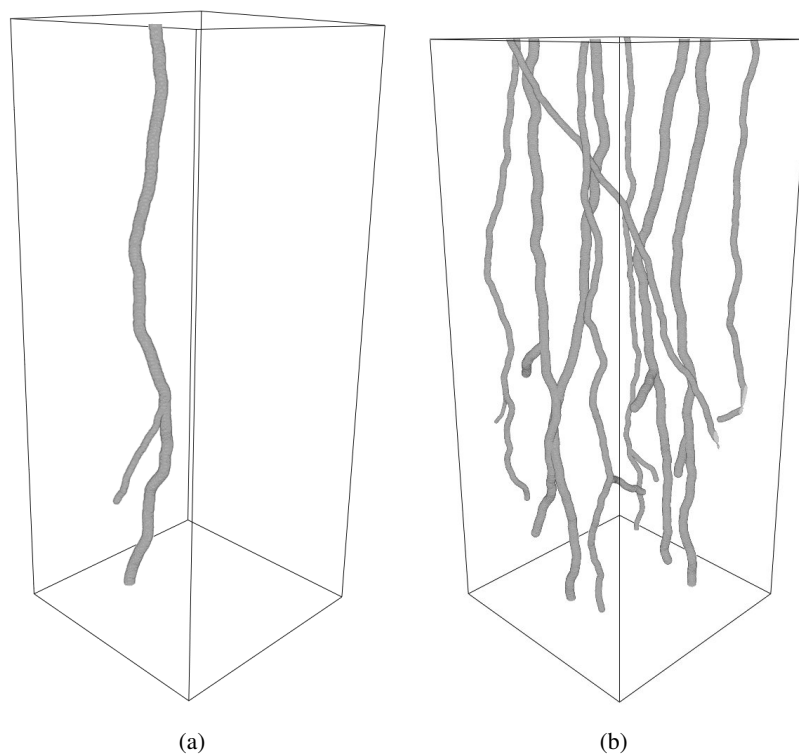


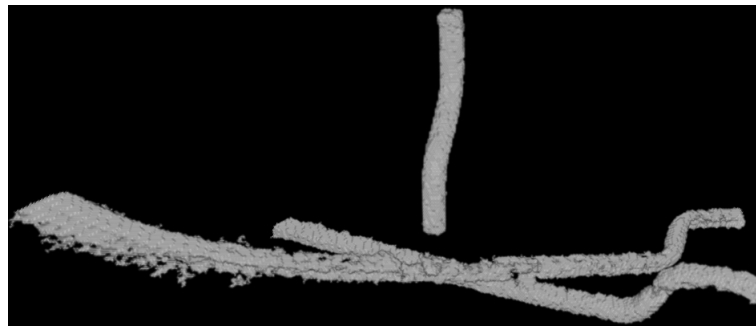
Figure 6.9 – (a) A fiber with a branch. (b) A fiber system with fiber branches

6.3 Separation and labeling of fibers in steel fiber reinforced concrete

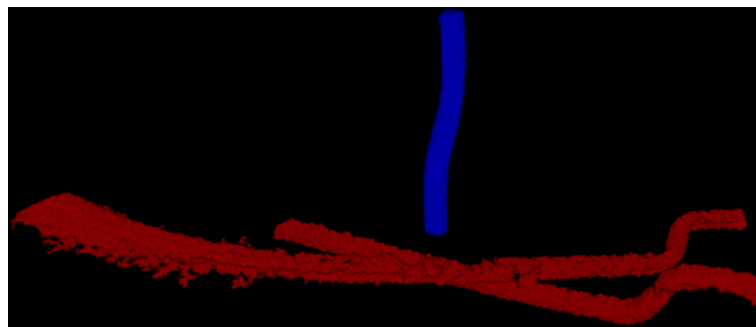
All images considered in this section are cropped for fiber clusters from a binarized 3D computed tomography (CT) image of steel fiber reinforced concrete (sample: TU Kaiserslautern and μ CT: Fraunhofer ITWM, Kaiserslautern). Original image size: $870 \times 923 \times 1705$ voxels with a voxel edge length of $77 \mu\text{m}$.

Concrete is a composite material and it is broadly used as a construction material. The durability and strength of the concrete can be adapted by making suitable changes in its ingredients such as aggregate, cement, water, etc. Plain (unreinforced) concrete has a low tensile strength and a low strain capacity. The weakness of the plain concrete can be discarded by embedding steel fibers, glass fibers or plastic fibers into the concrete. This type of concrete is called fiber reinforced concrete. It is widely used in commercial buildings, tunnel linings, septic tanks, slabs, etc. Properties of the fiber reinforced concretes such as compressive strength, tensile strength, post-cracking performance, etc., are influenced by the arrangement of the fibers in the concrete. In particular, the characteristics of the fiber reinforced concrete after cracking are strongly connected to the amount of fibers in the cracking zone, the orientation of fibers, the fiber length and so forth (Schuler et al. 2011). In order to analyze these properties, each fiber needs to be segmented and labeled. Once fibers are labeled, the orientation of the each fiber can be estimated. Moreover, the exact spatial position of the each fiber can be identified and fiber deformation after cracking can also be studied. However, fibers may form clusters during the concrete mixing. Standard labeling procedures assign a single label for all fibers in the cluster (see Figure 6.10). However, all fibers in the cluster should be separated and labeled.

Recently, the method based on the local fiber orientation which is computed on each fiber voxels, to separate fibers in sample of steel fiber reinforced concrete was introduced by Pastorelli and Herrmann 2016. The fibers are separated based on the assumption that the plot of the distribution of the local orientation vectors should have peaks for each fiber. However, there is only a single peak for two fibers which are oriented in the same direction. Since clusters considered in this section include fibers with identical orientation, their method cannot be considered. To this end, we apply a part of the fiber separation algorithm proposed by Altendorf 2011c to separate fibers from the clusters. Originally the algorithm is developed for glass fiber reinforced polymer which has fibers with low bending and circular cross section. However, our sample contains fibers with hooked-ends (see Figure 6.11). Apart from that, there are artifacts in the data and also some fiber voxels are missing (see Figure 6.11). Therefore, several pre- and post-processing steps are applied to separate fibers from clusters of steel fiber reinforced concrete.

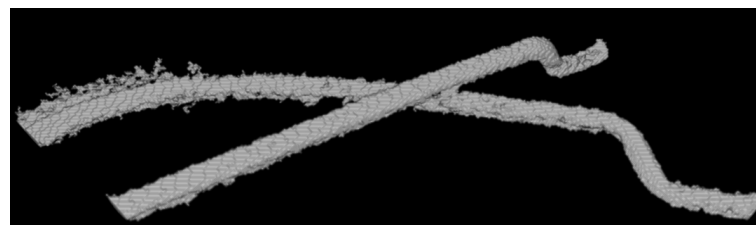


(a)



(b)

Figure 6.10 – (a) Cropped sample of steel fiber reinforced concrete with fiber cluster and single fiber (image size: $247 \times 301 \times 180$ voxels). (b) Labeled image from a standard labeling procedure.



(a)



(b)

Figure 6.11 – Noisy data of fiber clusters cropped from CT image of steel fiber reinforced concrete. (a) Image size: $257 \times 311 \times 100$ voxels. (b) Image size: $480 \times 114 \times 184$ voxels

6.3.1 Pre-processing

As a first preprocessing step, a morphological closure with structuring element ‘cube’ of size 3 and a median filter are applied. After that, the multiscale vessel enhancement filtering introduced by Frangi et al. 1998 is used to remove artifacts in the input image. It is used to enhance only fiber-like

structures in the image. This method is based on the eigenvalues of the Hessian matrix. Precisely, the Hessian matrix and its eigenvalues are computed on each voxel at various scales, based on the fiber thicknesses. The vesselness measure is calculated on each voxel based on these eigenvalues. Then the maximum vesselness response over the various scales is assigned at each voxel. The image after this filtering step is a float image and its gray values are in the interval $[0,1]$. Then, the Otsu thresholding method is applied to binarize this image. The binarized image contains fiber clusters with reduced noise on the surface. Due to energy limitations, there are holes in some of the fibers. Hence, a morphological dilation with structuring element ‘cube’ of size 3 is applied to fill those gaps in the fibers. The fiber separation algorithm is applied to this dilated image.

6.3.2 Fiber separation

We summarize the fiber separation algorithm from Altendorf 2011c in the following.

The fiber separation algorithm reconstructs each fiber as a chain of spheres. The algorithm is based on the input image (binary image), the radius image, the probability image and the marker image. The gray values of the radius image represent the fiber radius. The medial axis of the input image is considered as the marker image.

First, the Euclidean distance transform (EDT) is applied on the foreground of the input image. The result of this transformation is a gray value image where each foreground voxel value represents the distance to the closest background voxel. Hence, the EDT image has maximum gray values on the fiber core. The gray value of each voxel in the probability image P is calculated using the EDT image and the radius image as in Equation (6.2).

$$P(x) = \min \left\{ \frac{EDT(x)}{R(x)}, 1 \right\} \quad (6.2)$$

where $EDT(x)$ and $R(x)$ denote the gray value of the voxel x in the EDT image and the radius image, respectively. The gray values of the probability image are in the interval $[0, 1]$. It has higher values around the fiber core and lower values around the fiber boundary. The threshold p_{min} for the probability value is introduced. If the probability value of a fiber voxel is greater than p_{min} , the voxel is assumed to be in the fiber core.

Fiber reconstruction starts after computing the probability image and the marker image. The algorithm first selects a foreground voxel (x_0) from the marker image. If $P(x_0) > p_{min}$, x_0 is chosen as the initial coordinate for the fiber chain, otherwise the next foreground voxel in the marker image is tested. The fiber chain is extended from the initial coordinate in both fiber directions. The coordinates for subsequent spheres in the chain are computed as in the following. First, a voxel y which has maximum probability value among the 26 neighbors of the previous coordinate x_{i-1} is chosen. If the probability value at voxel y is higher than the threshold p_{min} , voxel y is assigned as the next sphere coordinate x_i . This step is repeated until the condition fails, i.e., $P(y) \leq p_{min}$. If the

condition fails, the above mentioned procedure is repeated to extend the fiber in the other direction. This process ends with a chain of coordinates once the condition fails. Then, the fiber is generated using these coordinates and the radii from the local radius image. This fiber reconstruction procedure is repeated for all other marker points which are not covered during previous reconstruction steps. A label is assigned to each reconstructed fiber. This algorithm ends up with a labeled image.

We apply the above mentioned approach to our pre-processed CT image of steel fiber reinforced concrete. The local fiber radius is estimated using the method proposed by Altendorf and Jeulin 2009. For all fiber clusters considered in this thesis, p_{min} is fixed to 0.6.

6.3.3 Post-processing

Since fiber separation is applied on the dilated image, the labeled image is masked with the original input image. Some small parts of fibers may not be reconstructed during fiber separation procedure due to low image resolution (see Figure 6.13). In order to extend labels to the missing regions, we do the following. The watershed transform is applied to the complement of the EDT image. The labeled image is used as a seeding image for the watershed segmentation. Then, the result image is masked with the original image. The image after masking is the labeled image of the original image. However, single fibers may split into two or more labels (see Figure 6.14). Hence, we manually merge those labels into a single label (see Figure 6.15 (a)). Whereas the standard particle separation approach splits a fiber into many small parts (see Figure 6.15 (b)). Precisely, for the specimen shown in Figure 6.12, the particle separation approach yields 663 labels and our approach yields only 15 labels. The manual merging is difficult for the particle separation approach compared to our method. More results are given in Figure 6.16 and Figure 6.17.



Figure 6.12 – One of the fiber clusters from CT image of steel fiber reinforced concrete (image size: $791 \times 232 \times 943$ voxels).

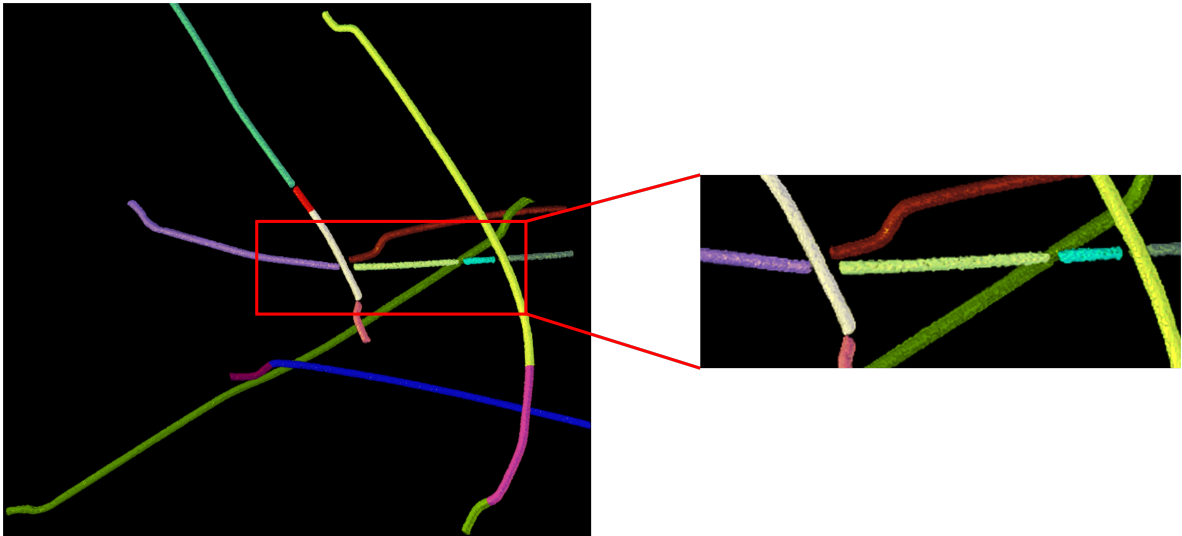


Figure 6.13 – Labeled image with gaps in the fiber.

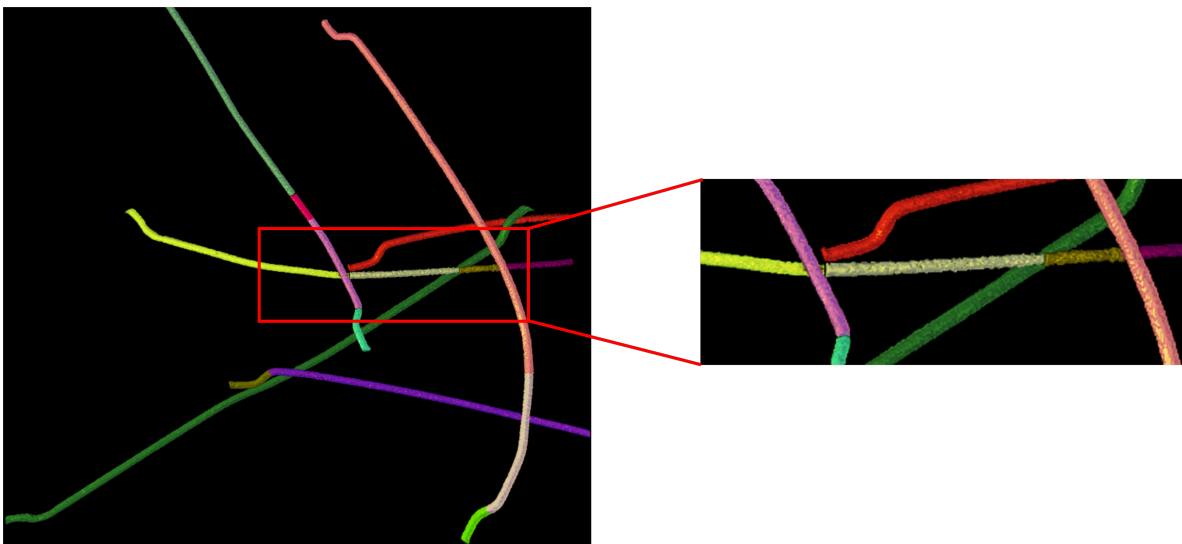


Figure 6.14 – Labeled image after filling the gaps. Some fibers have more than one label.

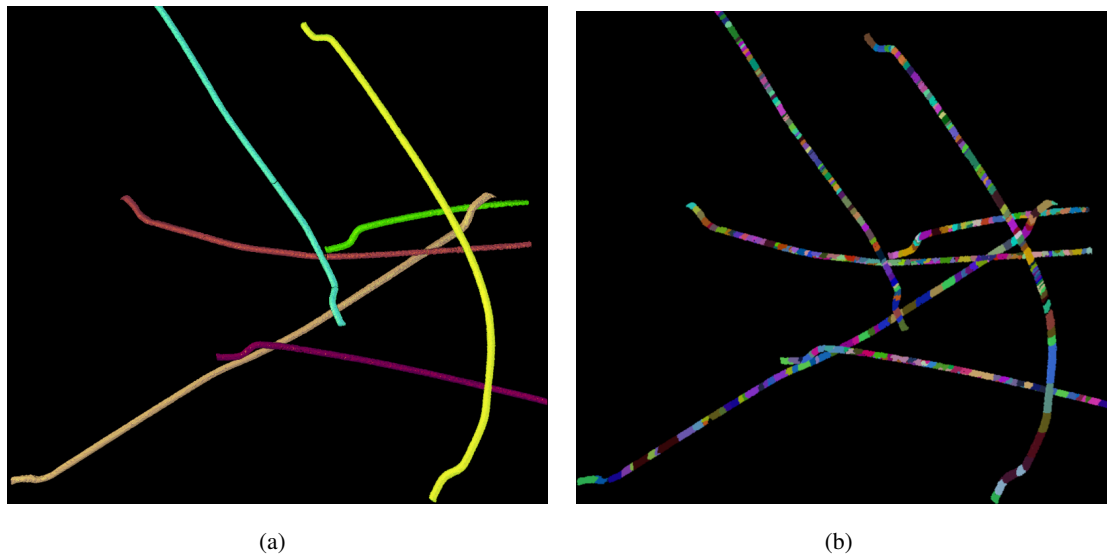


Figure 6.15 – (a) Labeled image after manual merging of labels in image shown in Figure 6.14. (b) Labeled image obtained from the standard particle separation.

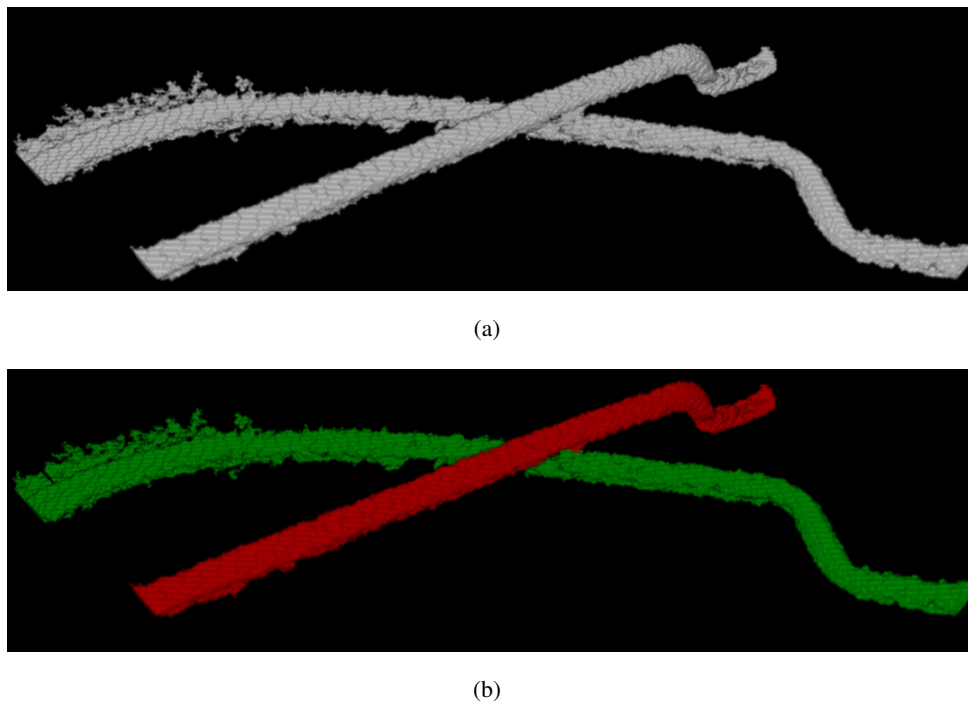
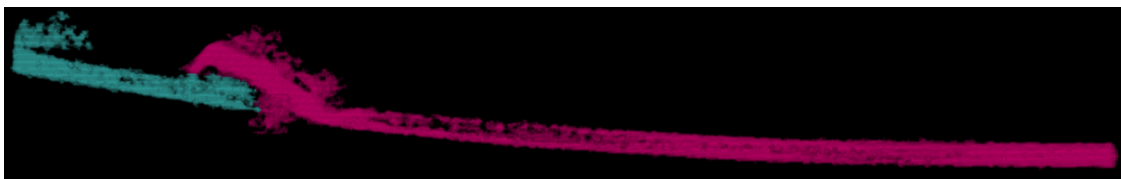


Figure 6.16 – (a) One of the fiber clusters from CT image of steel fiber reinforced concrete (image size: $257 \times 311 \times 100$ voxels). (b) Labeled image.



(a)



(b)

Figure 6.17 – (a) One of the fiber clusters from CT image of steel fiber reinforced concrete (image size: $480 \times 114 \times 184$ voxels). (b) Labeled image.

7

Conclusions and future work

7.1 Conclusions

This thesis dealt with a stochastic model for the microstructure of nonwoven materials. First the Altendorf-Jeulin approach was extended to model fiber systems with fibers of apparently infinite length. Then this approach was further extended to include fiber bundles into the system. We proposed two different methods for the modeling of fiber bundles. In Method I, fibers in a bundle were generated by using random walks starting from the initial sphere coordinate of the first fiber along its main orientation. In Method II, fibers in a bundle were simulated by duplicating the sphere centers of the initial fiber. Both methods can generate fiber bundles with entwined fibers. In addition, Method II can also simulate fiber bundles with parallel fibers. A parameter ε was introduced in Method II to switch between entwined and parallel fibers.

The maximum-likelihood (ML) estimator for the parameter β for the Schladitz distribution using the local fiber orientation was considered. The local orientation was computed using the Hessian-based approach and a technique based on inertia moments. The estimator was studied for straight and curved fibers. For straight fibers, both methods correctly estimated β value for input $\beta \leq 5$, and $\beta \leq 3$ for slightly curved fibers. Since the approach based on inertia is independent of scale, we used the inertia-based method to estimate β from the computed tomography (CT) image of the real nonwoven material. Our novel stochastic model was fitted to the CT data. The visual appearance of the simulated microstructure realizations of our model and the CT image were comparable. In order to evaluate the model fitting systematically, five realizations for various combinations of κ_1 and κ_2 were generated. The pressure drops computed in the CT image (8.05527 Pa) and in the virtual microstructures were compared. The pressure drops derived from the realizations of our model differs from the one calculated in the CT image by a relative error of 8% only.

The representative domain size was estimated for our microstructure model. A simulation and a statistical approach were used for the study. The simulation study was performed for the packing density, the pore size distribution and the pressure drop. The statistical approach was used to calculate the representative domain size for the packing density and the pressure drop. The simulation results were compared with the statistical results. It turned out that the statistical approach can be used to estimate the representative domain size for the given property more precisely and using less generated microstructures than the purely simulation based approach.

Furthermore, our fiber bundle model was used to validate the automatic fiber thickness and orienta-

tion estimation proposed by Altendorf et al. 2010. The automated fiber thickness measurements were able to capture the peaks of the true fiber thickness distributions with an accuracy of ± 1 pixel for thin fibers up to 10 pixels thickness. However, the method starts to feature an additional peak for thick fibers from 10 pixels thickness only because of fiber overlay effects. Note that these fiber overlay effects are inherent to the SEM imaging technique. The fiber orientation distribution estimated using the automatic orientation estimation was coinciding with the ground truth.

A basic extension of the Altendorf-Jeulin modeling approach to simulate a bio-pore structure was introduced. The extended model was considered by Bauer et al. 2017 to compare four different segmentation methods for bio-pores. Furthermore, fibers in the specimen of steel fiber reinforced concrete were separated and labeled. The method was tested on 17 clusters of a specimen of steel fiber reinforced concrete and it separated fibers in the all 17 clusters.

7.2 Future work

In recent days, applications of composite nonwovens are emerging. Spunbond-Meltblown-Spunbond (SMS) nonwoven is an example for composite nonwovens. SMS nonwovens comprises of two spunbond layers (large and strong filaments) inter laid with a meltblown layer (relatively small and soft fibers) (refer Das and Pourdeyhimi 2014 Chapter 1 Section 1.2.3). The microstructure of the composite nonwoven could be modeled by introducing layers into our proposed fiber bundle model.

Future work should find a proper method to estimate bending parameters, the frequency of fiber bundles, and the number of fibers in each bundle without segmenting individual fibers from the CT data. Bending parameters could be estimated from the local changing in the normal vector field along the fiber (Kronenberger et al. 2015). Fiber bundles could be segmented based on local fiber orientations (Sliseris et al. 2016). Furthermore, the estimation of an anisotropy parameter β for curved fibers should be improved.

It could be worthwhile to extend our representative domain size study to other filter properties such as dust holding capacity, filter efficiency, etc. Our model could be used to investigate some more automatic fiber analysis tools, for example, DiameterJ and OrientationJ plugins in ImageJ (<https://imagej.net>).

1

Appendix

A.1 The method for fiber orientation and radius estimation

The automatic fiber orientation and radius estimation method based on moments of inertia in binary and gray value images is introduced by Altendorf and Jeulin 2009. A summary of this estimation method is given in the following.

Orientation estimation

Assume that a binary image of a fiber system is given. Let $I \subset \mathbb{N}^2$ be the set of image pixels, and $b : I \rightarrow \{0, 1\}$ the initial binary image. The foreground is given as the set of all coordinates i with $b(i) = 1$. For each foreground pixel, the distance to the background in the eight or twenty six sampled directions (8 directions in 2D and 26 directions in 3D) forming the eight or twenty six neighborhood N (coordinate directions and diagonals) is calculated. This distance information $d : I \times N \rightarrow \mathbb{R}_{>0}$ is useful for estimating the endpoints of the centralized chords in all sampled directions via $e : I \times N \rightarrow I$, $e(i, vs) = \frac{1}{2} (d(i, vs) + d(i, -vs)) vs$. Having these endpoints, one computes for each pixel the moments of inertia

$$M_{pq}(i) = \sum_{l=0}^7 (e_x(i, vs_l))^p (e_y(i, vs_l))^q \quad p, q = 0, 1, 2, \quad \text{for 2D and} \quad (1.1)$$

$$M_{pqr}(i) = \sum_{l=0}^{25} (e_x(i, vs_l))^p (e_y(i, vs_l))^q (e_z(i, vs_l))^r \quad p, q, r = 0, 1, 2, \quad \text{for 3D} \quad (1.2)$$

$$(1.3)$$

where $e_x(i, vs_l)$, $e_y(i, vs_l)$, and $e_z(i, vs_l)$ denote the x , y , and z components of the $e(i, vs_l)$, respectively.

The inertia tensor for 2D is given by

$$M(i) = \frac{1}{8} \begin{pmatrix} M_{20}(i) & M_{11}(i) \\ M_{11}(i) & M_{02}(i) \end{pmatrix} \quad (1.4)$$

The inertia tensor for 3D is given by

$$M(i) = \frac{1}{26} \begin{pmatrix} M_{200}(i) & M_{110}(i) & M_{101}(i) \\ M_{110}(i) & M_{020}(i) & M_{011}(i) \\ M_{101}(i) & M_{011}(i) & M_{002}(i) \end{pmatrix} \quad (1.5)$$

The eigenvalues of $M(i)$ are denoted by $\lambda_1(i)$, $\lambda_2(i)$ and $\lambda_3(i)$. The eigenvector of $M(i)$ corresponding to its largest eigenvalue is the main inertia axis. This main axis of inertia gives a first estimate

of the local fiber orientation v . However, v is biased towards the sampled directions. To account for this bias, the estimate is corrected as in the following.

For 2D,

$$v'(i) = \frac{1}{2} \arctan \left(\sqrt[3]{\tan \left(2 \left(v(i) - j \frac{\pi}{4} \right) \right)} \right) + j \frac{\pi}{4} \quad (1.6)$$

if $j \frac{\pi}{4} \leq v(i) < (j+1) \frac{\pi}{4}$, $j \in \mathbb{N}$.

For 3D,

$$v'(i) = v(i) + \sum_{l=0}^{25} t(\angle(v_{s_l}(i), v(i))) \text{proj}(v_{s_l}(i), v(i)) \quad (1.7)$$

where

$\text{proj}(v_{s_l}, v)$ denotes the projections of the sampled directions v_{s_l} on the 2D subspace orthogonal to the estimated orientation v . It is defined by

$$\text{proj}(v_{s_l}, v) = v_{s_l} - (v \cdot v_{s_l})v \quad (1.8)$$

and

$$t(d) = \begin{cases} -0.2 \sin(\pi(4d/\pi)^{0.424}), & d < \pi/4 \\ 0, & \text{else.} \end{cases}$$

Radius estimation

In 2D, one can estimate the fiber radius with the help of the moments of inertia as follows:

$$r(i) = \sqrt{\frac{\lambda_2(i)}{f(v'(i))}} \quad (1.9)$$

with

$$f(v'(i)) = \begin{cases} \frac{2 - \sqrt{3 \cos^2(4(\frac{\pi}{2} - v(i)))} - 1}{\sin^2(4(\frac{\pi}{2} - v(i)))}, & \text{when the denominator is } \neq 0 \\ \frac{3}{4}, & \text{else.} \end{cases}$$

In 3D, radius corresponds to the each centralized distances $d(i, v_{s_l})$ is defined as

$$r_l(i) = d_l(i, v_{s_l}) \sin(\angle(v'(i), v_{s_l}(i))) \quad (1.10)$$

The final radius estimate for each voxel is calculated as in the following:

$$r(i) = \frac{1}{8} \sum_{l=10}^{17} r_l(i), \quad (1.11)$$

using the ordered sequence of the radius estimates (1.10):

$$r_1(i) \leq r_2(i) \leq \dots \leq r_{26}(i) \quad (1.12)$$

An extension for gray value images is obtained using quasi distances (Beucher [2007](#)). In this case, it is important to define some threshold of gray value changes to distinguish important changes from noise.

Academic curriculum vitae

- 04/2014 - 05/2017 Ph.D. Student in Mathematics
University of Kaiserslautern, Department of Mathematics, Kaiserslautern, Germany
Fraunhofer ITWM, Department of Image Processing, Kaiserslautern, Germany
- 10/2011 - 12/2013 M.Sc. in Mathematics International
University of Kaiserslautern, Department of Mathematics, Kaiserslautern, Germany
- 06/2009 - 04/2011 M.Sc. in Mathematics
Madurai Kamaraj University, School of Mathematics, Madurai, India
- 06/2006 - 04/2009 B.Sc. in Mathematics with Computer Application
Bharathiar University, KonguNadu Arts and Science College, Coimbatore, India

Akademischer Lebenslauf

- 04/2014 - 05/2017 Ph.D. im Fach Mathematik
Technische Universität Kaiserslautern, Fachbereich Mathematik, Kaiserslautern,
Deutschland
Fraunhofer ITWM, Bildverarbeitung, Kaiserslautern, Deutschland
- 10/2011 - 12/2013 M.Sc. in Mathematik International
Technische Universität Kaiserslautern, Fachbereich Mathematik, Kaiserslautern,
Deutschland
- 06/2009 - 04/2011 M.Sc. in Mathematik
Madurai Kamaraj Universität, School of Mathematics, Madurai, Indien
- 06/2006 - 04/2009 B.Sc. in Mathematik mit Computeranwendungen
Bharathiar Universität, KonguNadu Arts and Science College, Coimbatore, Indien

Bibliography

- Abdullah, N. R., Shahrudin, N. S., Ihsan Mamat, A. M., Kasolang, S., Zulkifli, A., and Mamat, R. (2013). "Effects of air intake pressure to the fuel economy and exhaust emissions on a small SI engine". *Procedia Engineering* 68, pp. 278–284.
- Altendorf, H. (2011c). "3D Morphological analysis and stochastic modeling of random fiber networks-applied on glass fiber reinforced composites". PhD thesis. Mines ParisTech, TU Kaiserslautern and Fraunhofer ITWM.
- Altendorf, H. and Jeulin, D. (2009). "3D directional mathematical morphology for analysis of fiber orientations". *Image Analysis & Stereology* 28 (3), pp. 143–153.
- (2011a). "Random-walk-based stochastic modeling of three-dimensional fiber systems". *Physical Review E* 83 (4), p. 0141804.
- (2011b). "Stochastic modeling of a glass fiber reinforced polymer". *Lecture Notes in Computer Science* 6671, pp. 439–450.
- Altendorf, H., Didas, S., and Batt, T. (2010). "Automatische Bestimmung von Faserradienverteilungen". *Forum Bildverarbeitung*. Ed. by F. P. Leon and M. Heizmann. KIT Scientific Publishing, pp. 59–70.
- Altendorf, H., Jeulin, D., and Willot, F. (2014). "Influence of the fiber geometry on the macroscopic elastic and thermal properties". *International Journal of Solids and Structures* 51 (23-24), pp. 3807–3822.
- Bauer, B., Cai, X., Peth, S., Schladitz, K., and Steidl, G. (2017). "Variational-based segmentation of bio-pores in tomographic images". *Computers & Geosciences* 98, pp. 1–8.
- Beneš, V. and Rataj, J. (2004). *Stochastic geometry: selected topics*. Kluwer academic publishers.
- Beucher, S. (2007). "Numerical residues". *Image and Vision Computing* 25 (4), pp. 405–415.
- Bezrukov, A., Bargieł, M., and Stoyan, D. (2002). "Statistical analysis of simulated random packings of spheres". *Particle and Particle Systems Characterization* 19 (2), pp. 111–118.
- Bharadwaj, R., Patel, A., Chokdepanich, S., and Chase, G. G. (2008). "Oriented fiber filter media". *Journal of Engineered Fibers and Fabrics* 3 (2).
- Bourke, N., Carty, G., Crowe, M., and Lambert, M. (1995). *Water treatment manuals - filtration*. The Environmental Protection Agency, Ireland.
- Chapelle, L., Lévesque, M., Brøndsted, P., Foldschack, M. R., and Kusano, Y. (2015). "Generation of non-overlapping fiber architecture". *Proceedings of the 20th International Conference on Composite Materials*.
- Das, D. and Pourdeyhimi, B., eds. (2014). *Composite nonwoven materials: Structure, Properties and Applications*. Woodhead Publishing.

- Dirrenberger, J., Forest, S., and Jeulin, D. (2014). “Towards gigantic RVE sizes for 3D stochastic fibrous networks”. *International Journal of Solids and Structures* 51 (2), pp. 359–376.
- Easwaran, P., Lehmann, M. J., Wirjadi, O., Prill, T., Didas, S., and Redenbach, C. (2015). “Automatic fiber thickness measurement in SEM images validated using synthetic data”. *Proceedings of FILTECH 2015*. Filtech Exhibitions Germany, Cologne.
- (2016a). “Automatic fiber thickness measurement in scanning electron microscopy images validated using synthetic data”. *Chemical Engineering & Technology* 39 (3), pp. 395–402.
- Easwaran, P., Hahn, F., Lehmann, M.J., Redenbach, C., and Schladitz, K. (2016b). “Representative domain size study on simulated 3D fiber systems.” *Proceedings of FILTECH 2016*. Filtech Exhibitions Germany, Cologne.
- Faessel, M., Delisée, C., Bos, F., and Castera, P. (2005). “3D Modelling of random cellulosic fibrous networks based on X-ray tomography and image analysis”. *Composites Science and Technology* 65 (13), pp. 1931–1940.
- Feder, J. (1980). “Random sequential adsorption”. *Journal of Theoretical Biology* 87 (2), pp. 237–254.
- Fisher, N. I., Lewis, T., and Embleton, B. J. J. (1987). *Statistical analysis of spherical data*. Cambridge University Press.
- Frangi, A. F., Niessen, W. J., Vincken, K. L., and Viergever, M. A. (1998). “Multiscale vessel enhancement filtering”. *Medical Image Computing and Computer-Assisted Intervention — MICCAI’98: First International Conference Cambridge, MA, USA, October 11–13, 1998 Proceedings*. Ed. by W. M. Wells, A. Colchester, and S. Delp. Springer Berlin Heidelberg, pp. 130–137.
- Franke, J., Redenbach, C., and Zhang, N. (2016). “On a mixture model for directional data on the sphere”. *Scandinavian Journal of Statistics* 43 (1), pp. 139–155.
- Fraunhofer ITWM, Department of Image processing (2016). *MAVI - Modular Algorithms for Volume Images*. URL: <http://www.mavi-3d.de>.
- Gaiselmann, G., Thiedmann, R., Manke, I., Lehnert, W., and Schmidt, V. (2012). “Stochastic 3D modeling of fiber-based materials”. *Computational Materials Science* 59, pp. 75–86.
- Gaiselmann, G., Froning, D., Tötze, C., Quick, C., Manke, I., Lehnert, W., and Schmidt, V. (2013). “Stochastic 3D modeling of non-woven materials with wet-proofing agent”. *International Journal of Hydrogen Energy* 38 (20), pp. 8448–8460.
- Hutten, I. M. (2007). *Handbook of non-woven filter media*. First Edition. Elsevier Ltd.
- Jeulin, D. (1991a). “Modèles de Fonctions Aléatoires multivariées”. *Sci. Terre* 30, pp. 225–256.
- (1991b). “Modèles Morphologiques de Structures Aléatoires et de Changement d’Echelle”. PhD thesis. Université de Caen.
- (2011). *Variance scaling of Boolean random varieties*. Tech. rep. N/10/11/MM (2011), hal-00618967, version 1. Centre de Morphologie Mathématique.
- Kanit, T., Forest, S., Galliet, I., Mounoury, V., and Jeulin, D. (2003). “Determination of the size of the representative volume element for random composites: statistical and numerical approach”. *International Journal of Solids and Structures* 40 (13-14), pp. 3647–3679.

- Kanit, T., N'Guyen, F., Forest, S., Jeulin, D., Reed, M., and Singleton, S. (2006). "Apparent and effective physical properties of heterogeneous materials: Representativity of samples of two materials from food industry". *Computer Methods in Applied Mechanics and Engineering* 195 (33-36), pp. 3960–3982.
- Karayiannis, N. C. and Laso, M. (2008). "Monte Carlo scheme for generation and relaxation of dense and nearly jammed random structures of freely jointed hard-sphere chains". *Macromolecules* 41 (4), pp. 1537–1551.
- Kärkkäinen, S., Nyblom, J., Miettinen, A., Turpeinen, T., and Pötschke, P. (2009). "A stochastic shape model for fibres with an application to carbon nanotubes". *10th European Congress of Stereology and Image Analysis*. Ed. by V. Capasso, G. Aletti, and A. Micheletti. Esculapio.
- Kärkkäinen, S., Miettinen, A., Turpeinen, T., Nyblom, J., Pötschke, P., and Timonen, J. (2012). "A stochastic shape and orientation model for fibres with an application to carbon nanotubes". *Image Analysis & Stereology* 31 (1), pp. 17–26.
- Kronenberger, M., Wirjadi, O., Freitag, J., and Hagen, H. (2015). "Gaussian curvature using fundamental forms for binary voxel data". *Graphical Models* 82, pp. 123–136.
- Lantuéjoul, C. (1991). "Ergodicity and integral range". *Journal of Microscopy* 161, pp. 387–403.
- Lehmann, M., Bastuck, H., Harenbrock, M., Brosi, H., and Beier-Hoys, S. (2013). "Method and system of determining the fiber diameter distribution of a fibrous media". Pat. US Patent US8594382 B2.
- Lehmann, M. J., Weber, J., Kilian, A., and Heim, M. (2016). "Microstructure simulation as part of fibrous filter media development processes - from real to virtual media". *Chemical Engineering & Technology* 39 (3), pp. 403–408.
- Matheron, F. (1975). *Random sets and integral geometry*. Probability and mathematical statistics. Wiley.
- Matteson, M. J. and Orr, C., eds. (1987). *Filtration: principles and practices*. Marcel Dekker, Inc., New York.
- Mościński, J. and Bargieł, M. (1989). "The force-biased algorithm for the irregular close packing of equal hard spheres". *Molecular Simulation* 3 (4), pp. 201–212.
- Naddeo, F., Cappetti, N., and Naddeo, A. (2014). "Automatic versatile parametric procedure for a complete FEM structural analysis of composites having cylinder-shaped reinforcing fibres". *Computational Materials Science* 81, pp. 239–245.
- Oh, W. and Lindquist, W.B. (1999). "Image thresholding by indicator kriging". *IEEE transactions on pattern analysis and machine intelligence* 21 (6), pp. 590–602.
- Ohser, J. and Mücklich, F. (2000). *Statistical analysis of microstructures in materials science*. John Wiley & Sons, Ltd, Chichester.
- Ohser, J. and Schladitz, K. (2009). *3D Images of material structures - processing and analysis*. Wiley - VCH, Weinheim.
- Otsu, N. (1979). "A threshold selection method from gray level histograms". *IEEE Transactions on Systems, Man, and Cybernetics* 9 (1), pp. 62–66.

- Öznergiz, E., Kiyak, Y. E., Kamasak, M. E., and Yildirim, I. (2014). “Automated nanofiber diameter measurement in SEM images using a robust image analysis method”. *Journal of Nanomaterials* 2014, pp. 1–6.
- Pagenkemper, S. K., Peth, S., Puschmann, D. U., and Horn, R. (2013). “Effects of root-Induced biopores on pore space architecture investigated with industrial X-Ray computed tomography”. *Soil-Water-Root Processes: Advances in Tomography and Imaging*. Ed. by Stephen H. Anderson and Jan W. Hopmans. The Soil Science Society of America, Inc., pp. 69–96.
- Pan, Y. (2010). “Stiffness and progressive damage analysis on random chopped fiber composite using FEM”. PhD thesis. Rutgers, The State University of New Jersey.
- Pan, Y., Iorga, L., and Pelegri, A. A. (2008). “Numerical generation of a random chopped fiber composite RVE and its elastic properties”. *Composites Science and Technology* 68 (13), pp. 2792–2798.
- Pastorelli, E. and Herrmann, H. (2016). “Time-efficient automated analysis for fibre orientations in steel fibre reinforced concrete”. *Proceedings of the Estonian Academy of Sciences* 65 (1), pp. 28–36.
- Payen, J., Vroman, P., Lewandowski, M., Perwuelz, A., Callé-Chazelet, S., and Thomas, D. (2012). “Influence of fiber diameter, fiber combinations and solid volume fraction on air filtration properties in nonwovens”. *Textile Research Journal* 82 (19), pp. 1948–1959.
- Peyrega, C., Jeulin, D., Delisée, C., and Malvestio, J. (2009). “3d morphological modelling of a random fibrous network”. *Image Analysis & Stereology* 28 (3), pp. 129–141.
- Prill, T. and Schladitz, K. (2013). “Simulation of FIB-SEM images for analysis of porous microstructures”. *Scanning* 35 (3), pp. 189–195.
- R Core Team (2013). *R: A language and environment for statistical computing*. R Foundation for Statistical Computing. Vienna, Austria. URL: <http://www.R-project.org/>.
- Redenbach, C. and Vecchio, I. (2011). “Statistical analysis and stochastic modelling of fibre composites”. *Composites Science and Technology* 71 (2), pp. 107–112.
- Schladitz, K., Peters, S., Reinel-Bitzer, D., Wiegmann, A., and Ohser, J. (2006). “Design of acoustic trim based on geometric modeling and flow simulation for non-woven”. *Computational Materials Science* 38 (1), pp. 56–66.
- Schuler, F., Schnell, J., and Breit, W. (2011). “Use of computer-tomography for the analysis of fibre reinforced concrete”. *Symposium Prague 2011*.
- Shin, E. H., Cho, K. S., Seo, M. H., and Kim, H. (2008). “Determination of electrospun fiber diameter distributions using image analysis processing”. *Macromolecular Research* 16 (4), pp. 314–319.
- Sliseris, J., Andrä, H., Kabel, M., Wirjadi, O., Dix, B., and Plinke, B. (2016). “Estimation of fiber orientation and fiber bundles of MDF”. *Materials and Structures* 49 (10), pp. 4003–4012.
- Soille, P. (1999). *Morphological image analysis*. Springer, Berlin Heidelberg New York.
- Stirzaker, R. J., Passioura, J. B., and Y, Wilms. (1996). “Soil structure and plant growth: Impact of bulk density and biopores”. *Plant and Soil* 185 (1), pp. 151–162.

- Stoyan, D., Kendall, W. S., and Mecke, J. (1995). *Stochastic geometry and Its applications*. Second edition. John Wiley & Sons.
- Thiedmann, R., Fleischer, F., Hartnig, C., Lehnert, W., and Schmidt, V. (2008). "Stochastic 3D modeling of the GDL structure in PEMFCs based on thin section detection". *Journal of The Electrochemical Society* 155 (4), pp. 8391–8399.
- Tomadakis, M. M. and Sotirchos, S. V. (1991). "Effective Kundsens diffusivities in structures of randomly overlapping fibers". *AIChE Journal* 37 (1), pp. 74–86.
- Wiegmann, A., Iliev, O., and Schindelin, A. (2010). "Computer aided engineering of filter materials and pleated filters". *Global Guide of the Filtration and Separation Industry* by E. von der Luehe. VDL - Verlag, pp. 191–198.
- Wirjadi, O. (2009). "Models and algorithms for image-based analysis of microstructures". PhD thesis. University of Kaiserslautern.
- Wirjadi, O., Schladitz, K., Easwaran, P., and Ohser, J. (2016). "Estimating fibre direction distributions of reinforced composites from tomographic images". *Image Analysis & Stereology* 35 (3), pp. 167–179.
- Ziabari, M., Mottaghitalab, V., McGovern, S. T., and Haghi, A. K. (2007). "A new image analysis based method for measuring electrospun nanofiber diameter". *Nanoscale Research Letter* 2 (12), pp. 597–600.

List of Figures

1.1 Spunbond process. Image source: http://www.edana.org	2
1.2 Flow chart for virtual microstructure design. 3D rendering of the first two images are obtained using MAVI (Fraunhofer ITWM, Department of Image processing 2016) and third image using the GeoDict2017 software (Math2Market, Kaiserslautern, Germany).	3
1.3 Scanning electron microscopy (SEM) images of nonwoven polymer filter media from MANN+HUMMEL GmbH, Ludwigsburg.	4
2.1 Density plot for the Schladitz distribution. 1000 points are sampled from the Schladitz distribution on the sphere for various parameters β . (a) $\beta = 0.1$ (orientations concentrate on the z -axis) (b) $\beta = 1$ (orientations are uniformly distributed) (c) $\beta = 10$ (orientations are isotropically distributed in the xy -plane). White color represents high values and red color represents low values. Red color on sphere boundaries in (b) is due to discretization effect.	9
2.2 Realizations of systems of cylinders generated using the RSA cylinder model. Common input model parameters: window size = 100^3 voxels, radius and length are uniformly distributed in the intervals $[3, 5]$ and $[150, 200]$, respectively. Orientation follows the Schladitz distribution with $\beta = 0.01$ (a), $\beta = 1$ (b), and $\beta = 5$ (c).	11
2.3 Illustration for edge correction. (a) No edge correction (b) Edge correction: plus sampling (C) Edge correction: periodic edge treatment . . .	12
3.1 Curved fiber modeled by a chain of polyhedra with elliptical cross-section. 1, 2, and 3 denote x -axis, y -axis, and z -axis, respectively. Reprinted from Composites Science and Technology, 68/13, Y. Pan, L. Iorga, A. A. Pelegri, Numerical generation of a random chopped fiber composite RVE and its elastic properties, 2792–2798, Copyright (2008), with permission from Elsevier.	16
3.2 Chain of spheres	18
3.3 Realizations of the fiber system from the Altendorf-Jeulin approach for input parameters: window size = 250^3 voxels, number of fibers = 80, $\beta = 10$, fiber radius = 5 voxels, $\kappa_1 = 10$, and $\kappa_2 = 100$. (a) Overlapping fiber system. (b) Non-overlapping fiber system.	20

3.4	Graph $G = (P, E)$ of a fiber system. Spheres are vertices P and connections between the spheres are edges E . a , c , and b are arbitrary spheres.	21
3.5	The original distance $D_{orig}(v_1, v_2)$ and the original angle $A_{orig}(a, c, b)$. . .	21
3.6	The overlap between two spheres p and q	22
3.7	Chain of spheres. The distance between sphere centers x_{j_i} and $x_{j_{(i+1)}}$ is $\frac{r_j}{2}$. The sphere p_{j_1} is overlapping with spheres from p_{j_2} to p_{j_4} . The length of the path between spheres p_{j_1} and p_{j_5} is 4.	22
3.8	Angle force geometry.	25
3.9	Realization of a packed fiber system. Model parameters: Window size = 250^3 voxels, number of fibers = 300, isotropic orientation ($\beta = 1$), constant fiber length = 300 voxels, fiber radius = 5 voxels, and bending parameters $\kappa_1 = 10$ and $\kappa_2 = 100$. Volume fraction = 46%. Higher volume fractions can be achieved for anisotropic orientation distributions or shorter fibers.	26
3.10	3D realization of a fiber system simulated using the Altendorf-Jeulin model. Fiber end points are visible in the observation window.	27
3.11	Generation of center coordinate x_{j_c}	28
3.12	Simulation of a fiber as a chain of spheres. (a) Center sphere. (b) New sphere along the line of the fiber main direction. (c) The $(s + 1)$ -th sphere along the line of the main direction. (d) Further spheres are generated until it reaches the boundaries. (e) New sphere along the line of the inverted fiber main direction. (f) The $(t + 1)$ -th sphere along the line of the inverted main direction. (g) Further spheres are generated until it reaches the boundaries.	30
3.13	Realizations of the fiber system with endless fibers for input parameters: window size = 250^3 voxels, number of fibers = 255, $\beta = 5$, fiber radius = 5 voxels, $\kappa_1 = 10$, and $\kappa_2 = 100$. (a) Overlapping fiber system in an extended window $W' = 450^3$. (b) Non-overlapping fiber system in an extended window $W' = 450^3$. Volume fraction = 20%	31
3.14	Realizations of the fiber system with endless fibers for various β . (a) Orientation concentrated on the z -axis ($\beta = 0.1$) and volume fraction = 20%. (b) Isotropic orientation ($\beta = 1$) and volume fraction = 17%. (c) Isotropy within the xy -plane ($\beta = 5$) and volume fraction = 21%. Common parameters are window size = 250^3 voxels, fiber radius = 5 voxels, $\kappa_1 = 10$, and $\kappa_2 = 100$	31
3.15	Realization of the fiber system with endless fibers for input parameters: window size = 1000^3 voxels, volume fraction = 8%, $\beta = 5$, fiber radius = 5 voxels, $\kappa_1 = 10$, and $\kappa_2 = 100$	32

3.16	Realizations of fiber systems with fiber bundles from Method I. (a) Fiber radius = 5 voxels and volume fraction = 12%. (b) Fiber radii = 4, and 8 voxels and volume fraction = 13%. Common parameters are window size = 250^3 voxels, $\beta = 10$, $\kappa_1 = 10$, and $\kappa_2 = 100$	36
3.17	Realizations of fiber systems with fiber bundles from Method II. (a) Entwined fibers ($\varepsilon = 0$) and volume fraction = 13%. (b) Parallel fibers ($\varepsilon = 1$) and volume fraction = 12%. Common parameters are window size = 250^3 voxels, fiber radius = 5 voxels, $\beta = 10$, $\kappa_1 = 10$, and $\kappa_2 = 100$	37
4.1	Realizations of the fiber system with different volume fractions. Input model parameters: window size = 100^3 voxels, $\beta = 5$, fiber radius = 5 voxels, $\kappa_1 = 10$, and $\kappa_2 = 100$. (a) Volume fraction = 13%. (b) Volume fraction = 29%. (c) Volume fraction = 51%.	40
4.2	A realization of Model I. Model parameters: window size = 250^3 voxels, number of fibers = 100, $\beta = 5$, fiber thickness = 10 voxels, and fiber length = 300 voxels.	43
4.3	A realization of Model II. window size = 250^3 voxels, number of fibers = 100, $\beta = 5$, fiber thicknesses are uniformly distributed in the interval (3,6), and fiber length = 300 voxels.	44
4.4	A realization of Model III. Model parameters: window size = 250^3 voxels, number of fibers = 100, $\beta = 5$, fiber thicknesses are uniformly distributed in the interval (3,16), and fiber length = 300 voxels.	44
4.5	A realization of Model IV. Model parameters: window size = 250^3 voxels, volume fraction = 10%, $\beta = 5$, fiber thickness = 10 voxels, $\kappa_1 = 200$, and $\kappa_2 = 5$	45
4.6	A realization of Model V. window size = 250^3 voxels, volume fraction = 10%, $\beta = 5$, fiber thickness = 10 voxels, $\kappa_1 = 10$, and $\kappa_2 = 100$	45
4.7	Deviation of the mean of the estimated β for Model I.	46
4.8	Deviation of the mean of the estimated β for Model II. (a) Hessian. (b) Inertia method.	47
4.9	Deviation of the mean of the estimated β for Model III. (a) Plot for the Hessian approach. (b) Plot for the inertia method.	48
4.10	Deviation of the mean of the estimated β for Model IV.	49
4.11	Deviation of the mean of the estimated β for Model V.	49
4.12	(a) A 3D visualization of the CT image of the non-woven material. Size: $580 \times 580 \times 300$ voxels and voxel edge length: $1.87 \mu m$. (b) The segmented image of (a)	50

4.13	The mean and standard deviation of pressure drop computed over 5 realizations for each combination of κ_1 and κ_2 . These realizations are without fiber bundles (Model A).	52
4.14	The mean and standard deviation of pressure drop computed over 5 realizations for each combination of κ_1 and κ_2 . 20% of the fibers in these realizations form bundles of two fibers (Model B).	52
4.15	The mean and standard deviation of pressure drop computed over 5 realizations for each combination of κ_1 and κ_2 . 60% of the fibers in these realizations form bundles of two fibers (Model C).	53
4.16	A 3D visualization of generated fiber system. Common parameters: Window size = $580 \times 580 \times 300$ voxels, fiber radius = 7.96 voxels, $\beta = 4.37$. (a) $\kappa_1 = 5$ and $\kappa_2 = 100$. (b) $\kappa_1 = 5$ and $\kappa_2 = 200$. (c) $\kappa_1 = 10$ and $\kappa_2 = 100$. (d) $\kappa_1 = 20$ and $\kappa_2 = 200$. (e) $\kappa_1 = 30$ and $\kappa_2 = 200$. (f) $\kappa_1 = 50$ and $\kappa_2 = 200$	54
5.1	Realizations of our stochastic geometry model in different domain sizes $2000^2 \times 512$ voxels, $1000^2 \times 512$ voxels, $750^2 \times 512$ voxels, $500^2 \times 512$ voxels, and $250^2 \times 512$ voxels. Volume fraction $\approx 10\%$, fiber radius = 10 voxels and fibers are oriented in the xy -plane.	56
5.2	The mean and standard deviation (error bar) of the packing density (a), the pressure drop (b), and the pore size distribution (c) computed for 10 realizations of each domain size.	57
5.3	Fitted straight line for the mean squared error of the packing density.	60
5.4	Fitted straight line for the mean squared error of the pressure drop.	60
5.5	Relative error of the packing density (a) and the pressure drop (b)	62
5.6	Relative error of three different quantiles of the pore size distribution.	62
6.1	Realization of a fiber system with fiber bundles and its thickness estimation. Input fiber thickness for the 3D model is 6 voxels and volume fraction = 1%. (a) Realization of the 3D fiber model. (b) Synthetic SEM image of the 3D model. (c) Area weighted thickness histogram of (b). The automatic approach captures the peak obtained by the true solution. The overestimation occurs due to the image contrast. Some parts of the fiber bundles are treated as single fiber.	64
6.2	Realization of a fiber system with fiber bundles and its thickness estimation. Input fiber thicknesses for the 3D model are chosen as 8 and 16 voxels each with probability 0.5 and volume fraction = 5%. (a) Realization of the 3D fiber model. (b) Synthetic SEM image of the 3D model. (c) Area weighted thickness histogram of (b). The automatic approach captures the two peaks obtained by the true solution. Frequencies of the peaks are different.	65

6.3	Realization of a fiber system with fiber bundles and its thickness estimation. Input fiber thickness for the 3D model is 16 voxels and volume fraction = 12%. (a) Realization of the 3D fiber model. (b) Synthetic SEM image of the 3D model. (c) Area weighted thickness histogram of (b). The automatic approach features an additional peak.	66
6.4	SEM of the real material (a) and its thickness map (b). Simulated SEM image (c) and its thickness map (d). Both in the SEM image of a real material and simulated SEM images, some of the fibers overlay others and shadows of upper fibers fall on lower fibers. The estimation method underestimates the fiber thickness of the lower fibers due to these overlaying and shadowing effects.	66
6.5	(a) Realization of the 3D fiber model. (b) Synthetic SEM image of the 3D model. (c) Mask image. (d) Ground truth. (e) Estimated local fiber orientation of (b). (f) Mask image after erosion. (g) Ground truth masked with (e). (h) Estimated masked with (e). (i) Ground truth and estimated fiber orientation plot.	68
6.6	(a) Realization of the 3D fiber model. (b) Synthetic SEM image of the 3D model. (c) Mask image. (d) Ground truth. (e) Estimated local fiber orientation of (b). (f) Mask image after erosion. (g) Ground truth masked with (e). (h) Estimated masked with (e). (i) Ground truth and estimated fiber orientation plot.	69
6.7	(a) Realization of the 3D fiber model. (b) Synthetic SEM image of the 3D model. (c) Mask image. (d) Ground truth. (e) Estimated local fiber orientation of (b). (f) Mask image after erosion. (g) Ground truth masked with (e). (h) Estimated masked with (e). (i) Ground truth and estimated fiber orientation plot.	70
6.8	Volume rendering of the CT image of the soil sample. Size: $399 \times 399 \times 983$ voxels with a voxel edge length of $463 \mu\text{m}$. Reprinted from Computers & Geosciences, 98, B. Bauer, X. Cai, S. Peth, K. Schladitz, G. Steidl, Variational-based segmentation of bio-pores in tomographic images, 1-8, Copyright (2017), with permission from Elsevier.	72
6.9	(a) A fiber with a branch. (b) A fiber system with fiber branches	72
6.10	(a) Cropped sample of steel fiber reinforced concrete with fiber cluster and single fiber (image size: $247 \times 301 \times 180$ voxels). (b) Labeled image from a standard labeling procedure.	74
6.11	Noisy data of fiber clusters cropped from CT image of steel fiber reinforced concrete. (a) Image size: $257 \times 311 \times 100$ voxels. (b) Image size: $480 \times 114 \times 184$ voxels	74

-
- 6.12 One of the fiber clusters from CT image of steel fiber reinforced concrete (image size: $791 \times 232 \times 943$ voxels). 76
- 6.13 Labeled image with gaps in the fiber. 77
- 6.14 Labeled image after filling the gaps. Some fibers have more than one label. 77
- 6.15 (a) Labeled image after manual merging of labels in image shown in Figure 6.14. (b) Labeled image obtained from the standard particle separation. 78
- 6.16 (a) One of the fiber clusters from CT image of steel fiber reinforced concrete (image size: $257 \times 311 \times 100$ voxels). (b) Labeled image. 78
- 6.17 (a) One of the fiber clusters from CT image of steel fiber reinforced concrete (image size: $480 \times 114 \times 184$ voxels). (b) Labeled image. 79

List of Tables

2.1	Image types	13
4.1	Input parameters for the ML estimator considered in our experiments	42

